Studies in discrete and continuum mechanics

Studies in discrete and continuum mechanics

A dissertation presented
by

Zhiyan Wei

to
The School of Engineering and Applied Sciences
in partial fulfillment of the requirements
for the degree of
Doctor of Philosophy
in the subject of

Applied Math

Harvard University
Cambridge, Massachusetts
March 2014

Thesis advisor

L. Mahadevan

Author

Zhiyan Wei

Studies in discrete and continuum mechanics

Abstract

We have used a combination of theory and computation to investigate collective aspects of discrete mechanical systems. The analysis involves considerations from geometry, elasticity and hydrodynamics. We have developed continuum theories to describe these systems, in the spirit of compressing information by mathematical abstraction from the discrete description.

As examples, we have studied the geometric mechanics of a particular mechanical metamaterial – origami. Origami structures have unusual mechanical properties that arise almost exclusively from the geometry of the constituent folds and the constraint of piece-wise isometric deformations of collective rigid plaquettes. We have analytically characterized the planar and non-planar effective elastic response of a simple periodically folded structure, Miura-ori, in terms of Poisson's ratios and rigidities for the first time. We have studied the dynamical coarsening of a fluid-immersed array of lamellae or filaments that is attached to a substrate and dried. For a 1D array of lamellae, we have explicitly derived a discrete theory with a firm basis on the microscopic physics. This analysis allows us to both analytically predict the onset of coarsening and numerically study the hierarchical evolution of clusters. We have also developed a general continuous model of phase separation with an arrest to capture the pattern formation that may be applicable to a variety of physical and biological systems. Generalizing the analysis to the 2D array of filaments, where the fluid domain is connected, we have explained many of the salient experimental observations by a numerical

finite element method. Finally, we show our studies on two sorts of meniscus instabilities arising in geometrically confined thin elastic films when they are stressed: one is the adhesive failure along the solid-solid interface and another is the cohesive instability at the free meniscus surface. We have constructed a geometric model based on symmetry arguments to reproduce the 2D rippling pattern of the crack front arising in the adhesive instability. Our numerical studies have captured the wavelength, the critical loading displacement, and the subcritical nature of the cohesive instability that leads to large amplitude fingers of air protruding into the elastomer.

Contents

Acknowledgments

Completing this doctoral work has been a wonderful and often overwhelming experience. I definitely have enjoyed the physics itself which has been the real learning experience. At the same time, I have struggled to build up confidence in myself in the crowd of scary smart people, overcome my shyness to give a coherent talk, work in a group, and hold teaching sections. I have also gained valuable experiences on technical issues, such as how to write a paper and code intelligibly.

I have been very privileged to have undoubtedly the most intuitive, smart and supportive advisor that any PhD student could ask for – L. Mahadevan. Ever since I read several of his papers when I was still an undergraduate in China, I have been hoping to work with him. After coming to Harvard, I have been more stimulated and excited by his constant flow of good ideas. I always admire his ability to see connections between fields that are vastly different to me and compress information by mathematical abstraction. He has also been quite an inspiring teacher. I will never forget that for numerous times, Maha demonstrated to me how to construct a mathematical model from sketch and then dissect the expressions into physically or geometrically meaningful terms so that I could learn to tell if a model made sense even without deriving it. I have also learned a great deal of physics and fascinating visual explanations of them from him. He has fostered certainly an open, friendly and collaborative research group. He has given me all the freedom to pursue independent research interest, and has also known when and how to give me a little push in the forward direction when I needed it. Maha has been more than just an academic advisor to me. He has always been supportive and willing to help me out of difficult times in my life. He has influenced my attitude and philosophy towards not only science but also life.

Throughout my six years, I was supported for 5 years through the generosity of my advisor so that I could always concentrate on my work. During my first year I thank Harvard University for providing my fellowship.

Maha's other students and post-docs, both past and present, comprise a superb research group. The stream of new ideas in different fields from many excellent minds has constantly reminded me how little I know about science and motivated me to explore more. Among many people, Ee Hou Yong has been my best friend at Harvard. He has been very supportive and patient whenever I needed someone to talk about my research work, and has given me many useful feedbacks to sharpen my arguments. We have had weekly dinners together for years to exchange ideas/news in science and life. I really appreciate his friendship, kindness and positive outlook to life. Haiyi Liang, a very energetic and sharp researcher, has driven me to think through many problems during discussions. Many of his fancy ideas have dazzled me and made research work colorful. Shreyas Mandre has set up a wonderful example of rigorous mathematician for me. He has also taught me quite a bit on numerical methods and perturbation methods. Paulo Paoletti, Luca Giomi, John Biggins, Andres Concha, Greg Morrison, Madhusudhan Venkadesan, Mahesh Bandi, Nadir Kaplan and Mattia Gazzola, all very easy-going and extraordinarily good scientists, have been willing to share their expertise with me and help me learn software and tools to complete my research work. Last but not least, I will always cherish the time that I have spent in Pierce 405 – the "PhD student office". Everyone stayed or staying in this office is amazing. It has been my pleasure to work with and hang out with John Kolinski, Andy McCormick, Sam Ocko and Levi Dudte; also Aryesh Mukherjee and Madhav Mani from the earlier days. We have shared our pains and gains on our journey to the PhD.

Our group's secretary Claudia Stearns is surely the kindest, coolest and most warm-hearted person. She has helped me out in preparation of all kinds of documentations in various situations, when I usually have no clue how to start.

There are countless others who have been there for me throughout my time as a graduate student. Tobias Schneider has been an encouraging friend and collaborator, and

a provider of fascinating physics conversations. Tadashi Tokieda has applied mathematical ideas to explain and design numerous toys that always inspire me. Lihua Jin is a guru of ABAQUS, who I have always consulted. Matt Pharr, Ben Jordan, and Yu Qin have been wonderful influences and friends, and the countless nights we stayed up until birds sang to finish problem sets will be always my precious memories.

I will undoubtedly give credit to my father Peizhou Wei and my mother Xiuzhen Xu for my fascination with the physical world and my opportunity to pursue my dream in the best university. Although they both received little education in those chaotic decades of last century in China, they have devoted their lives to raise me and create environment as much as they could to help me explore my interest. They did not teach me much specific knowledge in science, but have done a great job stimulating me to independently study following my own interest in physics and math. My late sister, Dan Wei, loved and cared about me more than herself throughout her life. My motivation to study hard in my early days was very simple – not to disappoint my sister, as she could never go to school because of the severe heart disease and had always hoped me to be a good student. It is sad to realise that she cannot be present for this moment in my life, but I am sure she would be proud of me if she knew. I thank my mother-in-law Yaqin Zhao for educating my wife to be such a great lady before we met. I also appreciate her long-term encouragement and support to my career for all these years.

Finally, my wife Shuqing Wu has been my guiding light and love over the past 5 years. She has accompanied me through my worst days and shared my joy in my best moments. She has provided unconditional support when I felt confused about my future. She has been such a caring and fun person that makes home the most relaxing and comforting place for me. She has also known when to ask me to take a break to enjoy life once I become too obsessed with my work. Without her, I could not be as good as I am now.

Dedicated to my father Peizhou Wei,
my mother Xiuzhen Xu,
my wife Shuqing Wu,
my mother-in-law Yaqin Zhao
and my late sister Dan Wei.

Chapter 1

Introduction and summary

Structure of this thesis

This thesis falls naturally into four parts, which are relatively independent:

- Geometric mechanics of Miura-ori (Chapter 2)
- Discrete model on capillarity-induced dynamical collapse of elastic lamellae and pillars (Chapter 3)
- Continuum model on dynamics of elastocapillary coalescence and arrest (Chapter 4)
- Studies on fingering instabilities in a confined elastic film: a geometric model on cohesive failure and numerical studies on adhesive instabilities (Chapter 5).

All these four parts embrace the common theme: we have been trying to create a bridge between the discrete and continuum mechanics. For example, Miura-ori plate [1] can be modeled as discrete rigid plaquettes elastically hinged together. It is appropriate to characterize the collective responses of this structure using a continuum theory at a scale that is much larger than a plaquette. Similarly, an array of elastic lamellae or pillars that is fluid-immersed and anchored on a substrate [2, 3, 4] is also intrinsically a discrete system.

While a discrete model that encodes physics (including surface tension, fluid flow, surface adhesion in the contact area and bending deformation of pillars or lamellae) and geometry is a natural way to precisely capture the response of a small-scale system, a continuum theory is a more effective and mathematically more condensed way to describe the system with a much larger scale. The example of fingering instabilities [5, 6, 7, 8], however, is different from the previous two because the thin confined elastic film is continuum, but the mechanical responses are discrete. First, instabilities lead to discrete large amplitude "digits" or fingers. Second, the subcritical nature of the cohesive instability, as we shall see later, makes the transition sudden with a region of bistability between the fingered and flat states.

Geometric mechanics of periodic pleated origami

Metamaterials are defined as materials whose structure and constitution allows them to have unusual emergent properties, such as negative refractive index optical metamaterials [9], or negative Poisson ratio mechanical metamaterials [10]. Here, we focus on origami-inspired mechanical metamaterials that arise as folded and pleated structures in a variety of natural systems including insect wings [11], leaves [12], and flower petals [13]. Using the presence of creases in these systems allows one to fold and unfold an entire structure simultaneously and design deployable structures such as solar sails [1] and foldable maps [14], and auxetic structural materials such as foams [15], and microporous polymers [16, 17]. Indeed, folded sheets with reentrant geometries serve as models for crystal structures [18, 19], molecular networks [20], and glasses [10] in a variety of physical applications. Complementing these studies, there has been a surge of interest in the mathematical properties of these folded structures [21, 22, 23], and some recent qualitative studies on the engineering aspects of origami [24, 25, 26]. In addition, the ability to create them de novo

without a folding template, as a self-organized buckling pattern when a stiff skin resting on a soft foundation is subject to biaxial compression [27, 28, 29] has opened up a range of questions associated with their assembly in space and time, and their properties. However, most past quantitative work on these materials has been limited to understanding their behavior in two dimensions, either by considering their auxetic behavior in the plane, or the bending of a one-dimensional corrugated strip.

In Chapter 2, we characterize the three-dimensional elastic response, Poissons ratios, and rigidities of perhaps the simplest such mechanical metamaterial based on origami – a three-dimensional periodically pleated or folded structure, the Miura-ori pattern (Fig. 2.1a), which is defined completely in terms of two angles and two lengths.

Capillarity-induced dynamical collapse of elastic lamellae and pillars

There has been growing recent interest in the self-assembly [30] of simple constituents into complex structures. The nature of the interactions between constituents that need to be controlled to form structures at high yield depends on their size. While the assembly on molecular lengthscales [31] is driven by chemical interactions between constituents, capillary forces [32, 33, 34] have been considered as driving forces on larger scales. In a typical experimental setting, the solid constituents maybe fully immersed in a liquid which is subsequently drying so that capillary forces at the forming liquid-gas interfaces lock the constituents into their desired position.

Among many building blocks, synthetic fibers, often anchored at a stiff support structure have been widely used. Examples include millimeter-scaled macroscopic brush hairs [3], micrometer-scaled mesoscopic polymeric surface mimicking gecko foot hairs [35], as well as nanometer-scaled carbon nanotube forests [36, 37]. Fibers are long and soft objects and can easily bend. Here a competition between actuating capillarity and resisting

elasticity selects the structures formed.

In order to predict and control the formation of specific structures containing many constituents, all physical mechanisms that affect the final structure need to be modeled in sufficient detail. Elastocapillary interaction have been well characterized in two-body systems [38, 39, 40]. However, for the collective behavior of many elastic fibers bundling together, most work have employed static energy minimization arguments to estimate the expected finally assembled bundle size [3, 41, 42]. An exception is the recent work [43] that uses stability analysis of the unpatterned base state to predict the hierarchical coalescence structure for an array of clamped parallel elastic sheets which are partially immersed in liquid. It considers the slender body regime so that the linear beam theory always applies in renormalization, and cannot explain the irregularity of the bundle size. Unlike in ergodic systems where the state space is stochastically sampled due to thermal excitations, the structures in elastocapillary systems are often not selected by energetics alone. Instead, they depend critically on the dynamics of the drying process. This leads to a path dependence caused by the strong coupling of the geometry of the air-liquid interface to the local evaporation when multiple unconnected liquid domains are formed. Additional aspects, such as pinning and contact angle hysteresis, as well as the permanent adhesion of contacts formed in intermediate structures, make purely energetic arguments unable to have any predicative power. Thus, to predict and control the assembled structures in capillarity-driven self-assembly experiments, we need to (1) follow the dynamics over time as irreversible effects associated with evaporation, contact line motion and adhesion, and (2) account for non-linear effects due to large deviations from the background state and go beyond a linearized analysis.

In Chapter 3, we use a combination of theory and computation to understand the instability and the hierarchical evolution of cluster formation for both two- and three-

dimensional elastocapillary systems driven by drying. Those systems represent generic situations, allow for a thorough theoretical treatment and can be validated by well controlled experiments. For the two dimensional case, we describe the drying induced collapse of an one-dimensional array of evenly spaced lamella immersed in the evaporating liquid (Figure 3.1(a)(b)). For this system *all* relevant physical forces are considered, allowing us to derive the interaction potentials and forces, analyze the linear stability of the system, and compute the nonlinear dynamics associated with pattern coarsening. We demonstrate that different dynamical paths through the system's state space indeed lead to different final structures which are observed in experiments.

In the three-dimensional case, our theory focuses on explaining experiments associated with the bundling of a regular square grid of fluid-immersed elastic posts anchored to a substrate [4] (Figure 3.1(c)-(e)). We determine the constant mean curvature surface for the air-liquid interface subjected to the global liquid volume constraint on the multi-connected domain. This allows us to compute the interaction forces and thence the primary unstable mode. Finally we use a numerical method to compute the aggregation dynamics.

Dynamics of elastocapillary coalescence and arrest

Capillary coalescence arises in a number of systems, including particles at an interface as well as filaments and lamellae that are brought together by interfacial forces which drive aggregation. Sometimes, these systems coarsen indefinitely, while at other times elastic deformations eventually arrest the process. Examples of the former include particles at an interface driven together by capillary and/or magnetic forces where aggregation and assembly continues eventually leading to just a single cluster [44, 45]. In contrast to the aggregation of free particles, elastic deformations of the bristles and lamellae eventually limit the coarsening leading to many finite sized clusters [2, 3, 4]. Prior investigations of

the elastocapillary coalescence of these systems has been primarily focused on understanding the final size of the bundle using energy minimization [3, 41]. Exceptions include a generic continuum mean-field theory [46] for arrested coarsening, and a discrete theory [43] for regular, ordered hierarchical aggregation. Here, we complement these studies using a long-wavelength continuum theory based on a physically consistent microscopic picture, that accounts for spatial/temporal variations in the pattern driven by inhomogeneities in drying and eventually arrested by elasticity.

In Chapter 4, we propose a continuum theory for the dynamics of elastically limited coarsening that is derived from a microscopic discrete setting of the fluid-mediated interactions between lamellae. All the coefficients in the model are analytically/numerically calculable from the measurable physical and geometrical parameters in experiments. The model well captures the wavelength at the onset of instability and the maximum phase size as well as qualitative features of phase coarsening and refining. This general idea is widely applicable to various physical and biological systems where phase separation with an arrest is involved.

Studies on fingering instabilities in a confined elastic film

Thin soft elastic layers serving as joints between relatively rigid bodies may function as sealants, bearings, adhesives, and mechanical insulators. In adhesive joints, the strains and stresses due to joint loading are magnified by the effects of geometric confinement and scale separation [47], making them susceptible to stress-driven instabilities that often lead to failure. Here, we are interested in two broad ways in which joints fail. One is the adhesive failure along the solid-solid interface. Such instability arises from peeling a relatively stiff elastic plate off a soft thin confined adhesive film. Failure occurs via the loss of adhesion at one of the surfaces attached to the adhesive, and an undulating crack

front can appear and evolve into a 2D rippling pattern. This mode of failure has been well documented and studied [5, 48, 49] in terms of understanding the onset of instabilities and primary mode. Another is the cohesive failure at the exposed free meniscus in the thin elastic layer. Such elastic instability leads to the formation of spatially periodic digits of air that invade the elastic layer, when a joint is loaded under tension [6] or by a fluid that is injected into a cavity in the confined elastic layer [7]. This mode of failure has been largely overlooked experimentally and only recently understood theoretically by our work [8]. Interestingly, the last experiment is an elastic analog of a well studied classical hydrodynamic free-surface instability associated with the relative motion between liquids of different viscosities in a narrow gap [50, 51]. This instability is not limited to Newtonian fluids, but is observed for many non-Newtonian fluids, and for perfectly plastic solids [52] as well. As we shall see, the elastic instability is fundamentally different given its reversible nature and lack of dependence on interfacial forces.

In Chapter 5, for the first part, we construct a minimal mathematical model that can reproduce the form of the crack front completely based on geometry and symmetry arguments. Quantitative features, including the onset of instability and primary mode in the linear regime, and the finger amplitude and widths of fat and thin fingers in the non-linear regime, are all well captured through correct choice of a reasonable number of fitting parameters. The choice of parameters is based on an optimization setting. For the second part, I present my numerical contributions in the work [8] to capture the subcritical nature of instability and compare with the linear theory, as well as experiments, on predications of the critical loading displacement and wavelength at the onset of instability.

Chapter 2

Geometric mechanics of periodic pleated origami

Here, we characterize the geometry and planar and non-planar effective elastic response of a simple periodically folded structure Miura-ori, which is composed of identical unit cells of mountain and valley folds with four-coordinated ridges, defined completely by 2 angles and 2 lengths. We find that the in-plane and out-of-plane Poisson's ratios are equal in magnitude, but opposite in sign, independent of material properties. Furthermore, we show that effective bending stiffness of the unit cell is singular, allowing us to characterize the 2-dimensional deformation of a plate in terms of a 1-dimensional theory for a beam, again independent of material properties. Finally, we solve the inverse design problem of determining the geometric parameters that achieve the optimal geometric and mechanical response of these mechanical metamaterials with an extreme deformation response.

2.1 Geometry and kinematics

The geometry of the unit cell embodies the basic element in all nontrivial pleated structures - the mountain or valley fold, wherein four edges (folds) come together at a single vertex, as shown in Fig.2.1d. It is parameterized by two dihedral angles $\theta \in [0, \pi]$, $\beta \in [0, \pi]$, and one oblique angle α, in a cell of length l, width w, and height h. We treat the structure as being made of identical periodic rigid skew plaquettes joined by elastic hinges at the ridges. The structure can deploy uniformly in the plane (Fig.2.1b) by having each constituent skew plaquette in a unit cell rotate rigidly about the connecting elastic ridges. Then the ridge lengths l_1, l_2 and $\alpha \in [0, \pi/2]$ are constant through folding/unfolding, so that we may choose θ (or equivalently β) to be the only degree of freedom that completely characterizes a Miura-ori cell. The geometry of the unit cell implies that

$$\begin{aligned} &\beta = 2\sin^{-1}[\zeta \sin(\theta/2)], \quad l = 2l_1\zeta, \\ &w = 2l_2\xi \quad \text{and} \quad h = l_1\zeta \tan\alpha \cos(\theta/2), \end{aligned} \tag{2.1}$$

where the dimensionless width and height are

$$\xi = \sin\alpha \sin(\theta/2) \quad \text{and} \quad \zeta = \cos\alpha(1-\xi^2)^{-1/2}. \tag{2.2}$$

We see that β, l, w, and h change monotonically as $\theta \in [0, \pi]$, with $\beta \in [0, \pi]$, $l \in 2l_1[\cos\alpha, 1]$, $w \in 2l_2[0, \sin\alpha]$, and $h \in l_1[\sin\alpha, 0]$. As $\alpha \in [0, \pi/2]$, we see that $\beta \in [\theta, 0]$, $l \in [2l_1, 0]$, $w \in [0, 2l_2\sin(\theta/2)]$ and $h \in [0, l_1]$. The geometry of the unit cell implies a number of interesting properties associated with the expansion kinematics of a folded Miura-ori sheet, including design optimization for packing, and the study of nearly orthogonally folds when $\alpha \approx \pi/2$, the singular case corresponding to the common map fold where the folds are all independent (**Supplementary Material in Appendix**; Appendix A.1). To minimize algebraic complexity and focus on the main consequences of isometric deformations of these structures, we will hitherto assume each plaquette is a rhombus, i.e. $l_1 = l_2 = l_e$.

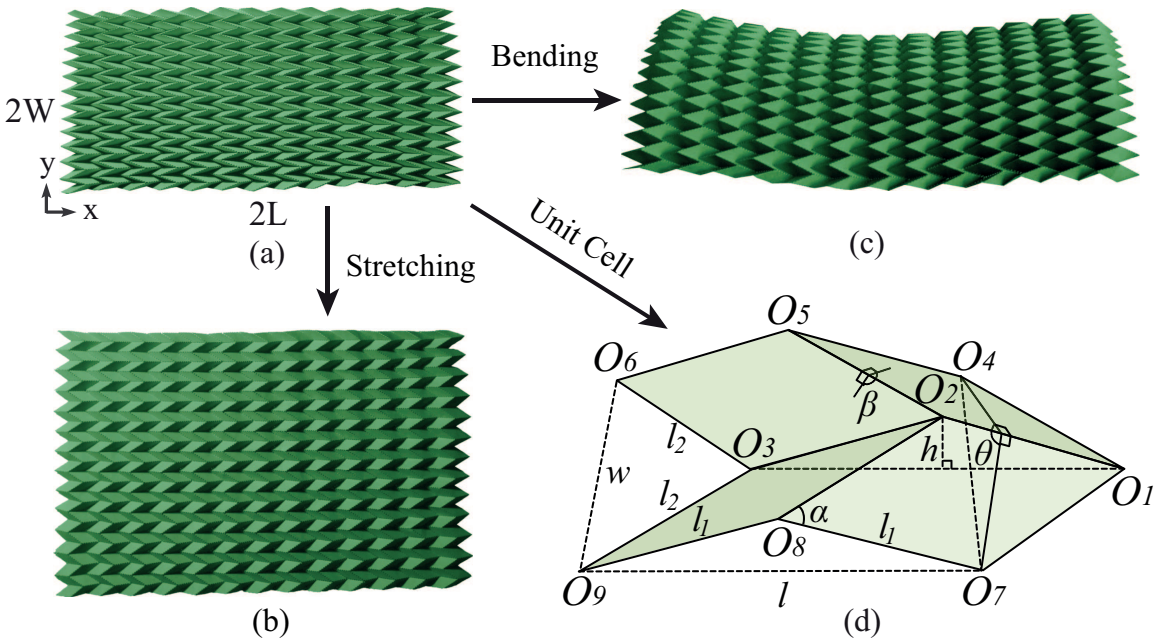

Figure 2.1: Geometry of Miura-ori pattern. (a) A Miura-ori plate folded from a letter size paper contains 13 by 13 unit cells (along x and y direction respectively), with $\alpha = 45^o$ and $l_1 = l_2 = l_e$. The plate dimension is $2L$ by $2W$. (b) In-plane stretching behavior of a Miura-ori plate when pulled along the x direction shows its expand in all directions, i.e. it has a negative Poisson's ratio. (c) Out-of-plane bending behavior of a Miura-ori plate when a symmetric bending moment is applied on boundaries $x = \pm L$ shows a saddle shape, consistent with that in this mode of deformation its Poisson's ratio is positive. (d) Unit cell of Miura-ori is characterized by two angles α and θ given l_1 and l_2 and is symmetric about the central plane passing through $O_1O_2O_3$.

2.2 In-plane response

The planar response of Miura-ori may be characterized in terms of 2 quantities – the Poisson's ratio which describes the coupling of deformations in orthogonal directions, and the stretching rigidity which characterizes its planar mechanical stiffness. The planar Poisson's ratio is defined as

$$\nu_{wl} \equiv -\frac{dw/w}{dl/l} = 1 - \xi^{-2}. \tag{2.3}$$

It immediately follows that the reciprocal Poisson's ratio $\nu_{lw} = 1/\nu_{wl}$. Because $\xi \leq 1$, the in-plane Poisson's ratio $\nu_{wl} < 0$ (Fig.2.2a), i.e. Miura-ori is an auxetic material. The limits on ν_{wl} may be determined by considering the extreme values of α, θ, since ν_{wl} monotonically increases in both variables. Using the expression (2.2) in (2.3) and expanding the result shows that $\nu_{wl}|_{\alpha\to 0} \sim \alpha^{-2}$, and thus $\nu_{wl}|_\theta \in (-\infty, -\cot^2(\theta/2)]$, while $\nu_{wl}|_{\theta\to 0} \sim \theta^{-2}$ and thus $\nu_{wl}|_\alpha \in (-\infty, -\cot^2\alpha]$. When $(\alpha, \theta) = (\pi/2, \pi)$, $\nu_{wl} = 0$ so that the two orthogonal planar directions may be folded or unfolded independently when the folds themselves are orthogonal, as in traditional map-folding. Indeed, this is the unique state for which non-parallel folds are independent, and it should surprise the reader that with few exceptions, this is the way maps are folded – makes unfolding easy, but folding frustrating! The Poisson's ratios related to height changes, ν_{hl} and ν_{wh} can also be determined using similar arguments (Appendix A.2.1).

To calculate the in-plane stiffness of the unit cell, we note that the potential energy of a unit cell deformed by a uniaxial force f_x in the x direction is $H = U - \int_{\theta_0}^{\theta} f_x(dl/d\theta')d\theta'$, assuming that the elastic energy of a unit cell is stored only in the elastic hinges which allow the rigid plaquettes to rotate isometrically, with $U = kl_e(\theta - \theta_0)^2 + kl_e(\beta - \beta_0)^2$, k being the hinge spring constant, θ_0 and β_0 $(= \beta(\alpha, \theta_0))$ being the natural dihedral angles in the undeformed state. Then the external force f_x at equilibrium is determined by the relation

$\delta H/\delta\theta = 0$, while the stretching rigidity in the x direction is given by

$$K_x(\alpha,\theta_0) \equiv \left.\frac{df_x}{d\theta}\right|_{\theta_0} = \frac{4k[(1-\xi_0^2)^2+\cos^2\alpha]}{(1-\xi_0^2)^{\frac{1}{2}}\cos\alpha\sin^2\alpha\sin\theta_0}, \tag{2.4}$$

where $\xi_0 = \xi(\alpha,\theta_0)$ and ξ is defined in (2.2). To understand the bounds on K_x, we expand (2.4) in the vicinity of the extreme values of α and θ_0 which gives us $K_x|_{\alpha\to 0} \sim \alpha^{-2}$, $K_x|_{\alpha\to\pi/2} \sim (\pi/2-\alpha)^{-1}$, $K_x|_{\theta_0\to 0} \sim \theta_0^{-1}$ and $K_x|_{\theta_0\to\pi} \sim (\pi-\theta_0)^{-1}$. As expected, we see that K_x has a singularity at $(\alpha,\theta_0) = (\pi/2,\pi)$, corresponding to the case of an almost flat, unfolded orthogonal Miura sheet.

We note that K_x is not a monotonic function of the geometric variables defining the unit cell, α and θ_0. Setting $\partial_{\theta_0}K_x|_\alpha = 0$ and $\partial_\alpha K_x|_{\theta_0} = 0$ allows us to determine the optimal design curves, $\theta_{0m}(\alpha)$ (green dotted curve in Fig.2.2b) and $\alpha_m(\theta_0)$ (red dashed curve in Fig.2.2b) that yield the minimum value of the stiffness K_x as a function of these parameters. Along these curves, the stiffness varies monotonically. Analogous arguments allow us to determine the orthogonal stretching rigidity K_y, which is related geometrically to K_x via the design angles α and θ (Appendix A.2.2, A.2.3). Since piece-wise isometric deformations only allow for planar folding as the only possible motion using rigid rhombus plaquettes in Miura-ori plates (Appendix A.3.1), the in-plane shear elastic constant is infinite; an unusual result given that most normal materials may be sheared easily and yet strongly resist volumetric changes.

2.3 Out-of-plane response

To understand the non-planar bending response of Miura-ori, we must consider the conditions when it is possible to bend a unit cell isometrically, i.e. with only rotations of the plaquettes about their linking hinges. Minimally, isometric deformations require the introduction of 1 additional diagonal fold into each plaquette (Fig.2.3a), either a short one

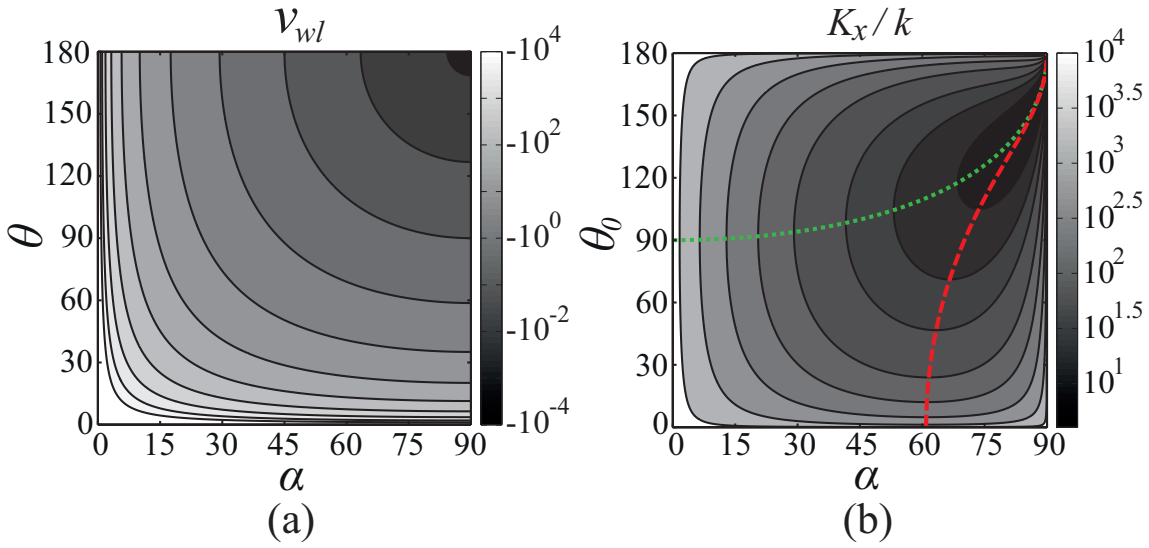

Figure 2.2: In-plane stretching response of a unit cell. (a) Contour plot of Poisson's ratio ν_{wl}. ν_{wl} shows that it monotonically increases with both α and θ. $\nu_{wl}|_{\alpha} \in [-\infty, -\cot^2 \alpha]$, and $\nu_{wl}|_{\theta} \in [-\infty, -\cot^2(\theta/2)]$. (b) Contour plot of the dimensionless stretching rigidity K_x/k. The green dotted curve indicates the optimal design angle pairs that correspond to the minima of $K_x|_{\alpha}$. The red dashed curve indicates the optimal design angle pairs that correspond to the minima of $K_x|_{\theta_0}$. See the text for details.

(e.g. O_2O_7) or a long one (e.g. O_1O_8). Here, we adopt the short fold, as a result of which 4 additional DOFs arise in each unit cell and allow for both symmetric bending and asymmetric twisting, depending on whether the rotations are symmetric or not. The out-of-plane bending Poisson's ratio $\nu_b \equiv -\kappa_y/\kappa_x$ [1], where κ_x, κ_y are the effective curvatures of the Miura ori sheet in the x and y directions given by

$$\begin{aligned} \kappa_x &= \frac{\cos(\alpha/2)\sin(\theta/2)}{2l_e\sqrt{1-\xi^2}}(\phi_2+\phi_4), \\ \kappa_y &= -\frac{\sqrt{1-\xi^2}}{4l_e\sin(\alpha/2)\xi}(\phi_2+\phi_4), \end{aligned} \tag{2.5}$$

with κ_x being the dihedral angle between plane $O_6O_3O_9$ and $O_4O_1O_7$ (Fig.2.3a) projected onto the x direction over the unit cell length (Appendix A.2.2), and κ_y being the dihedral angle between plane $O_4O_5O_6$ and $O_7O_8O_9$ projected onto the y direction over the unit cell width. The angles ϕ_2, ϕ_4 characterize rotations about internal folds $\overrightarrow{O_7O_2}$ and $\overrightarrow{O_8O_3}$ respectively, and are deemed positive according to the right-hand rule. We note that although there are a total of 5 deformation angles (Fig.2.3a), both κ_x and κ_y depend only on ϕ_2 and ϕ_4. This is because of the symmetry of deformations about xoz plane; ϕ_3 and ϕ_5 are functions of ϕ_1 and ϕ_2 (Eq. A.28 in Appendix A.2.2), and the case that ϕ_1 changes while keeping ϕ_2 and ϕ_4 zero corresponds to the planar stretch of a unit cell, so ϕ_1 does not contribute to both curvatures. This is consistent with our intuition that bending a unit cell requires the bending of plaquettes. The Poisson's ratio for bending thus is

$$\nu_b = -\frac{\kappa_y}{\kappa_x} = -1 + \xi^{-2} = -\nu_{wl}, \tag{2.6}$$

where the last equality follows from Eqs. (2.3) and (2.5). If the original plaquettes are allowed to fold along the long diagonals instead (e.g. O_8O_1 in Fig.2.3a), the new curvature components κ_x and κ_y are still given by (2.5) with α being replaced by $\pi - \alpha$ (Appendix

[1] In general, the incremental Poisson's ratio is $\nu_b = -d\kappa_y/d\kappa_x$, but here we only consider linear deformations about the flat state, so $\nu_b = -\kappa_y/\kappa_x$

A.2.3), and ϕ_2, ϕ_4 now being rotations about axis $\overrightarrow{O_8O_1}$ and $\overrightarrow{O_9O_2}$ respectively. Therefore $\nu_b = -\kappa_y/\kappa_x = -\nu_{wl}$. We note that in non-planar bending, the sheet behaves like a normal material, deforming into a saddle as shown in Fig.2.1c. The surprising result, that the in-plane Poisson's ratio is equal in magnitude but opposite in sign to the out-of-plane Poisson ratio, is independent of the mechanical properties of the sheet and is a consequence of geometry alone. Although our analysis is limited to the case when the deformation involves only small changes in the angles about their natural values, this not as restrictive as it seems, since small changes to the unit cell can still lead to very large global deformations of the entire sheet.

Given our understanding of the geometry of bending in a unit cell, we now derive an effective continuum elastic theory for a Miura-ori plate that consists of many unit cells. Our calculations for the unit cell embodied in (2.5) show that κ_x/κ_y is only a function of the design angles α and θ, and independent of deformation angles, i.e. one cannot independently control κ_x and κ_y. Physically, this means that purely cylindrical deformations with zero Gaussian curvature are impossible, as locally the unit cell can only be bent into a saddle with negative Gaussian curvature. Mathematically, this implies that in the continuum limit the effective stiffness matrix [53] of a 2-dimensional Miura ori plate is singular, and has rank 1, which indicates a remarkable result: the Miura plate can be described completely by a 1-dimensional beam theory instead of a 2-dimensional plate theory.

To calculate the bending stiffness per unit width of a single cell in the x direction B_x, we note that although the elastic energy is physically stored in the 8 discrete folds (Fig.2.3a) and thus expressed as $kl_e(2\phi_1^2 + \phi_3^2 + 2\phi_5^2) + 2k_p l_e \sin(\frac{\alpha}{2})(\phi_4^2 + \phi_2^2)$, where k and k_p are the spring constants of the ridges and the diagonal folds of plaquettes respectively, in the continuum theory, it is effectively stored in the entire unit cell when bent into a sheet with curvature κ_x and thus expressed as $\frac{1}{2}B_x wl\kappa_x^2$. B_x is derived by equating these two

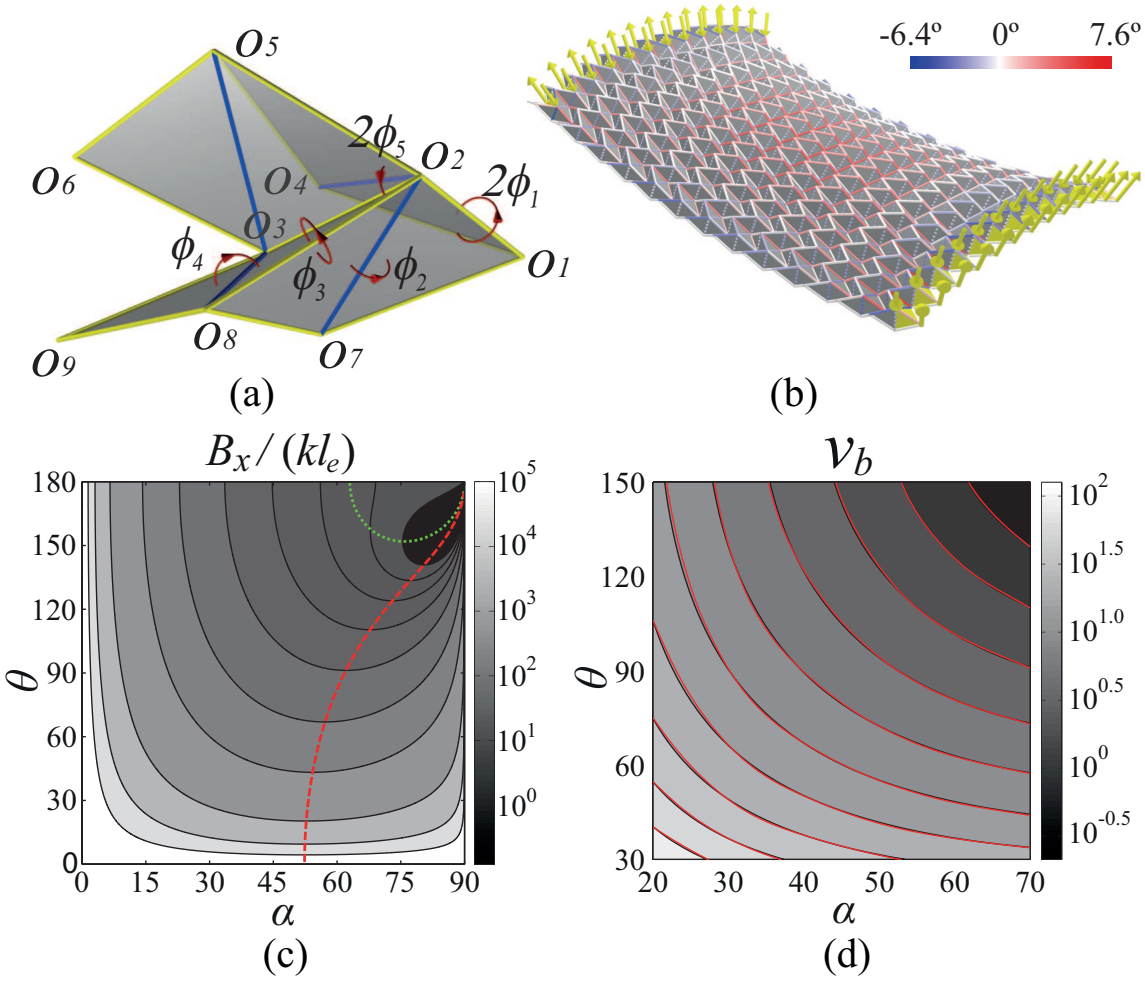

Figure 2.3: Out of plane bending response of a unit cell. (a) The plaquettes deformations about each fold are symmetric about the plane $O_1O_2O_3$, so that the angles $2\phi_1$, ϕ_2, ϕ_3, ϕ_4 and $2\phi_5$ correspond to rotations about the axes $\overrightarrow{O_1O_2}$, $\overrightarrow{O_7O_2}$, $\overrightarrow{O_2O_8}$, $\overrightarrow{O_8O_3}$ and $\overrightarrow{O_3O_2}$ respectively. (b) Numerical simulation of the bending of a Miura-ori plate with $\alpha = 45^o$ and $\theta = 90^o$. Force dipoles are shown by yellow arrows. Color of the folds indicates the value of deformation angles. (c) Contour plot of dimensionless bending stiffness $B_x/(kl_e)$ corresponding to pure bending of a unit cell. The green dotted curve and red dashed curve indicate the optimal design angle pairs that correspond to the local minima of $B_x|_\alpha$ and $B_x|_\theta$ respectively. (d) Contour plot of bending Poisson's ratio. The gray scale plot is from the analytic expression 2.6 and the red curves are extracted from simulation results. In our simulations, we use a plate made of 21 by 21 unit cells and vary α from 20^o to 70^o, θ from 30^o to 150^o both every 10^o.

expressions and inserting w, l from (2.1) and κ_x from (2.5). In general, B_x depends on multiple independent deformation angles, although here we only study the "pure bending" case, where a row of unit cells aligned in the x direction undergo the same deformation and the stretching is constrained, i.e. $\phi_1 = 0$ for all cells, and then $\phi_2 = \phi_4$ must be satisfied. In this well-defined case of bending, $\phi_3 = \frac{1}{2}\phi_2 \csc\frac{\alpha}{2}(1 - \frac{2\cos\alpha}{1-\xi^2})$ and $\phi_5 = \frac{1}{2}\phi_2 \csc\frac{\alpha}{2}$, so ϕ_2 (or equivalently ϕ_4) is canceled out in the expression of B_x and B_x is solely dependent on the design angles, so that

$$\begin{aligned} B_x(\alpha,\theta) =& kl_e\left[2 + 16\frac{k_p}{k}\sin^3\frac{\alpha}{2} + \left(1 - \frac{2\cos\alpha}{1-\xi^2}\right)^2\right] \\ & \cot\left(\frac{\theta}{2}\right)\frac{(1-\xi^2)^{3/2}}{2\xi^2\cos\alpha\sin\alpha\cos(\theta/2)}. \end{aligned} \tag{2.7}$$

Just as there are optimum design parameters that allow us to extremize the in-plane rigidities, we can also find the optimal design angle pairs that minimize B_x, by setting $\partial_\theta B_x|_\alpha = 0$ and $\partial_\alpha B_x|_\theta = 0$. This gives us two curves $\theta_m(\alpha)$ and $\alpha_m(\theta)$ shown in Fig.2.3c, where we have assumed $k = k_p$. To understand the bounds on B_x, we expand (2.7) in the vicinity of the extreme values of α and θ which shows $B_x|_{\alpha\to 0} \sim \alpha^{-3}$, $B_x|_{\alpha\to\pi/2} \sim (\pi/2 - \alpha)^{-1}$ and $B_x|_{\theta\to 0} \sim \theta^{-3}$. $B_x|_{\theta\to\pi}$ is bounded except at $(\alpha,\theta) = (\pi/2, \pi)$, where B_x has a singularity, corresponding to the case of an almost flat, unfolded orthogonal Miura sheet. The bending stiffness per unit width of a single cell in the y direction B_y is related to B_x via the expression for bending Poisson's ratio $\nu_b^2 = B_x/B_y$, where ν_b is defined in (2.6). This immediately implies that optimizing B_y is tantamount to extremizing B_x.

The deformation response of a complete Miura-ori plate requires a numerical approach because it is impossible to assemble an entire bent plate by periodically aligning unit cells with identical bending deformations in both the x and y direction. Our numerical model takes the form of a simple triangular-element based discretization of the sheet, in which each edge is treated as a linear spring with stiffness inversely proportional to its rest

length. Each pair of adjacent triangles is assigned an elastic hinge with a bending energy quadratic in its deviation from an initial rest angle that is chosen to reflect the natural shape of the Miur-ori plate. We compute the elastic stretching forces and bending torques in a deformed mesh [54, 55], assigning a stretching stiffness that is six orders of magnitude larger than the bending stiffness of the adjacent facets, so that we may deform the mesh nearly isometrically (Appendix A.3.2). When our numerical model of a Miura-ori plate is bent by applied force dipoles along its left-right boundaries, it deforms into a saddle (Fig.2.3b). In this state, asymmetric inhomogeneous twisting arises in most unit cells; indeed this is the reason for the failure of averaging for this problem, since different unit cells deform differently, and we cannot derive an effective theory by considering just the unit cell. This is in contrast with the in-plane case, where the deformations of the unit cell are affinely related to those of the entire plate. Excluding the boundary effect, the maximal deformation angle that leads to the maximal stress experienced by the plaquettes appears in the middle region of the Miura-ori plate, which may potentially cause fracture of the pattern.

To compare the predictions for the bending Poisson's ratio ν_b of the 1-dimensional beam theory with those determined using our simulations, in Fig.2.3d we plot ν_b from (2.6) (the gray scale contour plot) based on a unit cell and ν_b extracted at the center of the bent Miura-ori plate from simulations (the red curves). We see that these two results agree very well, because the unit cell in the center of the plate does have a symmetry plane so that only symmetric bending and in-plane stretching modes are activated, consistent with the assumptions underlying (2.6).

2.4 Summary

Folded structures, mechanical metamaterials might be named Orikozo, from the Japanese for Folded Matter. Our analysis of the simplest of these structures is rooted in the geometry of the unit cell as characterized by a pair of design angles α and θ together with the constraint of piecewise isometric deformations. We have found simple expressions for the linearized planar stretching rigidities K_x, K_y, and non-planar bending rigidities B_x and B_y, and shown that the bending response of a plate can be described in terms of that of a one-dimensional beam. Furthermore, we find that the in-plane Poisson's ratio $\nu_{wl} < 0$, while the out-of-plane bending Poisson ration $\nu_b > 0$, an unusual combination that is not seen in simple materials, satisfying the general relation i.e. $\nu_{wl} = -\nu_b$; a consequence of geometry alone. Our analysis also allows us to pose and solve a series of design problems to find the optimal geometric parameters of the unit cell that lead to extrema of stretching and bending rigidities as well as contraction/expansion ratios of the system. This paves the way for the use of optimally designed Miura-ori patterns in such passive settings as 3-dimensional nanostructure fabrication [56], and raises the possibility of optimal control of actuated origami-based materials in soft robotics [57] and elsewhere using the simple geometrical mechanics approaches that we have introduced here.

Note: While our work was under review for publication, an experimental engineering study on foldable structures was published [58] consistent with our comprehensive theoretical and computational approach to the geometry and mechanics of Miura-ori.

Chapter 3

Capillarity-induced dynamical collapse of elastic lamellae and pillars

When hair dries it clumps together due to surface tension-induced forces along the liquid menisci between the flexible hairs. Similarly, when a fluid-immersed array of lamellae or filaments that is attached to a substrate is dried, evaporation leads to the formation of menisci on the tips of the plates or pillars that bring them together. Building on prior experimental observations, we use a combination of theory and computation to understand the nature of this instability and its evolution in both the two-dimensional and three-dimensional setting of the problem. For the case of lamellae, we explicitly derive the interaction torques based on the relevant physical parameters. The Bloch-wave analysis captures the critical volume of the liquid and the 2-plate-collapse eigenmode at the onset of instability. We study the evolution of clusters and their arrest using numerical simulations to explain the hierarchical cluster formation and characterize the sensitive dependence of

final structures on the initial perturbations. We then generalize our analysis to treat the problem of pillar collapse in 3D, where the fluid domain is completely connected and the interface is a surface with the uniform mean curvature. This captures the salient features of prior experimental observations.

In §3.1 we describe the experimental observations for the two-dimensional case, derive a discrete two-plate model for the deformation of the plates driven by capillary forces, and carry out a linear stability analysis of the base state. We then study the coalescence dynamics of a collection of plates in the nonlinear regime. In §3.2 we describe the experimental observations for the three-dimensional case, and introduce a dynamical model that allows us to simulate the morphology of clustered pillars, and compare these results with experiments. In §3.3, we conclude with a description of open problems in this rich area.

3.1 Collective dynamics of elastic lamellae

3.1.1 The two-dimensional system and experimental observations

For the two-dimensional case (Figure 3.2), we consider a one-dimensional array of elastic micro-lamellae with height L, thickness h and uniform spacing D, Young's modulus E and Poisson's ratio ν respectively. Each lamella is assumed to be free at one end and anchored at the other on a substrate [2]. The lamella array is wetted by a liquid of surface tension σ, density ρ and viscosity μ, which is confined between neighboring lamellae, defining a cell. The contact line slips from the tips as the liquid evaporates. When the system is completely immersed in the liquid, the stable configuration is a uniform array of non-interacting vertical lamellae. However, when the liquid evaporates, it is not necessarily locally stable any more: capillary forces associated with the liquid-air menisci between the

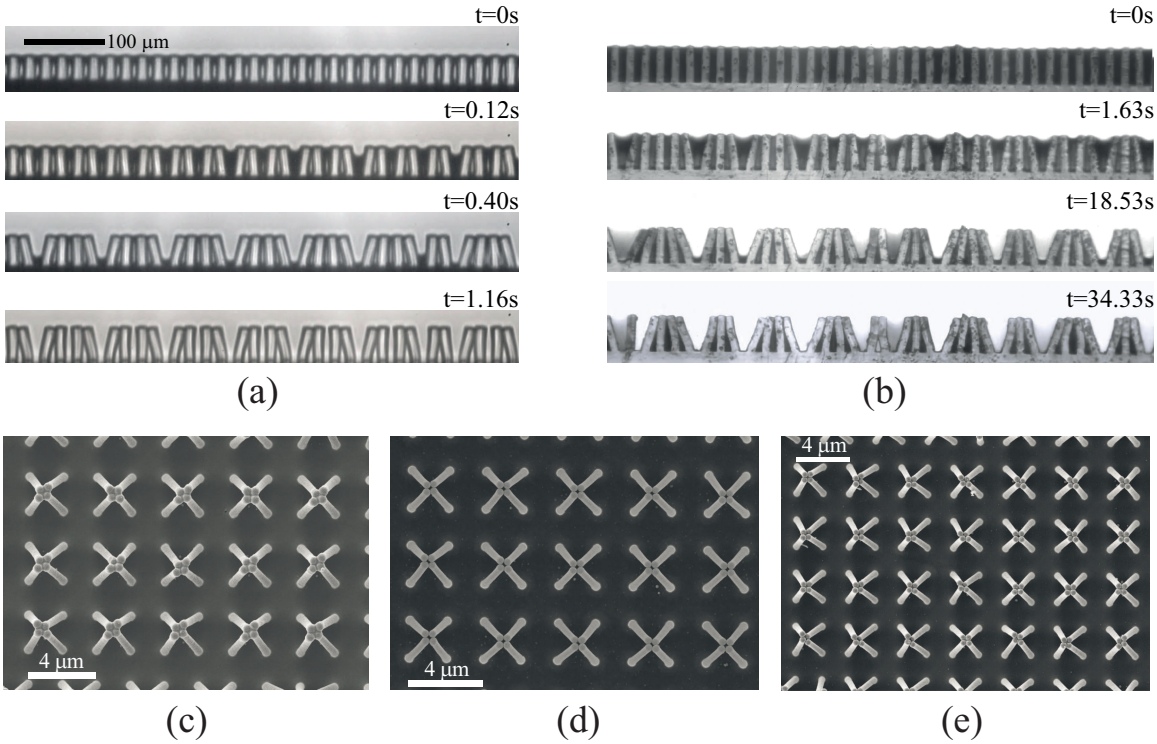

Figure 3.1: (a) and (b) show the dynamics of drying of a one-dimensional array of lamellae. (a) The lamellae are of width $40\mu m$ along the direction into the picture. As the liquid evaporates, a front of 2-lamella coalescence initiates and propagates from right to left, after which a front of 4-lamella coalescence swipes the system in the same direction. After the IPA dries out, the 4-lamella bundles separate and the 2-lamella bundles persist. (b) The lamellae are of width $\sim 1mm$ along the direction into the picture, and the imperfections in the system, e.g. the lamella geometry, roughness of the surface and et al., are larger than those in (a). Coalescence initiates simultaneously here. The 2-lamella mode still appears to be dominant at the onset of instability, and irregular bundles with a size distribution from 2 to 5 arise thereafter and persist even after the IPA dries out. (c)-(e) show the final structures of the two-dimensional array of bristles after the wetting liquid dries out. (c) Tips of the fourfold clusters form rhombi. (d) Tips of the fourfold clusters form squares. (e) A larger domain shows that the four fold clusters are more asymmetric, and the tips form both rhombi and squares. The geometric parameters of the bristles and the material properties are the same in all three images. The only difference is the imperfections of the system.

free ends of the soft lamellae may cause them to deflect laterally and adhere together. In an experimental system with small imperfections, we observe a regular cascade of successive sticking events that leads to a hierarchical bundling pattern: every two neighboring lamellae incline towards each other to form a dimer first, which then collapses into quadrimers (Figure. 3.1(a)). The process repeats until the elastic bending resistance eventually becomes large enough to prevent further coarsening. In the system with large imperfections, irregular bundles can and do arise but the 2-lamella-collapse mode still appears to be dominant right after the instability(Figure. 3.1(b)). After the liquid dries out, bundles separate if the adhesion in contact is not strong to counterbalance the elastic forces; else they persist. In our experiments, the liquid used is isopropyl alcohol (IPA), and the lamellae and the substrate are made of polydimethylsiloxane (PDMS). Throughout this entire section, we use the following experimental parameters $\sigma = 0.022N/m$, $\rho = 786Kg/m^3$, $\mu = 0.0196Pa \cdot s$, $E = 1.5Mpa$, $\nu = 0.5$, $h = 10\mu m$, $L = 40\mu m$, $D = 10\mu m$, and gravity $g = 9.8m/s^2$.

3.1.2 Forces and torques: model description

In our experiments, the lamellae are short and stiff, and remain almost straight as they are deflected by capillary forces. Therefore, we can approximate each lamella as a rigid plate and integrate all the bending response into an elastic hinge at the base. This is in contrast with complementary studies that account for the inhomogeneous bending and buckling (Appendix B.1) of the individual lamella [43, 59]. The hinge elastic constant can be approximately derived from the bending response of a short cantilever by a transverse force F at its free end, which is given by

$$k = \frac{d(F\delta)}{d\theta} = \left(\frac{3L}{Eh^3} + \frac{6}{7GhL}\right)^{-1}, \tag{3.1}$$

where $\delta = 4FL^3(1-\nu^2)/Eh^3 + \alpha_s FL/Gh$ is the deflection at the free end, θ is the tilting angle between the straight plate and the horizontal direction (Figure 3.2(a)), G is the shear

modulus, and α_s is the shear coefficient. The second term of the right hand side of Eq.(3.1) comes from the Timoshenko beam theory [60], because the slender beam condition $L \gg h$ is violated in our experimental setup. We have taken $\nu = 0.5$ and $\alpha_s = 10(1+\nu)/(12+11\nu)$ as an approximation for the rectangular cross section.

To explicitly derive torques due to capillarity, we consider the unit cell consisting of two plates, with liquid confined in between, and air outside (Figure 3.2(a)). The pressure field inside the liquid is nonuniform due to the effects of gravity and flow. However, in our system, gravity can be neglected, because the Bond number $Bo = \Delta\rho g D^2/\sigma \sim 10^{-5} \ll 1$, which indicates that the gravity effect is prevailed by the surface tension force. Comparing the viscous moment due to flow $M_\mu \sim \mu L^5\dot{\theta}/D^3$ (Appendix B.3) with that caused by the surface tension $M_\sigma \sim \sigma L^2/D$, we find that $M_\mu/M_\sigma \sim 10^{-3} \ll 1$ for $\dot{\theta} \sim O(1)$, which indicates that pressure effects due to fluid flow can be neglected. Therefore, the air-liquid interface is always a segment of a circle because of the uniform pressure in each cell. For each plate, the moment results from both the line tension at the contact line, and the pressure gradient across the plate caused by the curvature difference of two neighboring menisci. To calculate the moment we need to find the wetting length, the contact angle, and the pressure difference across the air-liquid interface due to its local curvature. We assume the contact angle to be arbitrary when the meniscus is pinned on the tip, as long as it is larger than the critical value α. The meniscus can thus be concave-up (Figure 3.2(b1)), flat (Figure 3.2(b2)), or concave-down (Figure 3.2(b3)). We assume that once the contact angle reaches the critical value α, it remains constant as the meniscus starts to slide down from the tip (Figure 3.2(b4)-(b6)). Consequently, the meniscus profile and the resulting moment can be calculated for any given tilting angles θ_n, θ_{n+1} and the liquid volume per unit depth V_n. Scaling lengths by L, volumes V_n by L^2 and moments by σL leads to the following results that are necessary for our subsequent linear stability analysis (for details,

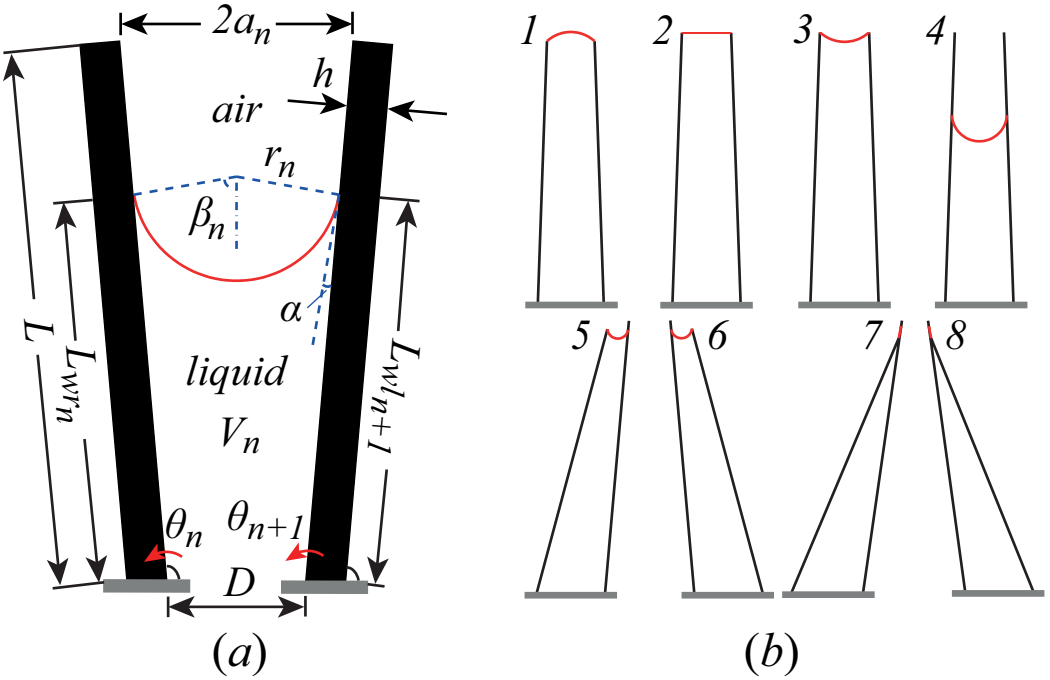

Figure 3.2: (a) Sketch of the model of one cell confined by two adjacent lamellae. Each lamella is modeled as a rigid plate elastically hinged at the base. The plate is of height L and thickness h. θ_n is the angle of n^{th} plate with respect to the horizontal direction. The plate spacing is D and the distance between the two free tips is $2a_n$. V_n is the volume per unit depth of the liquid confined in the cell. Red curve represents the air-liquid interface, which is always a segment of a circle. r_n is the radius of the meniscus and the β_n is the half angle subtended by the meniscus arc. α is the critical contact angle at which the meniscus slides down from the tip and remains afterwards. L_{wln+1} is the wetting length on the left side of the $(n+1)^{th}$ plate and L_{wrn} is the wetting length on the right side of the n^{th} plate. (b) 1-8 are the 8 possible cases of menisci, showing that the menisci can be pinned on both tips, or slip down from one or both tips. 7 and 8 show that when the two free tips are so close that no circular arcs exist to connect them given certain liquid volume and the contact angle constraint, in which case the arc is replaced by a line. They are solely used to prevent the simulation failure in rare cases.

see Appendix B.2).

1. The meniscus is pinned on both tips (Figure 3.2(b1)). The half angle β_n subtended by the meniscus arc is determined by solving

$$V_n = \frac{1}{2}d(\sin\theta_n + \sin\theta_{n+1}) + \frac{1}{2}\sin(\theta_n - \theta_{n+1}) - a_n^2(\beta_n \csc^2\beta_n - \cot\beta_n), \tag{3.2}$$

for given V_n, θ_n and θ_{n+1}, where $d = D/L$ and tip separation is

$$2a_n = \sqrt{2 - 2\cos(\theta_{n+1} - \theta_n) + 2d(\cos\theta_{n+1} - \cos\theta_n) + d^2}. \tag{3.3}$$

β_n must satisfy $\beta_n \leq \hat{\beta}_n$, where $\hat{\beta}_n$ is the critical angle at which the meniscus starts to slide down from at least one lamella. $\beta_n < 0$ when the meniscus concaves down, $\beta_n = 0$ when the meniscus is flat, and $\beta_n > 0$ when the meniscus concaves up. The moments on the n^{th} and $n+1^{th}$ plates are given respectively by

$$M_n = -\frac{1}{2a_n}\left[\sin(\beta_n + \theta_n - \theta_{n+1}) + d\sin(\beta_n + \theta_n)\right], \tag{3.4}$$

$$M_{n+1} = \frac{1}{2a_n}\left[\sin(\beta_n + \theta_n - \theta_{n+1}) - d\sin(\beta_n - \theta_{n+1})\right], \tag{3.5}$$

2. The meniscus has slipped down from both tips (Figure 3.2(b3)). The contact angle is fixed at α. When $\theta_n = \theta_{n+1} = \theta$, the meniscus radius is independent of V_n, and $r_n = d\sin\theta/(2\cos\alpha)$. l_n is determined by solving

$$V_n = \frac{2l_n - d\cos\theta}{2}d\sin\theta - \left(\frac{d\sin\theta}{2}\right)^2\tan\alpha - \frac{\pi - 2\alpha}{2}\left(\frac{d\sin\theta}{2\cos\alpha}\right)^2. \tag{3.6}$$

The wetting length on the right side of the n^{th} plate and that on the left side of the $(n+1)^{th}$ plate are given respectively by

$$L_{wrn} = l_n - \frac{d}{2}\sin\theta\tan\alpha, \tag{3.7}$$

$$L_{wln+1} = l_n - \frac{d}{2}\sin\theta\tan\alpha - d\cos\theta. \tag{3.8}$$

The moments on the n^{th} and $(n+1)^{th}$ plate are given respectively by

$$M_n = -\frac{{L_{wr}}_n^2}{2r_n} - L_{wrn}\sin\alpha, \tag{3.9}$$

$$M_{n+1} = \frac{{L_{wl}}_{n+1}^2}{2r_n} + L_{wln+1}\sin\alpha. \tag{3.10}$$

So far, we have only calculated the moments based on a 2-plate model. To get the total moment on one plate, we must add the contributions from both adjacent cells. For example, we can obtain the full expression of M_n simply by replacing n by $n-1$ in Eq. (3.5) and add up to Eq. (3.4) for the case when the meniscus is pinned at both tips, which readily yields $M_n = M_n(\theta_{n-1}, \theta_n, \theta_{n+1}, V_n, V_{n-1})$.

The dynamics of the n^{th} plate neglecting inertia (Appendix B.3) follows the over-damped first order equation of motion

$$C\frac{\partial\theta_n}{\partial t} + k\left(\theta_n - \frac{\pi}{2}\right) + \sigma L M_n(\theta_{n-1}, \theta_n, \theta_{n+1}, V_n, V_{n-1}) = 0, \tag{3.11}$$

where C is the damping coefficient, k is defined in Eq. (3.1) and the dimensionless moment M_n is due to capillarity. (Readers need to make use of Eqs. (B.5) and (B.6), Eqs. (B.13) and (B.14), Eqs. (B.19) and (B.20), Eqs. (B.25)-(B.28), and Eqs. (B.31) and (B.32) for different situations to obtain the full expressions of M_n as explained above. Please see Appendix B.2 for more details.) To estimate C, we need to account for both the internal viscosity of the solid and the external viscosity of the fluid, and find that the former one dominates, which gives $C \approx \tau_m k$ (Appendix B.3). Together with Eq. (3.11) and the dynamics of drying that will be discussed later, the response of the lamella array is completely determined.

3.1.3 The onset of bundling - linear stability of the base state

For the base state with all lamella being vertical when the liquid volume in each cell is decreased, there is a potential for instability.

To understand this, we consider a periodic domain of $2N$ plates and the same volume of liquid V confined in each cell, when all plates being vertical ($\theta_n = \pi/2, n = 1, 2, ..., 2N$) is an equilibrium state. To determine the stability of this state, we study the perturbations in the moment as a function of variations in the angles θ_n linearized around the current state,

$$d\overrightarrow{M} = (\mathbb{K}_1 + \mathbb{K}_2) d\overrightarrow{\theta}, \tag{3.12}$$

where $\mathbb{K}_1$ and $\mathbb{K}_2$ are the $2N \times 2N$ stiffness matrices due to the elasticity of the plate and the geometrical change of menisci respectively. $\mathbb{K}_1$ is a diagonal matrix with all elements being the dimensionless hinge constant $k_b = (3\sigma L^2/Eh^3 + 6\sigma/7Gh)^{-1}$, and $\mathbb{K}_2$ is a tridiagonal matrix with two additional elements of $-k_1$ on the upper-right and lower-left corners reflecting the periodic boundary condition. At the base state with $\theta_n = \pi/2$, $\mathbb{K}_2$ is expressed as

$$\mathbb{K}_2 = \begin{bmatrix} \ddots & \vdots & \vdots & \vdots & \vdots & \vdots & \\ \dots & -k_1 & 2k_2 & -k_1 & 0 & 0 & \dots \\ \dots & 0 & -k_1 & 2k_2 & -k_1 & 0 & \dots \\ \dots & 0 & 0 & -k_1 & 2k_2 & -k_1 & \dots \\ & \vdots & \vdots & \vdots & \vdots & \vdots & \ddots \end{bmatrix}, \tag{3.13}$$

where $k_1 = \partial M_n/\partial\theta_{n+1} = \partial M_{n+1}/\partial\theta_n$ and $k_2 = -\partial M_n/\partial\theta_n = -\partial M_{n+1}/\partial\theta_{n+1}$ are the stiffness of the effective spring connecting two neighboring plates due to capillarity, where M_n is defined in Eq. (3.4) or Eq. (3.9), and M_{n+1} is defined in Eq. (3.5) or Eq. (3.10). For the case when the meniscus is pinned at both tips,

$$\begin{aligned} k_1 &= k_2 + \sin\beta, \\ k_2 &= \frac{\cos\beta - d\sin\beta}{d}\left[1 + \frac{1 - d(\beta\csc^2\beta - \cot\beta)}{d^2\csc^2\beta(1 - \beta\cot\beta)}\right] - \frac{\sin\beta + d\cos\beta}{d^2}, \end{aligned} \tag{3.14}$$

where β is determined by the volume

$$V = d - (d/2)^2(\beta\csc^2\beta - \cot\beta), \tag{3.15}$$

which follows from Eq. (3.2) and Eq. (3.3) by substituting $\theta_n = \theta_{n+1} = \pi/2$. We here have omitted the subscript n for simplicity for the translationally invariant base state. Note that k_1 and k_2 in this case are not necessarily equal, because while the wetting length is constant, the contact angles change by different amount on the two neighboring plates as they are deflected except when the meniscus is flat. For the case when the meniscus is no longer at both tips,

$$k_1 = k_2,\ k_2 = -\left[\frac{L_w}{r}\sin\alpha + \frac{L_w^2}{2r^2} + \sin^2\alpha\right]\frac{2L_w + d\tan\alpha}{4\cos\alpha}, \tag{3.16}$$

with $r = d/(2\cos\alpha)$ is the radius of the meniscus, and the wetting length L_w is determined by the volume

$$V = L_w d + d^2\tan\left(\frac{\alpha}{4}\right) - d^2\frac{\pi - 2\alpha}{8\cos^2\alpha}, \tag{3.17}$$

which follows from Eqs. (3.6)-(C.7) by substituting $\theta = \pi/2$. k_1 and k_2 in this case are always identical, because the contact angle keeps constant, and the change of wetting length is the same on both plates when they are deflected. From Eqs. (3.14)-(3.17), we see that for any given geometric parameter d and critical contact angle α, $k_i = k_i(V)$ $(i = 1, 2)$. The inset of Figure 3.3(a) shows that k_i switches signs as V decreases, implying that the system could possibly become unstable. The discontinuity in k_i corresponds to the meniscus sliding down from the tip.

To study the instability of the system, we investigate the eigenmode of the stiffness matrix $\mathbb{K} = \mathbb{K}_1 + \mathbb{K}_2$. $\mathbb{K}$ resembles the discrete Laplacian, with eigenvectors

$$\left[1, e^{if}, e^{2if}, \ldots, e^{i(2N-3)f}, e^{i(2N-2)f}, e^{-if}\right], \tag{3.18}$$

and the corresponding eigenvalues

$$\lambda(f) = -2k_1\cos(f) + 2k_2 + k_b,\ \text{where } f = n\pi/N \text{ and } n = 1, 2, \ldots, 2N. \tag{3.19}$$

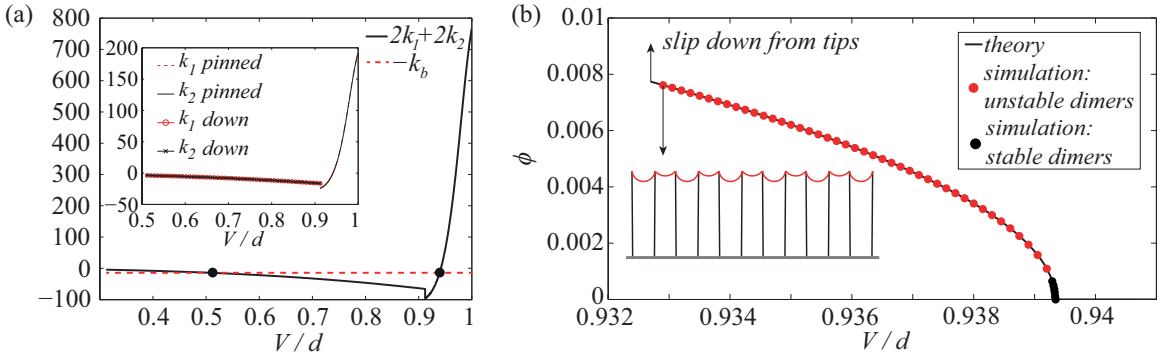

Figure 3.3: (a) shows that the curve of $2k_1 + 2k_2$ as a function of V intersects with the line $-k_b$. The interval between the two intersections indicates the region where the system is unstable as according to Eq. (3.18), $\lambda(\pi) = 2k_1 + 2k_2 + k_b < 0$. For the typical experiments, any $V/d \in (0.5073, 0.9393)$ would result in a tendency to coalesce given infinitesimal perturbations to the system. Inset figure is the effective dimensionless spring constants $k_i(V)$ $(i = 1, 2)$ as shown in Eq. (3.14) and Eq. (3.16). k_i switches signs from positive to negative as V decreases, and the discontinuity corresponds to the meniscus sliding down from the tip. (b) shows the positive bifurcation branch using both simulation and asymptotic expansion. When $V \geq V^* = 0.9393d$, $\phi = 0$, and when $V < V^*$, $\phi \sim \sqrt{V^* - V}$, which is a clear indication of supercritical bifurcation. The inset illustrates the dimer mode. We simulate 2 pillars by solving Eq. (3.11) with periodic boundary conditions, and periodically display them for visualization. For the black dots, dimers are the locally stable configuration. For the red dots, dimers are unstable and will further coalescence.

$\mathbb{K}$ must be positive definite to ensure stability, which is equivalent to requiring the smallest eigenvalue positive. When $k_1 \geq 0$, the meniscus is pinned at both tips, and the smallest eigenvalue is $\lambda(2\pi) = -2k_1 + 2k_2 + k_b = k_b - 2\sin\beta$, which follows from Eqs. (3.14) and (3.19). In our experiments, $k_b \approx 13.5 > 2\sin\beta$, so that the array of vertical plates is stable. When $k_1 < 0$, the smallest eigenvalue is $\lambda(\pi) = 2k_1 + 2k_2 + k_b$, reflecting stability to be controlled by the competition between elasticity and capillarity. As $k_i = k_i(V)$ $(i = 1, 2)$, the condition $\lambda(\pi) < 0$ sets the range of V in which the system is unstable (Figure 3.3(a)). The primary eigenmode corresponds to $f = \pi$, and the eigenvector thus is $[1, -1, 1, -1, \ldots, 1, -1]$ from Eq. (3.18), which indicates the dimer mode. Therefore, to avoid the lamella collapse completely, we need to keep $k_1 > 0$ or reduce $|k_1|$ when $k_1 < 0$ and increase k_b. The practical approaches include the use of liquid with low surface tension and contact angle close to 90^o, at which k_1 is at maximum positive value, the use of stiff solid material, and proper choice of geometric parameters, e.g. large aspect ratio of h/L.

Now we continue to explain the supercritical nature of the transition. We make use of the fact that the fastest growing mode is the dimer mode and assume $\theta_{n-1} - \pi/2 = \pi/2 - \theta_n = \theta_{n+1} - \pi/2 = \phi$. In the vicinity of the critical volume V^* at which the instability happens, the dynamics of any lamella is governed by

$$c\frac{d\phi}{dt} = -(2k_1 + 2k_2 + k_b)\phi - g(V^*)\phi^3 + O(\phi^5), \tag{3.20}$$

where c is the dimensionless damping coefficient, and $g(V^*)$ is a positive, although algebraically lengthy, coefficient of the cubic term. Eq. (3.20) is derived from expanding Eq. (3.11). The even orders of ϕ do not appear in Eq. (3.20) due to $\phi \to -\phi$ symmetry. For the critical $V = V^*$ (equivalently $\beta = \beta^*$), $2k_1 + 2k_2 + k_b = 0$. When $0 < V^* - V \ll 1$, expansion of Eq. (3.14) in the neighborhood of β^* gives us $2k_1 + 2k_2 + k_b \sim \beta^* - \beta$, the expansion of Eq. (3.15) in the neighborhood of β^* gives us $V^* - V \sim \beta - \beta^*$, and hence

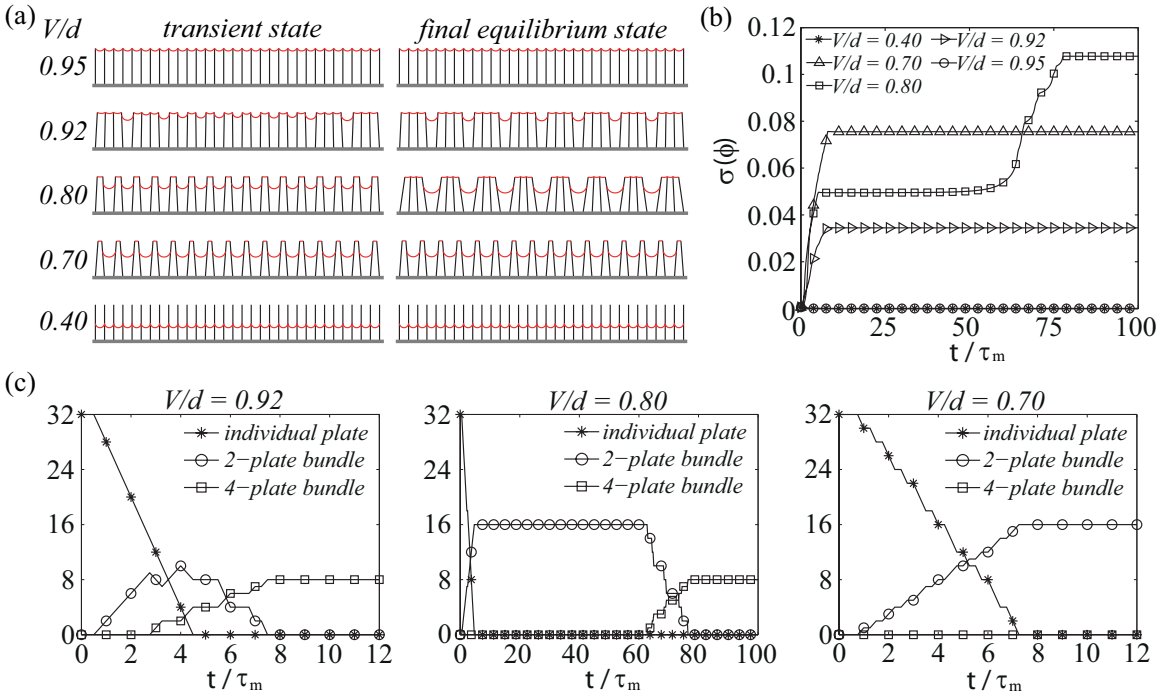

Figure 3.4: (a) A periodic domain of 32 plates is simulated by solving Eq. (3.11) for different prescribed volumes V. The tilting angle θ of only the first plate is perturbed by 0.1% from 90^o as the initial condition. The left column shows the transient states and the right column shows the steady states. (b) The standard deviation of deflection angle ϕ as a function of time. t is time and τ_m is the time scale for mechanical relaxation. (c) Complementing (b), these plots show the evolution of hierarchical formation of bundles for different prescribed volumes. The time resolution of the plots is $0.25\tau_m$ and plates are considered as a bundle if the tilting angle gradient is positive and larger than the perturbation amplitude.

$2k_1 + 2k_2 + k_b \sim V - V^*$. From Eq. (3.20), the stable equilibrium state has two branches of solutions $\phi_1 = -\phi_2 \sim \sqrt{V^* - V}$ for $V^* > V$ and only one solution $\phi = 0$ otherwise, suggesting that the bifurcation is supercritical. Figure 3.3(b) has shown both the positive branch of asymptotic solutions ϕ_1 and the simulation result from 2 lamellae by solving Eq. (3.11) with periodic boundary conditions and they agree well. The inset of the figure clearly indicates a dimer mode.

3.1.4 Beyond linear stability analysis – dynamics for large deviations

Controlled liquid volume

For an initially translationally invariant system, the two-plate-collapse mode is the fastest growing mode, yet the cluster of dimers is not necessarily the final stable state (red dots in Figure 3.3(b)). We notice that for a range of sufficient liquid volumes in each cell, both the deflection of the plates and the geometric change of the liquid menisci are large so that the linear approximation in Section 3.1(3.1.3) breaks down. Therefore, we numerically integrate Eq. (3.11) directly and demonstrate the hierarchical process from an array of vertical individual plates to dimers, to quadrimers thereafter, until to the bundles of the largest size. Figure 3.4(a) shows the snapshots of dynamical coarsening for different control parameters V, in all of which a periodic domain of 32 pillars are simulated, and the tilting angle θ of only one plate is perturbed by 0.1% from 90^o as the initial condition. As expected, for volumes outside the range $V/d \in (0.5073, 0.9393)$, e.g. for the cases of $V/d = 0.95$ and 0.4, the array is stable to perturbations and remains uniformly vertical. Within this unstable parameter range, the primary mode corresponds to two plates collapsing into dimers (Figure 3.3(a)(c)). These dimers may further collapse into quadrimers or stay as the final stable state with different amplitude of deformation angles as shown in Figure 3.4(a)(b). For the same initial perturbation, the dynamical path of successive bundle aggregation depends on the control parameter V. As examples, we see that for $V/d = 0.92$, quadrimers sweep through the domain right after the dimers form and the system reaches the stable equilibrium, for $V/d = 0.80$ the dimers persist for a while before they eventually collapse to quadrimers, and for $V/d = 0.70$ the dimers stay stable, as shown in Figure 3.4(c).

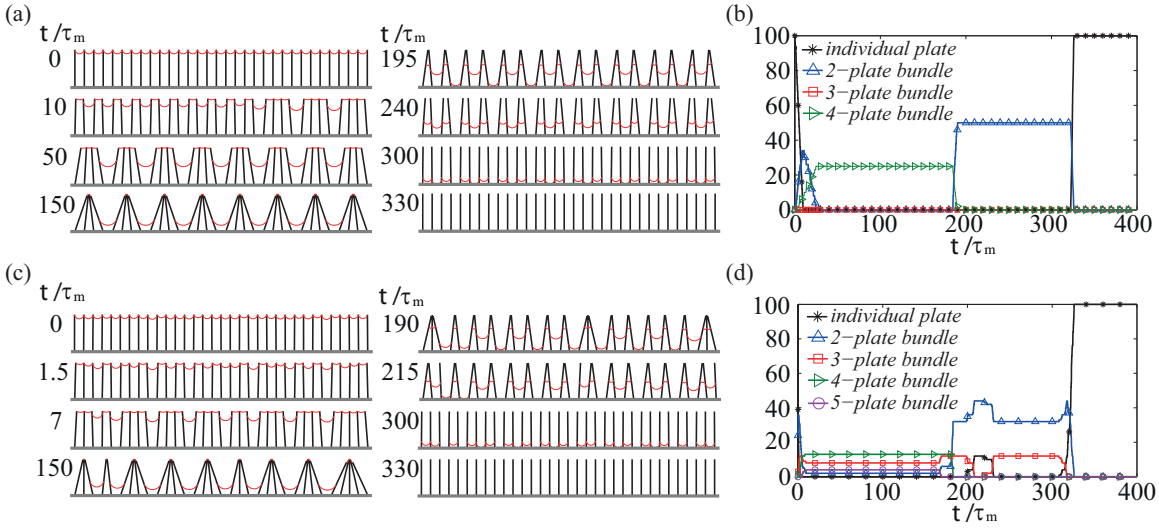

Figure 3.5: Evolution of bundle formation assuming evaporation rates to depend on the surface area in each cell. Of the periodic domain of 100 plates only 32 are displayed. (a) Snapshots of the array of pillars and menisci at different times. The initial conditions are $V_n/d = 0.92$ except that V_{99} is smaller by 2% and $\theta_n = 90^o$. (b) Number count of bundles of different size as a function of time for (a). (c) Same as (a) but with uniform random initial perturbations with the maximum amplitude of 5% on both $V_n/d = 0.92$ and $\theta_n = 90^o$. (d) Number count of bundles of different size as a function of time for (c). Note the 3- and 5-plate bundles.

Coupling to dynamics of drying

For an evaporation dominated situation, the rate at which the liquid volume in each cell is reduced depends on the local surface area of the air-liquid interface and thus on deflection angles of the adjacent lamellae. Consequently, the drying dynamics is coupled to the evolution of the geometric configuration, and new instabilities associated with inhomogeneous cell fillings are expected, which cannot be captured by either energy minimization [3, 41, 42] or renormalization analysis [43].

A minimal evaporation model that is sufficient to capture the qualitative features

of hierarchical bundle formation is given by

$$\frac{dV_n}{dt} = \begin{cases} 2\frac{t_m}{t_e} c_e r_n \beta_n & \text{when} \quad V_n > 0, \\ 0 & \text{otherwise,} \end{cases} \tag{3.21}$$

where c_e is a constant, τ_m and τ_e are time scales for mechanical relaxation and evaporation respectively, r_n is the radius of the meniscus and $2\beta_n$ is the angle subtended by the meniscus arc. Eq. (3.11) and Eq. (3.21) coupled together determine the dynamics of lamella coalescence driven by evaporating liquid. When $t_m \ll t_e$, V_n decreases quasi-statically so that Eq. (3.20) is always relaxed to the static state for a V_n. When $t_m \sim t_e$, the evolution of V_n and θ_n is coupled. When $t_m \gg t_e$, the evaporation is ultra-fast so that the lamella array does not coarsen. In our typical experiments, $\tau_m \sim 22.5ms$ and τ_e is around a few seconds, so we choose c_e correspondingly in Eq. (3.21) so that the liquid dries out in about 7 seconds. Figure 3.5 shows the simulation results for a periodic domain of 100 pillars with 2 different initial perturbations. In Figure 3.5(a), all pillars are perfectly vertical, and the liquid volume in each cell is constant for all cells except that V_{99} is smaller by 2% to mimic boundary effects in an experimental system. The evolution of the system indicates that a front of dimer coalescence propagates from the imperfection site and sweeps through the entire domain, followed by a successive front of quadrimer coalescence. The largest transient bundles have 4 lamellae. If adhesion in a real system is neglected, capillary forces are not sufficiently large to hold the pillars together, and the bundles separate symmetrically, when the liquid volume falls bellow a second threshold, the perfect vertical configuration is restored. Figure 3.5(b) presents the number of bundles of different sizes as a function of time corresponding to the configuration shown in Figure 3.5(a), we see that bundle formation/sepration is perfectly hierarchical and regular.

In Figure 3.5(c), uniform random perturbations with maximum relative amplitude of 5% are applied to all the tilting angles and liquid volume in all cells. Irregular bundles

of size ranging from 2 to 5 form transiently, and separate as the liquid evaporates. Figure 3.5(d) presents the number count of bundles of different size for Figure 3.5(c), which shows that the dimer is still the dominant mode in the early stages, but bundle formation is hierarchical yet irregular. This is because the the jump in the location of the contact line when the contact angle reaches a critical value leads to a sudden decrease in the effective stiffness as shown in Figure 3.3(a), and the uniform random initial perturbation generating multiple sites from which the front of dimer coalescence starts propagating. Consequently the sites are not necessarily separated by an even number of pillars. Therefore, trimers and pentamers also arise in addition to quadrimers. Bundles of larger size do not appear because of the large elastic energy associated with their formation.

The dynamics of both cases indicates the number of plates per cluster varying in a step-like manner, very similar to the experimental data reported by Pokroy [4] and Gat [43]. All these features agree qualitatively well with our own experimental observations (Figure 3.1(a)(b)).

3.2 Collective dynamics of a two-dimensional array of bristles

3.2.1 The three-dimensional system and experimental observations

We generalize our study of the dynamics of pillar aggregation driven by capillary effect to a two-dimensional array of epoxy nano-bristles immersed in the evaporating wetting liquid as reported in detail in previous work [4, 61]. Compared to the lamella case, there are 3 major differences. First, fluid freely flows around the multi-connected domain so that the interaction between bristles occurs over much longer ranges rather than being limited to just nearest neighbors. Secondly, the three-dimensional geometry allows the pillars to bend in

two principal directions and twist. Here, we neglect the role of twisting. This is equivalent to neglecting the role of friction between filaments. ($\partial\tau/\partial s = 0$ for twisting filaments, where τ is the shear stress and s is the arc length coordinate, so that $\tau = const = 0$ if the end is free.) Thirdly, experimentally we see that a segmented, "wormlike" geometry of the specially treated bristles increases pinning of the receding contact line by reentrant curvature [4].

The uniform array of non-interacting straight pillars again loses stability as the liquid evaporates. The dynamics of the ensuing structures is a result of the competition between elasticity and capillarity, and the morphology of the final assembly is determined by intrapillar elasticity and interpillar adhesion [61], present in the experimental setting. Figure 3.1(c)-(e) show the scanning electron microscopy (SEM) images of the assembly into uniform periodic fourfold clusters of nanopillars, in which the pillar height $L = 4.5\mu m$, the pillar radius $R = 150nm$, the pillar spacing $D = 2\mu m$, the Young's modulus $E = 0.2GPa$, the surface tension of the liquid $\sigma = 0.022N/m$, and the density of the liquid $\rho = 786Kg/m^3$. Unlike in the 1-dimensional array of lamellae, where the dimer is the primary unstable mode, for pillars the quadrimer is the primary unstable mode. As the liquid evaporates, this mode gives way to hierarchically grow into larger assemblies until they are eventually arrested by the increasing elastic resistance.

3.2.2 Model description

As in the lamellar case, inertial effects can be neglected, so that the dynamics of each pillar tip, characterized by its displacement vector relative to its base $\overrightarrow{X}(x, y)$ (Figure 3.6(a)), is given by

$$c\frac{d\overrightarrow{X}}{dt} + \overrightarrow{F}_b(\overrightarrow{X}) + \overrightarrow{F}_\sigma(\overrightarrow{X}, V) = 0, \tag{3.22}$$

where c is the drag coefficient, $\overrightarrow{F}_b$ is the elastic bending resistance force at the tip, $\overrightarrow{F}_\sigma$ is the capillary driving force due to surface tension σ, and V is the liquid volume inside the system. The dominant contribution to c is from the internal damping of the viscoelastic solid similar to the lamellar case, and $c \approx 3t_m \pi E R^4/4L^3$ (Appendix B.4), where $t_m \sim 10^{-2}s$ is the time scale for the fiber to relax mechanically.

To compute the bending resistance force $\overrightarrow{F}_b$ in the horizontal direction, we employ Euler's elastica theory. Assuming ϑ is the angle of the bristle centerline tangent with the vertical direction, $s \in [0, L]$ is the arc length coordinate, and $|\overrightarrow{F}_b|$ is the shear force amplitude, equilibrium yields

$$\frac{\pi}{4} R^2 E \vartheta_{ss} + |\overrightarrow{F}_b| \cos\vartheta = 0, \tag{3.23}$$

Geometry implies that $|\overrightarrow{X}| = \int_0^L \cos[\vartheta(|\overrightarrow{F}_b|)]ds$, so given $\overrightarrow{X}$, $|\overrightarrow{F}_b|$ is uniquely determined, and $\overrightarrow{F}_b = |\overrightarrow{F}_b|\overrightarrow{X}/|\overrightarrow{X}|$.

To obtain $\overrightarrow{F}_\sigma$, we need to determine the shape of the air-liquid interface. Since the Bond number $Bo \sim 10^{-6} \ll 1$, gravity can be neglected. Moreover, the time scale for the fluid to equilibrate in the porous brush t_f is much smaller than that for the bristles to relax mechanically t_m, which is much smaller than that for the evaporation t_e, i.e. $t_f \sim 10^{-3}s \ll t_m \sim 10^{-2}s \ll t_e \sim 10^{0}s$ (Appendix B.5). Therefore, the pressure throughout the liquid domain can be regarded uniform. Then the air-liquid interface $z = S(x, y)$ has uniform mean curvature and thus satisfies

$$2\sigma H = \sigma \frac{(1+S_x^2)S_{yy} - 2S_x S_y S_{xy} + (1+S_y^2)S_{xx}}{(1+S_x^2+S_y^2)^{3/2}} = p, \tag{3.24}$$

where H is the mean curvature of the interfacial surface, and without loss of generality, we have implicitly set the ambient pressure 0, and p is the pressure inside the liquid. Volume

conservation in the whole domain yields

$$V = \int_A S(x,y)dxdy + \pi R^2 \sum_{i=1}^{N}(h_i - L), \tag{3.25}$$

and serves to determine p. Here A is the projected domain of the air-liquid interface to the horizontal plane (meshed area in Figure 3.6(a)), and h_i is the elevation of i^{th} pillar tip. Since the menisci are always pinned on the pillar tips, We need to solve Eq. (3.24) on a multi-connected domain, in which pillar tips are regarded as solid circles with the identical radius (Figure 3.6(a)) and the height of the surface is fixed at the elevation of pillar tips (Figure 3.6(b)) $h = \int_0^L \sin\vartheta ds$ calculated from Eq. (3.23). As the bristles are effectively immersed in liquid, the integration of pressure over the lateral surface of the cylinder does not contribute to $\overrightarrow{F}_\sigma$, and the only active contribution is the line tension at the contact line. For a given air-liquid interface (Figure 3.6(c)), the angle of the meniscus tangent with the horizontal direction on the circular boundary of the tip is known, which we denote as φ. To calculate the the capillary driving force on each bristle, we integrate the surface tension over the contact line contour at the tip and only the component in the horizontal direction contributes to the deflection, so that $\overrightarrow{F}_\sigma = \oint_c \sigma \overrightarrow{n} \cos\varphi ds$, where the subscript c represents the tip circle and $\overrightarrow{n}$ is the unit out normal of the circle. Note that for very small values of V, the assumption of the surface being pinned at the pillar tips breaks down. The clusters are however chosen well before the assumption is violated and thus does not affect our results.

To avoid the complication of contact and prevent penetration upon collision, we treat each pillar as a rod with finite radius, and add an artificial short range repulsion force when two circles representing pillar tips come close enough (10% of the pillar diameter), but do not consider the elastic deformation of the cross section due to contact.

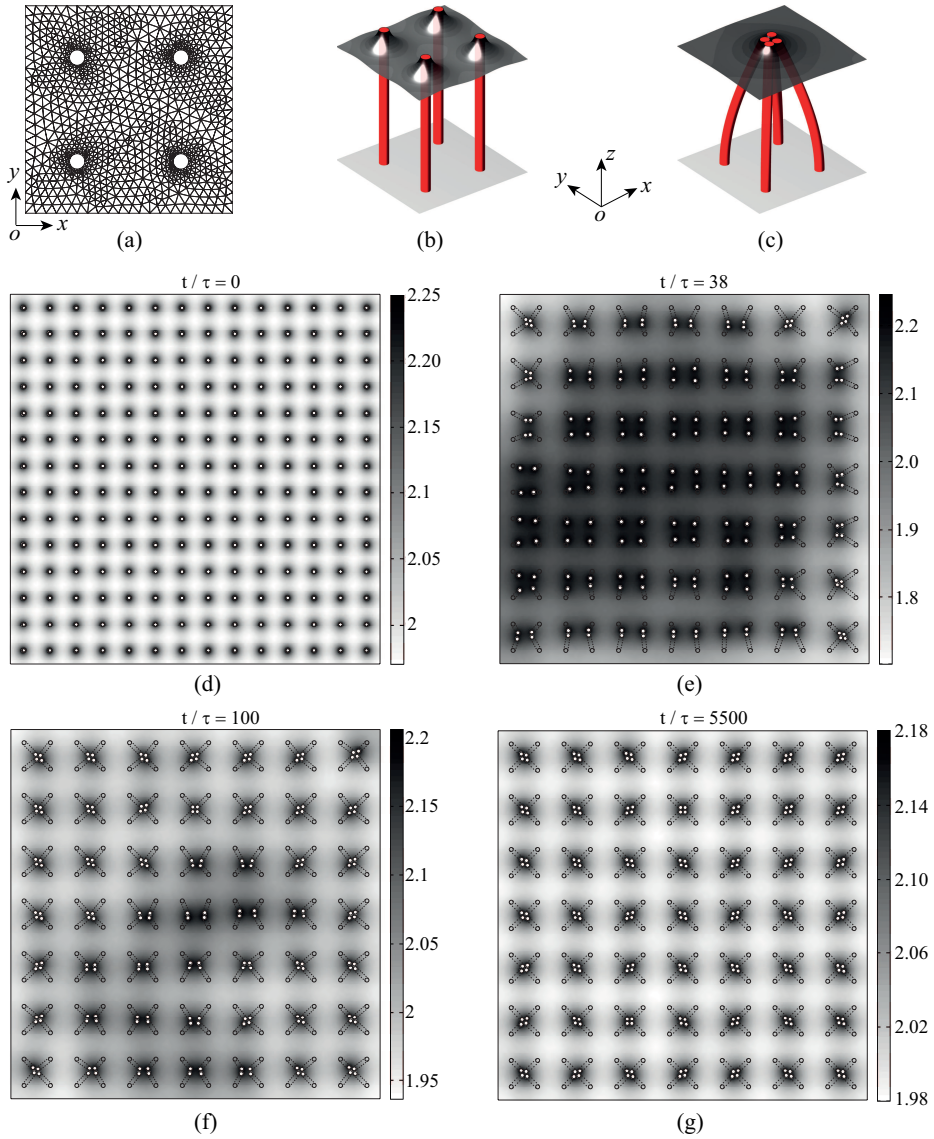

Figure 3.6: (a) Demonstration of triangular meshes on a domain that contains an array of 2 by 2 pillars, where the white solid circles represents pillar tips. The mesh density used in the actual simulation is 4 times denser. (b) Three-dimensional visualization of air-liquid interface on the domain shown in (a) for a given liquid volume $V/V_{flat} = 0.85$. (c) Given a slight perturbation to (b), 4 pillars move towards each other to form a bundle. (d)-(g) A domain of 14 by 14 pillars is evolving to the steady state of fourfold clusters for a given liquid volume $V/V_{flat} = 0.85$. τ is the dimensionless time scaled by τ_m (see text). The gray scale shows the air-liquid interface height, which is scaled by the pillar spacing. White solid circles represent pillar tips, and the black open circles represent pillar bases. The dashed lines connecting bases and tips could be thought of as a projection of pillars viewed from the top.

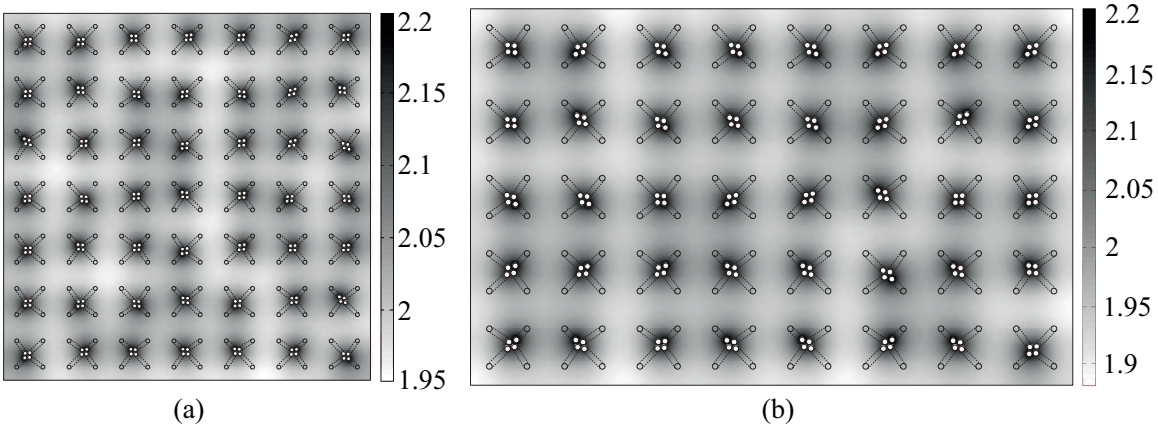

Figure 3.7: Final structures of the fourfold clusters for different prescribed volumes and domain sizes. (a) $V/V_{flat} = 0.90$. (b) $V/V_{flat} = 0.88$.

3.2.3 Simulation results and comparison with experiments

Symmetric boundary conditions are applied on the straight boundary walls and pinned contact lines are assumed on all pillar tips. The distance between the boundary walls and pillar bases of the boundary layer is half of the pillar spacing. For initial conditions, the pillar bases (open circles in Figure 3.6(g)) form a perfect periodic square lattice. The pillar tips (solid white circles in Figure 3.6(g)) are perturbed from the vertical configuration so that the layer of pillars closest to the boundaries inclines inwards to trigger the inward motion from the boundaries, and other pillar tips are uniformly and randomly perturbed. We numerically evaluate the coupled evolution equations using a custom-coded finite element code. For a given pillar tip displacement $\overrightarrow{X_i}$, Eq. (3.23) is solved with the geometric condition $|\overrightarrow{X}| = \int_0^L \cos[\vartheta(|\overrightarrow{F}_b|)]ds$ to determine the reaction force $\overrightarrow{F}_{bi}$ and tip elevation of each pillar h_i. Given $\overrightarrow{X_i}$ and h_i, Eq. (3.24) is solved using the finite element method to determine the interface $S(x, y)$ on the multi-connected domain under the liquid volume constraint Eq. (3.25), which determines p and thence $\overrightarrow{F}_{\sigma i}$. Then Eq. (3.22) is integrated in time explicitly to update the pillar tip positions, and the domain is remeshed accordingly

at every time step.

Figure 3.6(d)-(g) show the simulated evolution of an array of 14 by 14 bristles collapsing into fourfold bundles at a prescribed liquid volume of $V/V_{flat} = 0.85$, where V_{flat} is the control volume inside the system when all the bristles are vertical and air-liquid interface is flat, using the parameters from experiments in Figure 3.1(c)-(e). Due to the initial perturbations, coalescence initiates from the boundary and propagates towards the center of the domain. We observe that similar to the case of lamellae, there exists a critical liquid volume above which uniform vertical pillars are stable, and below which pillar coalescence occurs. The primary fourfold eigenmode (Figure 3.6(e)) is universal upon instability independent of initial perturbations as observed in both experiments and simulations (Figure 3.6(g) and Figure 3.7). An intuitive way to understand this is to decompose the fourfold bundles into the two principal directions, which results in dimers in each direction. Although the interaction potential between pillars in the three-dimensional case is longer range than in the two-dimensional case because of connectivity, it is the strongest to the nearest neighbors. Provided that within the linear analysis the effective spring constants in the two principal directions are decoupled, the dimer is the primary mode in each direction as in the one-dimensional lamella array. Beyond the linear regime, our simulation can precisely capture the maximum bundle size. We also note that the tips in a bundle can form either rhombi or squares depending on the initial perturbations although rhombi are more likely. Since we neglect friction between the tips, the rhombus is a more energetically favorable configuration than the square. However, the energy difference between these two states is very small, so that contact and friction in real experiments leads to both square tips (Figure 3.1(d)) and rhombi tips (Figure 3.1(c)).

3.3 Summary

We have studied the dynamics of bundle formation driven by drying liquid for two characteristic problems in two and three dimensions. For the lamellar case, we explicitly derive all torques in terms of the state variables - tilting angles θ_n and liquid volumes V_n, and the relevant geometrical and physical parameters. Based on these results, the linear stability analysis captures the primary 2-plate-collapse eigenmode, but does not predict the nonlinear coarsening of the clusters. Full numerical simulations show that the final states sensitively depends on initial perturbations because of the jump in the location of the contact line when the contact angle reaches a critical value. This leads to an effective stiffness that suddenly decreases as shown in Figure 3.3(1). Therefore, self-organization of clusters cannot be predicted by energy minimization arguments but depend on the dynamics of the drying process - this is especially true when the coupling of geometry to local evaporation rates is taken into account. For the three-dimensional bristle case, our numerical method captures the primary fourfold eigenmode associated with the onset of collapse, which can be intuitively understood as the superposition of the dimer modes in two principal directions. Once again, the full dynamics predicts the final stable state, which is determined by the competition between capillarity and elasticity. For both cases, our numerical results agree well with many of the salient experimental observations. In particular, we can explain the eigenmodes at the onset of instability and the time scales on which clusters form, give dynamical predictions of both regular and irregular hierarchical bundle formations, and capture the final state.

We end our discussion with open questions. More careful studies can be carried on by considering the surface adhesion effect after lamellae or pillars are in contact, which may lead a different final distribution of cluster size. Also, both the adhesion effect and

twisting of pillars need to be considered to explain the formation of chiral clusters after pillars are in contact, as shown in the three-dimensional case. Finally, a continuum theory that addresses the explicit connection to the essential geometric and physical parameters that influence the maximal size and dynamics of the assembly remains an open question.

We thank Sam Okco for many discussions that helped to sharpen and clarify our arguments.

Chapter 4

Dynamics of elastocapillary coalescence and arrest

Here, We describe the elastically-limited coarsening of a one-dimensional array of lamellae immersed in an evaporating liquid. Starting from a discrete microscopic model of the process, we derive a mesoscopic continuum model for the coalescence and arrest of the lamellae. Our model couples the inhomogeneous dynamics of drying and capillary forcing to the elastic bending of the lamellae. Our model is consistent with the onset of the primary unstable mode seen in experiments and further captures the coalescence of pillars, their elastic arrest and the eventual separation of bundles as the liquid dries out.

We consider a one-dimensional array of evenly spaced mirco-lamellae that are made of the incompressible material with Young's modulus E, and have height L, thickness h and uniform spacing D [2] (see Fig. 4.1). Each lamella is anchored at one end on a substrate and free at the other. The array is initially completely immersed in a liquid with an air-liquid surface tension σ. When the liquid evaporates, the liquid remains confined between two neighboring lamellae which define a cell. During this process, capillary forces

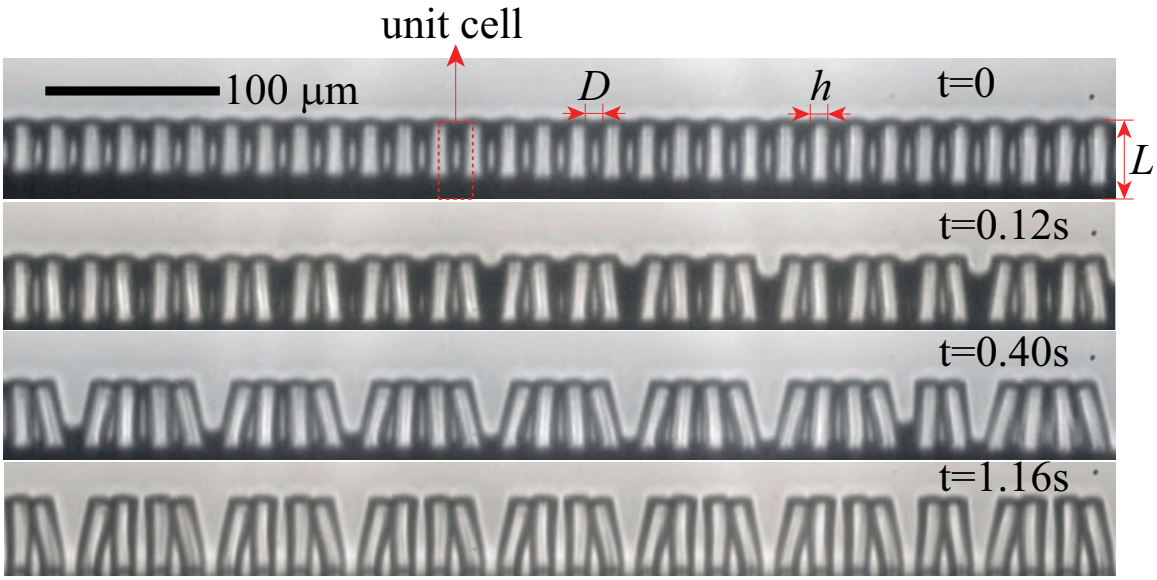

Figure 4.1: (a) Experimental snapshots of 2-dimensional lamellar coalescence driven by an evaporating liquid. The lamellae are made of polydimethylsiloxane (PDMS) with pre-polymer and cross-linker weight ratio 10:1 and Young's modulus $E = 1.275Mpa$. The geometric parameters are pillar height L, thickness h, and spacing D with $L = 4h = 4D = 40\mu m$. The liquid is isopropyl alcohol (IPA), with an interfacial tension $\sigma = 0.022N/m$. As the liquid evaporates, lamellae bundle to form dimers, quadrimers and other hierarchical structures. As the liquid dries out, bundles separate out in the reverse order if the surface adhesion due to contact is not strong enough to counterbalance the bending resistance.

associated with the liquid-air menisci between the free ends of the soft lamellae can cause them to deflect laterally and adhere together. In the experiment, we observe a cascade of successive sticking events that leads to a hierarchical bundling pattern: pairs of neighboring lamellae tilt towards each other to form a dimer; these dimers collapse to form quadrimers, and so on. This process repeats until the increasing elastic resistance eventually arrests the coarsening. After the liquid dries out, the bundles separate into lamellae if the adhesion between lamellae is not strong to counterbalance the elastic forces; otherwise they persist.

4.1 Brief review of the discrete model

We adopt a Bloch-wave like analysis [62] for our periodic mechanical system which consists of $2N$ vertical lamellae and the same volume of liquid V confined in each cell. If $\overrightarrow{M}$ is the vector of moments on all plates and $\overrightarrow{\theta}$ is the vector of deflection angles of all plates, we can write

$$M_n = -k_c l^2 \partial_d^2 \theta_n + k_b \theta_n, \tag{4.1}$$

where M_n is the local moment on the n^{th} plate, θ_n is the deflection angle of the n^{th} plate, $l = D + h$ is the size of the unit cell, $k_c(\sigma L, V/L^2)$ is the capillary stiffness, $k_b = Eh^3/3L$ is the bending stiffness (see Appendix), and $\partial_d^2 \theta_n = (\theta_{n+1} - 2\theta_n + \theta_{n-1})/l^2$ is the discrete Laplacian. Then the stiffness matrix $d\overrightarrow{M}/d\overrightarrow{\theta}$ has eigenvalues $s(f)$ and eigenvectors $\Psi(f)$ given by

$$s(f) = -2k_c \cos(f) + 2k_c + k_b, \tag{4.2}$$

$$\Psi(f) = [1, e^{if}, e^{2if}, \ldots, e^{i(2N-3)f}, e^{i(2N-2)f}, e^{-if}] \tag{4.3}$$

respectively, where $f = n\pi/N$ with $n = 1, 2, \ldots, 2N$.

From (4.2), we see that when $k_c \geq 0$, $s \geq k_b > 0$, and the vertical base state is stable. When $k_c < 0$, the smallest eigenvalue is $s(\pi) = 4k_c + k_b$ corresponding to $f = \pi$, reflecting the fact that stability is controlled by the competition between elasticity and capillarity. As $k_c = k_c(V)$, this eigenvalue can switch sign so that $s(\pi) < 0$ for a range of V where the system is unstable. For this case, we see from (4.3) that the eigenvector of the primary mode is $[1, -1, 1, -1, \ldots, 1, -1]$, corresponding to the dimerization two-lamella-collapse mode observed from the experiments. Beyond the onset of instability, we have to numerically determine the aggregation dynamics using the discrete model (Appendix C). Alternatively we can develop a long-wavelength continuum theory that unifies the linear and nonlinear dynamics of the system to explain elastically arrested phase separation.

4.2 Continuum model

In our continuum model, we consider a binary fluid that is composed of two constituents: the tips of the lamellae and gaps between them. Denoting ϕ as the concentration field of the binary fluid, with $\phi = -1$ corresponding to gaps and $\phi = 1$ to tips, the equation describing the phase separation is given by

$$\partial_t \phi = -\partial_x J = a_0 \partial_x^2 \frac{\delta U}{\delta \phi}, \tag{4.4}$$

where $\partial_t = \partial/\partial t$, $\partial_x = \partial/\partial x$, $\partial_x^2 = \partial^2/\partial x^2$ etc., and J is the flux. The first equality in (4.4) follows from mass conservation and the last equality follows from the assumption that the flux is proportional to the gradient of the chemical potential $\partial_x(\delta U/\delta\phi)$, where a_0 is the diffusion constant and $U(\phi)$ is the free energy of the system that includes the bending energy of lamellae, the surface energy of the air-liquid interface, and the potential energy associated with the pressure gradient across the lamella. It is simplest to write the free energy $U(\theta)$, where θ is the deflection angle field, and then relate ϕ to θ. In the linear deformation regime where $|\theta| \ll 1$,

$$U(\theta) = \int_0^{\mathcal{L}} \frac{M\theta}{2l} dx, \tag{4.5}$$

where $\mathcal{L}$ is the system size, and M is the local moment given by (4.1). In the continuum limit, letting $\theta(x) = \theta_n$, $\theta(x + l) = \theta_{n+1}$ and $\theta(x - l) = \theta_{n-1}$, and substituting into the expression for the discrete Laplacian $\partial_d^2\theta$, we get

$$\partial_d^2 \theta = \partial_x^2 \theta + \frac{l^2}{12} \partial_x^4 \theta + O(\partial_x^6 \theta). \tag{4.6}$$

The expression (4.6) is asymptotically correct only when the wave number $k \ll 1/l$, as can be readily seen from its Fourier transformation $[2\cos(kl) - 2]/l^2 = -k^2 + l^2k^4/12 + O(k^6)$, and breaks down when $kl \gg 1$, since $[2\cos(kl)-2] \in [-4, 0]$, while $[-(kl)^2+(kl)^4/12] \to +\infty$ as $k \to \infty$.

Substituting Eqs. (4.1) and (4.6) into the expression (4.5) gives us

$$U(\theta) = \int_0^{\mathcal{L}} \left[-\frac{k_c l}{2}\theta \left(\partial_x^2 \theta + \frac{l^2}{12}\partial_x^4 \theta \right) + \frac{k_b}{2l}\theta^2 \right] dx. \tag{4.7}$$

To relate the plate deflection angle field θ to the concentration filed of the binary fluid ϕ, we note that in the uniform state, the reference concentration is $\phi_0 = (h - D)/l$. After the lamellae are deflected by θ, the current concentration field is given by $\phi(x) = [h - (D - lL\partial_x\theta)]/l(1 - L\partial_x\theta) = \phi_0 + (2hL/l)\partial_x\theta + O[(\partial_x\theta)^2]$. Integrating $\phi(x)$ once allows us to write $\theta(x) = (l/2hL)\int_0^x \bar{\phi} dx'$, where $\bar{\phi} = \phi - \phi_0$ is the difference between the current and the reference concentration. Substituting this into (4.7) gives us

$$U(\bar{\phi}) = \int_0^{\mathcal{L}} \left[-\frac{a_c}{2}\int_0^x \bar{\phi} dx' \left(\partial_x \bar{\phi} + \frac{l^2}{12}\partial_x^3 \bar{\phi} \right) + \frac{a_b}{2}\left(\int_0^x \bar{\phi} dx' \right)^2 \right] dx, \tag{4.8}$$

where $a_c = k_c l^3/4h^2L^2$ and $a_b = k_b l/4h^2L^2$ are determined by capillarity and elasticity.

Substituting (4.8) into (4.4), we get the evolution equation

$$\partial_t \bar{\phi} = a_0 a_c \partial_x^2 \left(\bar{\phi} + \frac{l^2}{12}\partial_x^2 \bar{\phi} \right) - a_0 a_b \bar{\phi}, \tag{4.9}$$

where the last term comes from the variation of the elastic bending energy[1]. To understand the onset of instability of the homogeneous vertical state, we derive the associated dispersion relation by substituting $\bar{\phi} = \exp(\omega t + ikx)$ into (4.9) to get,

$$\omega = a_0 a_c \left(-k^2 + \frac{l^2}{12}k^4 \right) - a_0 a_b. \tag{4.10}$$

When $a_c < 0$, the fastest growing mode corresponds to the wave number $k_m = \sqrt{6}/l$ and the wavelength $\lambda_m \approx 2.57l$. We see that the continuum model qualitatively captures the primary mode of instability, although there is a quantitative discrepancy compared to the discrete model ($\lambda_m = 2l$), because the condition $kl \ll 1$ is not strictly satisfied. When

[1]This term looks nonconservative, but it is derived from $a_0 a_b \partial_x^2 [\int_0^x dx_1 \int_0^{x_1} \bar{\phi}(x_2) dx_2]$, which is in fact conservative

$a_c > 0$, from (4.10) we see that $\omega \to \infty$ as $k \to \infty$ for any finite a_b. This failure to predict a stable state is inconsistent with both the experimental observations and the discrete model, because (4.6) breaks down when $kl \gg 1$. To fix this, we keep the first order term in the expansion (4.6) when $a_c \geq 0$, so that $\omega = -a_0(a_c k^2 + a_b) < 0$. Therefore, (4.9) becomes

$$\partial_t \bar{\phi} = a_0 a_c \partial_x^2 \left(\bar{\phi} + a_1 l^2 \partial_x^2 \bar{\phi}\right) - a_0 a_b \bar{\phi}, \tag{4.11}$$

with a_1 modified to a piecewise constant, i.e. $a_1 = 1/2\pi^2$ when $a_c < 0$, and $a_1 = 0$ when $a_c \geq 0$ to capture the wavelength at the onset of instability.

Beyond the linear regime, we modify the functional form of the free energy $U(\bar{\phi})$ by adding a semi-phenomenological term into (4.8). Since the system can eventually separates into two phases of tips or gaps in the absence of an elastic field, the energy density should have two minima at $\phi = \pm 1$, suggesting a double well potential $a_c(\phi^2/2 - \phi^4/4)$, as in the Cahn-Hilliard equation [63]. Indeed, a comparison with (4.8) suggests that ϕ^2 may be a better alternative to $-(\int_0^x \bar{\phi} dx')\partial_x \bar{\phi}$ (the first term in the right hand side of (4.8)) as they have the same spectrum and the former has a smaller continuity requirement. The ϕ^4 term is the first nonlinear term allowed by the symmetry of the system associated with $(\partial_x \theta)^4$ that was neglected in (4.7) and causes the pattern amplitude to saturate.

To account for the inhomogeneity of the liquid volume in the cells, we note that the capillary stiffness k_c should be replaced by $k_c' = \sigma L f(\widetilde{V})$ with $f(\widetilde{V}) = c_c \widetilde{V}(\widetilde{V} - \widetilde{V}_c)$ being a dimensionless function that accounts for the non-monotonic nature of the capillary force as a function of the dimensionless liquid volume $\widetilde{V} = V/DL$. Omitting the tilde henceforth for simplicity of notation, we note that when $V \geq V_c$, we get stable lamellae; when $V \leq V_c$, we get unstable lamellae; when $V \to 0$, $f(V) \to 0$, and we get stable lamellae again. Here the positive constant c_c can be numerically computed from the discrete model to set the correct amplitude of k_c', and $V_c = V_c(D/L)$ is the critical volume at which k_c switches sign

and can also be explicitly calculated.

Then the dimensionless form of (4.4) is given by

$$\partial_\tau \phi = \partial_s^2 \left[c_c V (V - V_c) \left(\phi - \phi^3 + c_1 \partial_s^2 \phi \right) \right] - c_b (\phi - \phi_0), \tag{4.12}$$

where $\tau = t/t_c$, $t_c = 4h^2 L / a_0 \sigma l$ is the time scale at which lamellae deflect (coarsening time scale), $\partial_s = \partial / \partial s$, $s = x/l$, $c_b = k_b / \sigma L$, $c_1 = 0$ when $V \geq V_c$ and $c_1 = 1/2\pi^2$ when $V < V_c$. V can be either a constant or a spatial and temporal function.

4.3 Numerical results

In Fig. 4.2, we show the numerical solutions of Eq. (4.12) using a spatially uniform V as the control parameter with periodic boundary conditions and random perturbations of V and/or ϕ as initial conditions, computed using the commercial finite element package COMSOL4.3a. We see that for $V < V_c$, phase separation results with either a finite amplitude and dimensionless wavelength 2 [Fig. 4.2(a)] for small $f(V)$, or a hierarchically coarsened pattern with dimensionless wavelength 4 [Fig. 4.2(b)] for large $f(V)$. Since $f(V)/c_b$ represents the ratio of capillary driving forces to the elastic bending resistance, the results show that the largest bundle size depends on the competition between these two effects; indeed, for softer lamellae with smaller k_b, coarsening may continue beyond wavelength 4 until the increasing elastic resistance eventually arrests it.

If the dynamics of coalescence is coupled to evaporation, we need a dynamical law for the change in V. We assume that the evaporation rate is proportional to the area of liquid-air interface and thus to both the local gap concentration $(1 - \phi)/2$ and the liquid volume V. Then, the dimensionless equation that governs the evolution of liquid volume is

$$\partial_\tau V = \begin{cases} -\frac{t_c}{t_e}(1 - \phi) V & \text{when} \quad V > 0, \\ 0 & \text{otherwise,} \end{cases} \tag{4.13}$$

where t_e is the evaporation time scale.

In Fig. 4.3, we show the results for the case of the dynamics of lamella aggregation driven by an inhomogeneously evaporating liquid, obtained by solving (4.12) and (4.13) simultaneously with the same boundary and initial conditions used in Fig. 4.2. The evaporation time scale and the coarsening time scale are well separated ($t_e = 10t_c$) so that V decreases quasistatically. During the early stages of evaporation when $V > V_c$, the homogeneous state is insensitive to perturbations. When $V < V_c$, the dimensionless wavelength 2 in the unstable mode captures the dimerization observed in the experiments and the largest domain size 4 beyond the linear regime are also in good agreement with the observation of quadrimers (see Fig. 4.1). Our model also naturally captures refining of domains when $V \approx 0$, describing the separation of bundles in the absence of interpillar adhesion. Then, the system is restored to its homogenous state $\phi = \phi_0$ on complete drying.

4.4 Summary

Our continuum model of dynamical coalescence driven by capillarity and eventually arrested by elasticity arises from a physically consistent discrete microscopic model. It captures the onset of instability and the primary unstable mode, and describes the dynamics of lamellar coalescence with elastic arrest, followed by the bundle separation, in terms of an elasto-capillary field theory coupled to evaporation dynamics that accounts for long wavelength inhomgeneities in space and time. Of particular significance is that all the coefficients in our model are directly linked to microscopic measurable physical and geometrical parameters in the experiments, allowing for a clear test of our theory.

More broadly, our continuum theory Eq. (4.12) is similar to the classical Cahn-Hilliard theory for phase separation [63] with an important difference due to the elastic

contribution $\phi - \phi_0$. This term is the origin of the refining driven by elastic resistance that competes with the coarsening driven by surface tension. Together, they determine the stability of the system and arrest the coarsening at an equilibrium size. Given that aggregation dynamics with arrested phase separation is observed in a variety of physical systems, such as two-phase epitaxial monolayer grown on an elastic substrate [64, 65, 66, 67] or phase separation in an electrochemically active nanoporous sponge[68], this class of theories ought to be broadly applicable. Indeed, a phenomenological model used to describe the evolution of nanoporosity in dealloying [68] is almost the same as Eq. (4.12), although the underlying physics is fundamentally different and the model is not derived microscopically.

Natural generalizations of our model include accounting for the role of surface adhesion between contacting lamellae, and an anisotropic 2-dimensional theory for the coalescence of bristles [4] to capture the orthotropic and other symmetries in these systems.

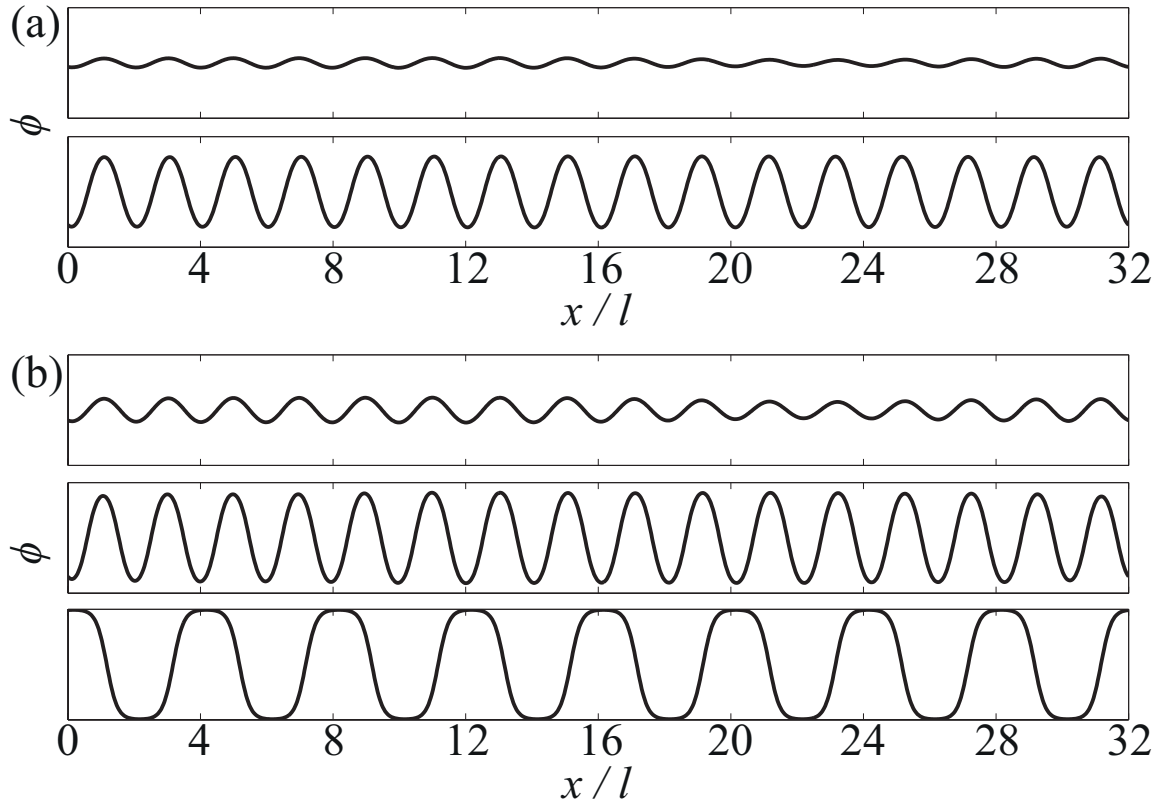

Figure 4.2: The onset, evolution, and steady state of elastocapillary phase separation for an imposed homogenous liquid volume V, obtained by solving (4.12) on a periodic domain of length 32, corresponding to an array of 32 lamellae. A random perturbation with the amplitude of $\phi = 10^{-5}$ is prescribed as the initial condition. Using the parameters for the experiments shown in Fig. **??**, we set $c_c = 4500$, $V_c = 0.95$, $c_b = 10$, and $\phi_0 = 0$ in (4.12). All figures have the same scale, and the range of the vertical axis is $[-1, 1]$. (a) $V = 0.949$. The dimensionless wavelength of the primary mode is 2, and we see that the pattern saturates at a finite amplitude and stabilizes without coarsening. (b) $V = 0.8$. The pattern saturates at a finite amplitude by coarsening and stabilizing to form periodic domains of size 4.

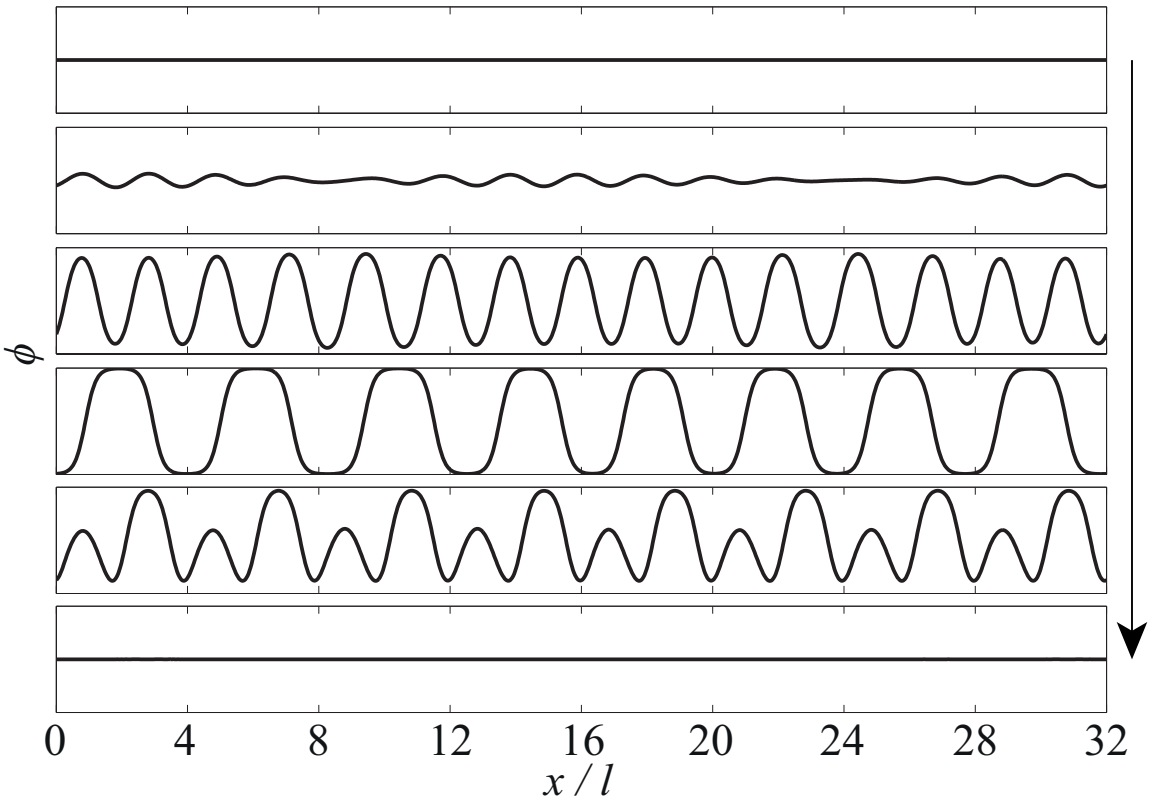

Figure 4.3: The onset, evolution and steady state of elastocapillary phase separation coupled to evaporation dynamics obtained by solving (4.12) and (4.13) simultaneously. The initial conditions are $V = 1$ and $\phi = 0$, and an initial random perturbation of amplitude $\phi = 10^{-5}$. Using the experimental parameters in Fig. **??**, we set $c_c = 4500$, $V_c = 0.95$, $c_b = 10$, $\phi_0 = 0$, $t_1 = 0.02s$ and $t_2 = 0.2s$. All figures have the same scale, and the range of the vertical axis is $[-1, 1]$. Time increases in the direction of the arrow, corresponding to dimensionless times τ are 0.64, 0.714, 0.8, 6, 58, and 140. At $\tau = 0.65$, $V > V_c$, and the system is still stable at $\phi = 0$. As V decreases with time, the system becomes unstable to the primary mode of instability that gradually coarsens. An elastic refining process at very small V appears naturally, as in the experimental observations, and corresponds to bundle separation. At late times, as $V \to 0$, i.e. when the liquid has almost completely evaporated, the system is restored to its initial state with $\phi = 0$.

Chapter 5

Studies on fingering instabilities in a confined elastic film

5.1 Geometric model for adhesive instabilities

The growth of an interface between two domains has been widely observed in a host of patterns formed in nature. One of the most familiar examples is the evolution of a snowflake crystal via the process of solidification [69]. Other systems which exhibit similar behavior include classical hydrodynamic free-surface instability associated with the relative motion between liquids of different viscosities in a narrow gap [50, 51], crack growth in solid materials [70, 71], and biological cell differentiation [72]. In all of these systems, there exists a moving boundary between two phases, on which competing stabilizing and destabilizing forces act. The physical origins of these forces depend on the particular system under investigation. The equations that describe the moving interface are often quite complicated, and not analytically tractable. Consequently, there have been extensive numerical studies using phase field models applied in this area, such as solidification dynamics [73], fracture

dynamics [74, 75], viscous fingering [76] and vesicle dynamics [77]. Relatively few works, however, take a different approach to investigate such problems, namely to construct geometrically motivated models for interfacial growth [78, 79]. Clearly, this class of models is not a fully realistic alternative to the actual evolution equations which will correctly reproduce all the intricacies of the long-time development of the system. Nevertheless, these models are purely based on general geometric considerations, and can therefore be applied to a wide variety of growth dynamics. They greatly condense information and are useful for understanding the relevance of various analytic structures. Here, in the same spirit, we revisit the problem of fingering instability that arises from peeling a thin plate from a soft confined adhesive film [5], and propose a geometric model to capture the major quantitative features of the crack front in a minimal mathematical setting.

First, we briefly describe the problem and review the work that has been done to understand the underlying physics of the phenomena. In Fig. 5.1(a), we show the schematic for such an experiment where a thin flexible cover-slip is peeled off from a soft, thin elastic adhesive film that is itself attached firmly to a rigid substrate. Fig. 5.1(b) shows the instabilities at the crack front, in the form of wavy undulations that develop during the opening of the crack but remain stable even after the crack comes to a complete rest. More experimental pictures corresponding to different film thicknesses are presented in Fig. 5.2(a) and Fig. 5.3(a). It has been shown by previous work [49] that there is a threshold for the onset of the instability that is dependent on the ratio of two length scales that arise naturally in the problem: the thickness of the film h and an elastic length $(B/\mu)^{1/3}$ defined by the stiffness of the plate B and that of the film μ. A linear stability analysis predicts that the wavelength of the instability λ scales linearly with the film thickness, namely $\lambda \approx 3.4h$, which is in a reasonable agreement with the corresponding experimental values of $\lambda_{exp} \approx 4h$ [5]. However, the linear theory loses its predicative power when the crack front evolves into

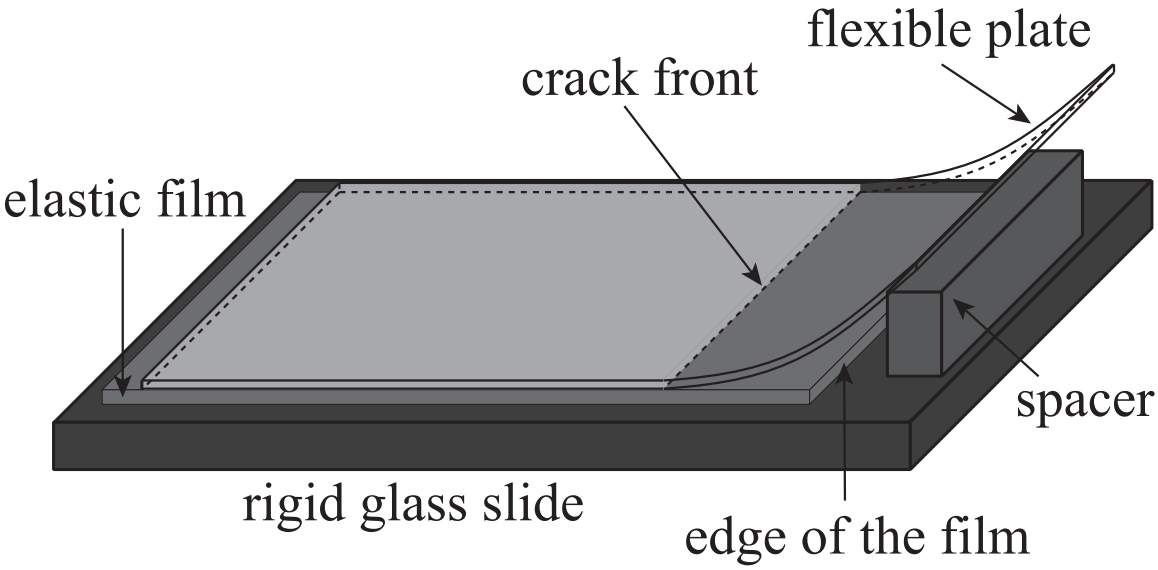

(a)

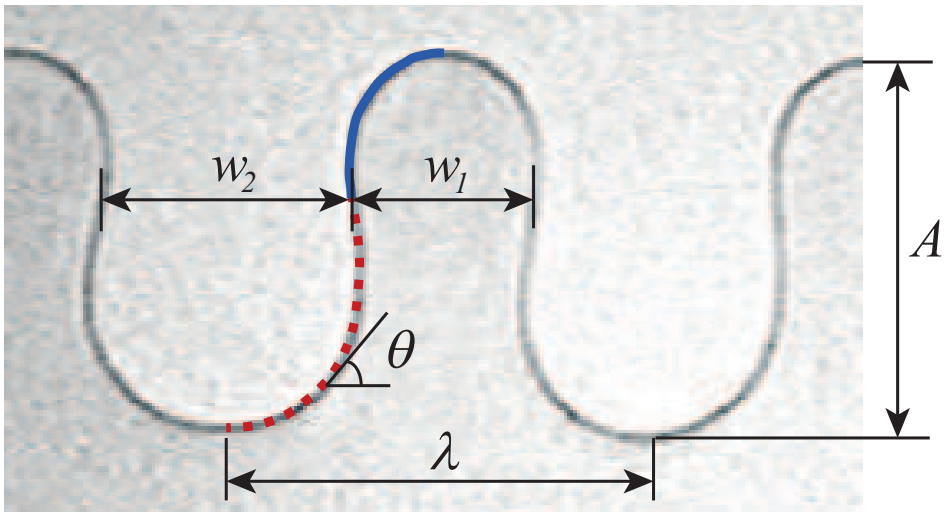

(b)

Figure 5.1: (a) Schematic of the problem. (b) The crack front loses stability to an undulatory mode when the confinement parameter $\alpha = (B/\mu h^3)^{1/3}$ is large enough [49], where B is the bending stiffness of the flexible plate, μ is the shear modulus of the elastic film and h is the thickness of the film. A is the amplitude of the finger, λ is the wavelength of the undulatory crack front, and w_1 and w_2 are the widths of the fingers protruding in and out respectively. θ is the angle spanned by the tangent of the crack front with respect to the horizontal direction. The counterclockwise direction is deemed as positive. θ increase from 0 to the maximum value on the red dotted line and decreases from the maximum value to 0 on the blue curve.

a finite amplitude.

We regard the crack front as a two-dimensional ($2D$) curve because of the geometric confinement and scale separation in the thin elastic film (the film thickness is much smaller than the width). Our geometric model that the curve obeys needs to capture the wavelength at the onset of instability, the finger amplitude A, and the widths of fat and thin fingers. Borrowing ideas from the equation describing the Euler's elastica [80], we use θ as the dependent variable, where θ is the angle spanned by the tangent vector of the crack contour with respect to the horizontal direction, and arclength s as the independent variable. Based on the fact that fingers are symmetric, the "phase separation" of θ away from the homogenous state ($\theta = 0$) always ends up with the same amplitude of mountain and valley value. Nonetheless, as the fingers could be thin or fat, the length scale of the transition from mountain to valley is not necessarily the same as that from valley to mountain (i.e. the arc lengths of the red dotted curve and the blue solid curve in Fig. 5.1(b) are not the same). This means that the periodic curve of θ can be asymmetric, tilting either to the left or to the right. Keeping those essential facts in mind, we can write down the dimensional equations describing the evolution of the $2D$ curve as

$$\begin{aligned} \frac{\partial \theta}{\partial t} &= c_1 \left(\theta - \frac{\theta^3}{\theta_{max}^3} \right) + [c_2 + f(\theta_s)]\theta_{ss} + c_3 u, \\ u_{ss} &= \theta, \end{aligned} \tag{5.1}$$

where $s \in [0, L]$, and the total arc length $L(t)$ is also a function to be determined. The overdamped dynamics is used here because the curve is massless and no oscillations are observed on the crack front development. The ideas embedded in the right hand side of the first equation in Eq. (5.1) are as follows. θ drives the phase separation away from the homogenous state. As the fingers are symmetric, θ^2 must vanish, and the next nonlinear term to saturate the finger amplitude in the expansion is θ^3 . The maximum θ in the curve scales with θ_{max}. By tuning the maximum angle θ_{max}, we can control the finger profile

to be either a graph or not depending on whether the saturated amplitude is larger than $\pi/2$. θ_{ss} is the mechanism to coarsen the pattern. In the linear regime, $c_1\theta$ and $c_2\theta_{ss}$ together determine a length scale $\sqrt{c_2/c_1}$ that characterizes how steep the transition from the mountain value to the valley value of θ. However, they predict the shortest wavelength (wave number $k = 0$) at which θ diverges. To capture the correct wavelength at the onset of instability, we need the third term c_3u, which is effectively the double integral of θ, and $2\pi(c_2/c_3)^{1/4}$ sets the wavelength. The coefficient $f(\theta_s)$ is to break the symmetry (s to $-s$) of the "phase separation" pattern so that the fingers can be fat or thin, and we will discuss the choice of $f(\theta_s)$ later.

After rescaling $\tau = c_1t$, $\sigma = s/L \in [0, 1]$, and $v = u/L^2$. Eq. (5.1) can be written in the dimensionless form as

$$\begin{aligned} \frac{\partial\theta}{\partial\tau} &= \left(\theta - \frac{\theta^3}{\theta_{max}^3}\right) + [\epsilon^2 + f(\theta_\sigma)]\theta_{\sigma\sigma} + (2\pi n)^4\epsilon^2 v, \\ v_{\sigma\sigma} &= \theta, \end{aligned} \tag{5.2}$$

where $\epsilon = \sqrt{c_2/c_1}$ (c_1 and c_2 are the coefficients in Eq. (5.1)), and n is the number of fingers in the domain. The simplest form of $f(\theta_\sigma)$ is

$$f(\theta_\sigma) = \begin{cases} (\pm)\epsilon_1^2 & \text{if} \quad \theta_\sigma > 0 \\ (\mp)\epsilon_1^2 & \text{if} \quad \theta_\sigma < 0 \end{cases}, \tag{5.3}$$

which allows us to independently control the widths of fingers $\sim (\epsilon^2 \pm \epsilon_1^2)^{1/2}$. The $\pm$ sign relies on the experimental fact whether the finger protruding upward is fatter or thinner. As Eq. (5.2) is anonymous in σ, it is translationally invariant when the periodic boundary condition is used.

As fingers grow, the contour length increases. To determine L, we use the experimental fact that the spacing of the fingers does not change as they grow, namely the

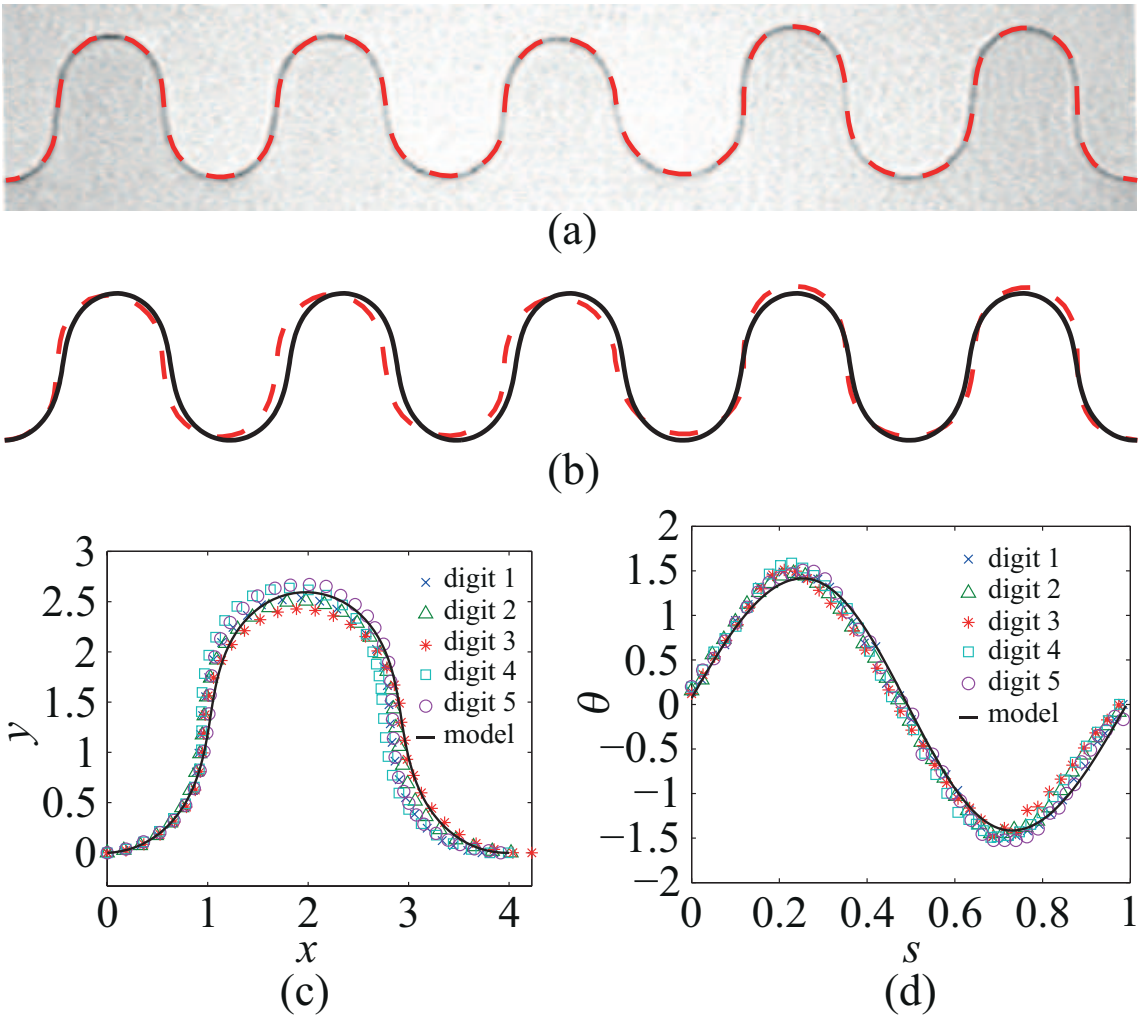

Figure 5.2: (a) The experimental image is taken from FIG. 2(a) in Ref. [5] and the red dashed curve is the trace of the interfacial crack. (b) The red dashed curve is the trace of the interfacial crack from the experimental image in (a), and the black curve is the numerical result from the model (parameters are chose to generate 5 fingers: $\theta_{max} = 1.022\pi$, $\epsilon = 0.022$ and $n = 5$ in Eq. (5.2), and $f(\theta_s) = (6.222 \times 10^{-3})^2$ if $\theta_s > 0$, $f(\theta_s) = -(6.222 \times 10^{-3})^2$ if $\theta_s < 0$ and $f(\theta_s) = 0$ if $\theta_s = 0$). (c) 5 digits ($1 \to 5$: left $\to$ right) from (a) are overlapped together with the single (periodic) digit numerically determined from the theoretical model. The x and y dimensions have been scaled by the film thickness. From Maha's paper, the wave length is roughly 4 times of the thickness. Therefore, we have taken 4 as the periodicity of the digits. (d) This plot shows comparison of the tangent angle $\theta(s)$ of a single digit between the experiments and numerical result determined by the model. $s \in [0, 1]$ is the scaled arclength coordinate.

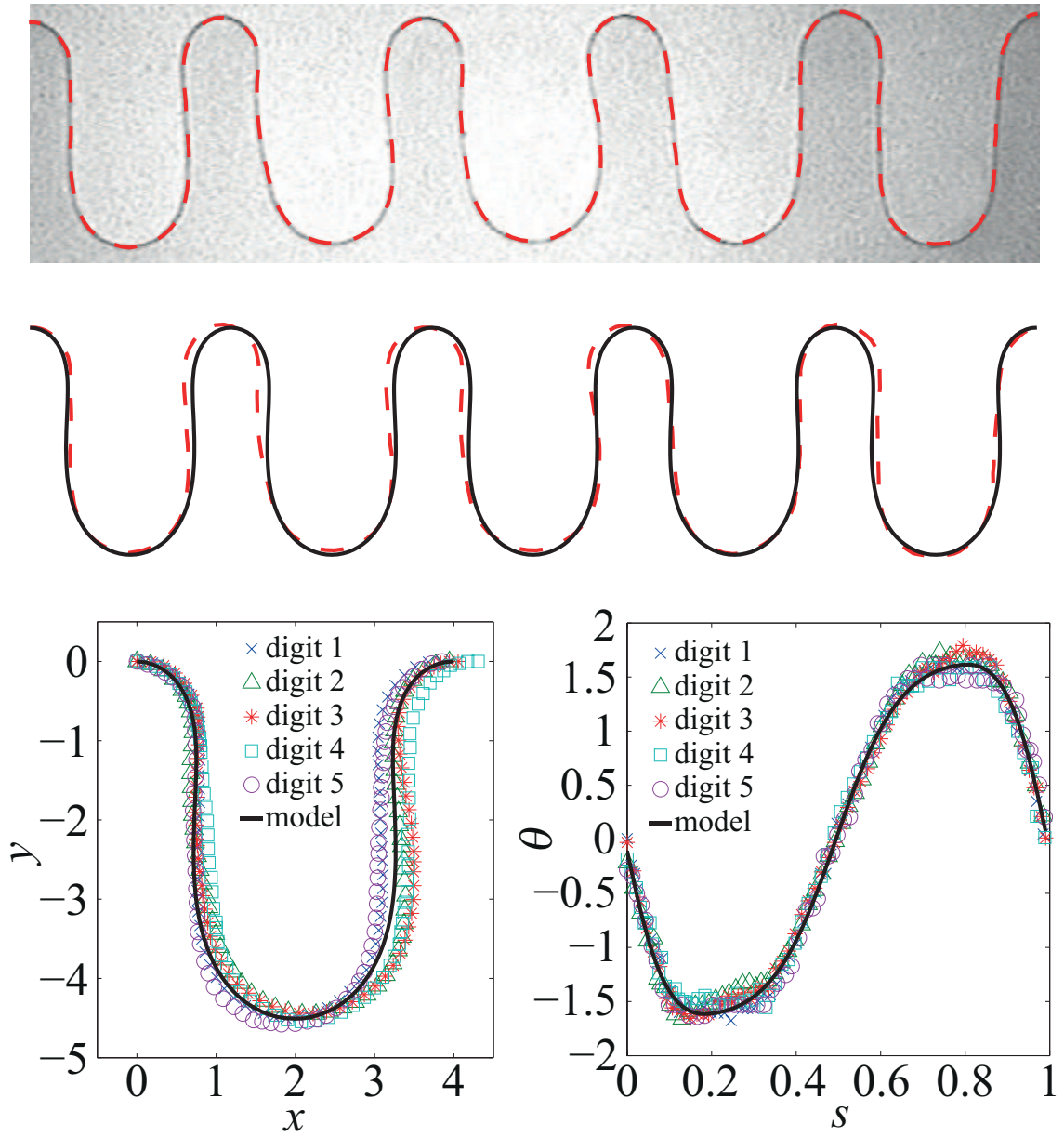

Figure 5.3: (a) The experimental image is taken from FIG. 2(c) in Ref. [5] and the red dashed curve is the trace of the interfacial crack. (b) The red dashed curve is the trace of the interfacial crack from the experimental image in (a), and the black curve is the numerical result from the model (parameters are chose to generate 5 fingers: $\theta_{max} = 0.5122\pi$, $\epsilon = 0.016$ and $n = 5$ in Eq.((5.2)), and $f(\theta_s) = 0.0101^2$ if $\theta_s > 0$, $f(\theta_s) = -0.0101^2$ if $\theta_s < 0$ and $f(\theta_s) = 0$ if $\theta_s = 0$) . (c) 5 digits ($1 \to 5$: left $\to$ right) from (a) are overlapped together with the single (periodic) digit numerically determined from the theoretical model. The x and y dimensions have been scaled by the film thickness. From Maha's paper, the wave length is roughly 4 times of the thickness. Therefore, we have taken 4 as the periodicity of the digits. (d) This plot shows comparison of the tangent angle $\theta(s)$ of a single digit between the experiments and numerical result determined by the model. $s \in [0, 1]$ is the scaled arclength coordinate.

constraint

$$L\int_0^1 cos\theta d\sigma = L_0, \tag{5.4}$$

where L_0 is the initial length of the straight crack front, and is scaled by the thickness of the thin film h. For example, in Fig. 5.2(a), there presents 5 fingers. To do the numerical computation for the same system, we set $n = 5$ in Eq. (5.2) and $L_0 = 20$ in Eq. (5.4) as $\lambda = 4$.

With the periodic boundary condition and random perturbations on $\theta = 0$ as the initial condition, the steady-state solution of Eqs. (5.2)-(5.4) reproduces the profile of a crack front. There are 3 fitting parameters in this model, which are ϵ, ϵ_1 and θ_{max}. These parameters are determined from an optimization setting. We start from initial guesses of the parameters, and adopt the covariance matrix adaptation method [81, 82] to converge to an optimal set of solutions that minimizes the square error between the computed profile and the experimental result. Fig. 5.2(a) shows the experimental picture of the crack front taken from [5], and the red curve traces the front. Fig. 5.2(b) shows the comparison of the crack front profile from the experiment (the red dashed curve) and the numerical solution (the black solid curve). As the solution of Eqs. (5.2) is periodic, we take out a single finger from the numerical result, and compare with the 5 fingers from the experiment, as shown in Fig. 5.2(c). All the quantitative features including the amplitude, the width, and the spacing of the fingers are all well captured. The comparison of θ is shown in Fig. 5.2(d), and the numerical solution agrees remarkably well with the experiment. Fig. 5.3 is another example to show that with 3 fitting parameters, the model is able to quantitatively reproduce a class of the crack fronts observed in experiments although their actual shapes may differ quite a bit.

Our model Eq. 5.2 resembles the classic Allen-Cahn equation [83, 84], but distinguishes from it on two major aspects: $c_3 v$ that is responsible for arresting the phase

separation from coarsening indefinitely, and $f(\theta_\sigma)$ that is responsible for breaking the mirror symmetry of the steady-state solution.

5.2 Numerical studies on cohesive instabilities

Soft polymeric adhesives are most effective when used as a thin layer to glue relatively rigid bodies. When the bodies are pulled apart, we see a cohesive instability manifest as spatially periodic digits that invade the elastic layer along its free meniscus. This instability is qualitatively different from the crack-like adhesive undulatory instabilities seen at the glass-gel contact line when adhesion starts to fail [5] (Chapter 5 Sec. 5.1): in this case adhesion is perfectly maintained and fingers appear along the elastic meniscus, just as in the case of viscous fingering [50], although there fingering is dynamic and out of equilibrium.

We have studied the form and nature of the elastic fingering instability in a confined thin film meniscus in a minimal rectilinear setting using a combination of theory, experiment and numerical simulation [8]. We show the origin of the transition is geometric (and hence likely to be ubiquitous), predict and verify the wavelength and threshold of the instability and show the transition is sudden with a region of bi-stability between the fingered and flat states and hence can encode digital information. To complete the story of this chapter, here I only include my numerical contribution to this work. For details in theory and experiments, please see Ref. [8].

Geometrically, our setup, sketched in Fig. 5.4, consists of a thin highly-elastic layer occupying the region $-a/2 < z < a/2$, $-\infty < x < \infty$, $0 < y < l$ with $a/l << 1$ that is adhered to rigid plates at $z = \pm a/2$. Experimentally we used a layer of polyacrylamide gel with a shear modulus of 550Pa, thickness $a \in [0.28, 10.64]$mm and width $l \in [50, 60]$mm

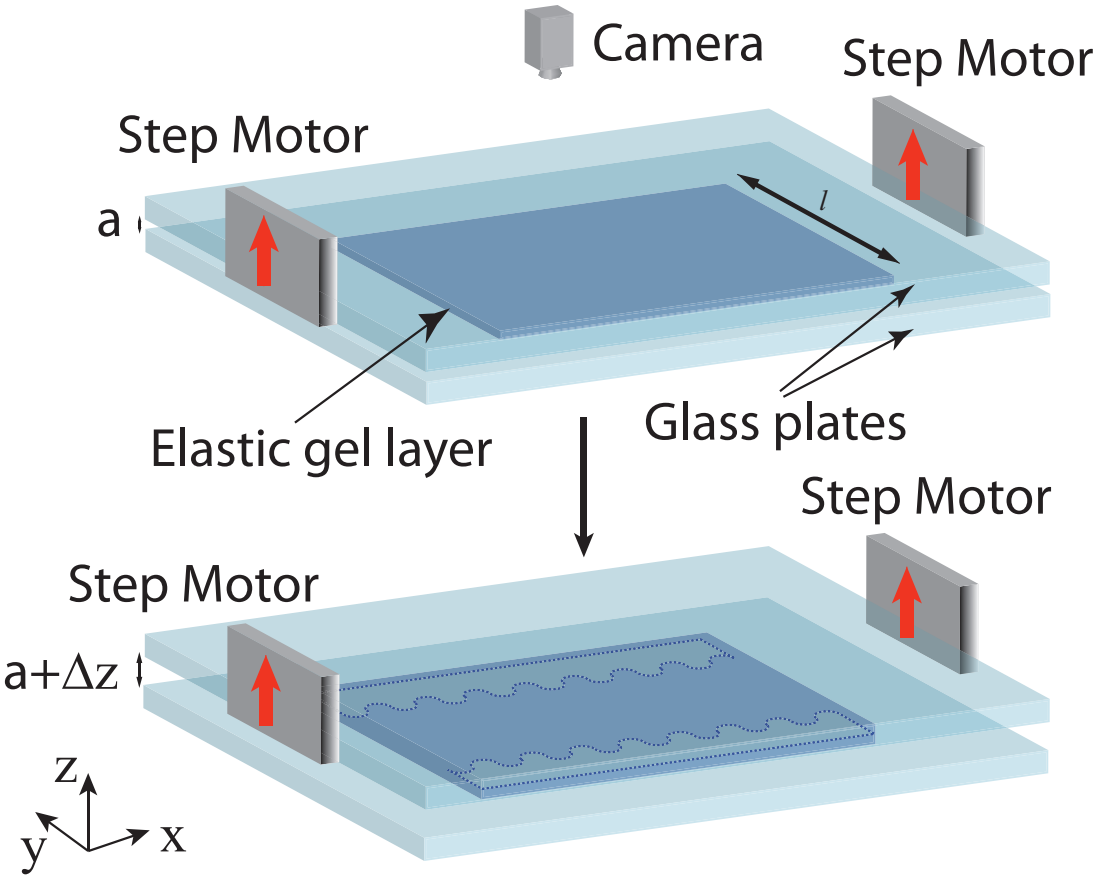

Figure 5.4: Schematic of an elastic layer between two rigid plates. Pulling the plates apart causes fingering.

bound between 10mm thick glass plates that were about 200mm long. The plates are then pulled apart, increasing their separation to $a + \Delta z$, while maintaining adhesion. Experimentally, the separation was increased at a constant speed of $2\text{mm}s^{-1}$. As the rigid plates are separated, the free boundaries of the elastomer (at $y = 0$ and $y = l$) retreat to form an elastic meniscus that, at a critical separation, loses stability via a sharp transition to an undulatory configuration in which fingers of air protrude into the elastomer, shown schematically in Fig. 5.4.

Fig. 5.5(a) shows the undulatory pattern observed. We note that Fig. 5.5(a) also shows a loading-unloading hysteresis loop for the transition, showing that the instability sets in suddenly past a given threshold in displacement via a subcritical instability, leading to large amplitude "digits" or fingers whose amplitude grows further upon further loading. On unloading, the fingers snap back at a much lower value of the displacement, suggestive of the strongly hysteretic nature of this first order transition. We find that the undulatory transition is fully reversible, unlike its hydrodynamic counterpart, and has no dependence on the shear modulus of the elastomer, strongly suggesting that the phenomenon is purely elastic. Numerical simulations of the instability carried out using a commercial finite element package ABAQUS 6.11 allow us to reproduce this instability; in Fig. 5.4(b), we show that both the form of the fingers and the hysteresis loop associated with a loading-unloading loop arise in a purely elastic quasi-static finite-element simulation.

Here is how the simulation is done. A sketch of the simulation domain is shown in Fig. 5.7. Although the transition under examination is purely elastic, its subcritical nature means that it cannot be simulated using equilibrium methods, so instead we use Newtonian dynamics with both numerical and viscous damping. We run two types of simulations: lower resolutions simulations containing many wavelengths to capture the behavior at onset and high resolution simulations containing a single wavelength to capture the profile of the

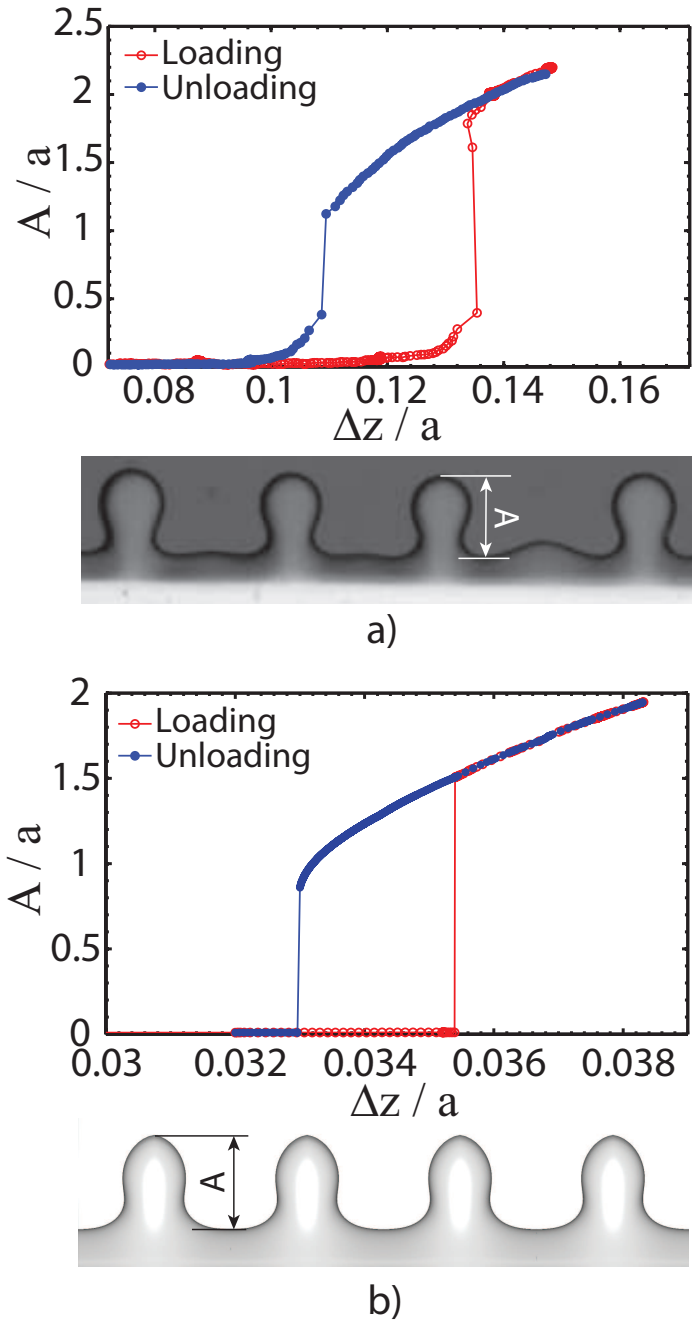

Figure 5.5: Figures (a) and (b) are hysteresis loops showing the amplitude of the fingers as a function of plate separation Δz, and top-views of a fingered boundary showing the fingers of air (bottom) invading the elastic layer (top). Figure b shows experimental data for a layer of thickness $a = 3.05$mm and width $l = 56$mm while figure (b) shows finite element results (calculated using a single periodically repeated finger) for an elastic layer for thickness $a = 1$mm and width $l = 40$mm.

Figure 5.6: $3D$ geometry of a single finger right after the instability. Only one finger was simulated and periodically repeated for display purpose. Adobe reader is recommended to open this file in order to play with the interactive figure.

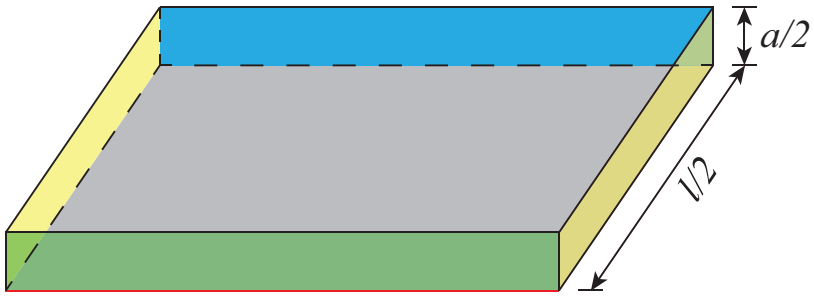

Figure 5.7: Sketch of the simulation domain. Only a quarter of the thin slab is simulated. To detect whether the front surface (green) is oscillatory, we extract the displacement at the intersection line (red) where the middle plan (light grey) and front surface meet.

fingers.

1. Material properties

   The gel is modeled as an incompressible neo Hookean material with shear modulus being $500Pa$. The density of the material is $10^3\text{Kg}/m^3$. Rayleigh damping is applied to ensure that the system is overdamped. For a given mode i the fraction of critical damping, ξ_i, can be expressed in terms of the damping factors α_R and β_R as:

   $$\xi_i = \frac{\alpha_R}{2\omega_i} + \frac{\beta_R \omega_i}{2}, \tag{5.5}$$

   where ω_i is the natural frequency at this mode, α_R is for mass proportional damping and β_R is for stiffness proportional damping. To define Rayleigh damping, we need to specify α_R and β_R. We load the boundary near the critical displacement and perform a linear perturbation procedure to extract ω_i, $i = 1$ to 5, and correspondingly specify α_R to make ξ_i around 5. This is only a crude estimation of the damping coefficient as the stiffness matrix is a function of strain. When the fingers are fully grown, we expect the natural frequency is different from that of the onset state. After a try and error, we set $\alpha_R = 8000$ to 10000 to damp out the lowest frequency oscillation. For the highest frequency, we rely on numerical damping (which will be documented later) and set $\beta_R = 0$.

2. Boundary conditions

   Symmetric boundary conditions are applied on the two lateral planes (highlighted in yellow), the middle plane (light grey), and the back plane (blue). Therefore only a quarter of the physical thin slab is simulated to save computational power. The front surface (green) is stress free and Gaussian white noise is applied on its initial y coordinate in order to trigger the instability at the critical loading displacement. The mean magnitude of the noise is 2% of the smallest mesh size inside the system. The top surface is pulled apart at such a small constant velocity that it always takes 5 to 10 minutes before the top surface is loaded up to the critical displacement. Once oscillations of the front surface ore detected., the pulling is stopped and the top surface is held still while the system evolves freely.

3. Meshes and elements

   First, to get the displacement and wavelength of the onset of the instability, we run the simulation in a long cell (which contains 8 to 9 wavelengths) containing 401 nodes for the length, 76 nodes for the half-width and 26 nodes for the half-gap. This is more than adequate to detect the point of onset and the wavelength of the unstable mode, but, as the fingers grow, the strain at the tip of the fingers becomes very large (greater than 7) so we need a finer mesh. In order to capture the profile of the fully grown finger, we set the length of gel slab as half the previously calculated wavelength, and keep the boundary conditions the same. We are now able to devote $201 \times 76 \times 26$ nodes to a quarter of a single finger, which is sufficient to resolve its full profile, even with the very large strains at its tip. Mesh density is geometrically biased towards the free front and middle plane, where the nonlinearity is the most pronounced after instability happens. C3D8H (8-node linear brick, hybrid with constant pressure) elements are

adopted. The pressure penalty serves as an additional degree of freedom to ensure the constraint of incompressibility.

4. Time integrator

   As the material is incompressible, it is impossible to simulate the dynamic response with an explicit method as the stable time increment would be inversely proportional to the bulk modulus. Therefore we use an implicit method. Both the Hilber-Hughes-Taylor (HHT) integrator and backward Euler integrator are tried and compared and they both get the same onset of instability and fastest growing mode. In our system, we do not care about the accurate resolution of high-frequency vibrations, so considerable numerical dissipation is applied to reduce the solution noise and obtain convergence during certain stages of the loading history. In the HHT operator, we choose $\alpha = -1/3$, $\beta = 1/4(1-\alpha)^2$ and $\gamma = 1/2-\alpha$ to achieve the maximum numerical damping [85]. Adaptive time step is used. Time step decreases dramatically in the neighborhood of instability. Tolerance control is as default in ABAQUS.

5. Dimensions of the samples

   We choose layer dimensions that ensure that the ratio of the width to the gap thickness is large (over 10) so that the layer can reasonably be thought of as thin. Our choice of length is a trade-off between the slab containing many wavelengths and the required computational power being reasonable. We choose lengths that are 8 to 9 wavelengths. We note that this causes some end-effects in our simulation, which explains why our simulated wavelength is slightly below our experimentally observed wavelength. Tab. 5.1 shows the sample dimensions on which we have done simulations. Fig. 5.6 is the $3D$ geometry of the fully grown finger right after the instability onset. Only one finger was simulated and periodically repeated for display purpose.

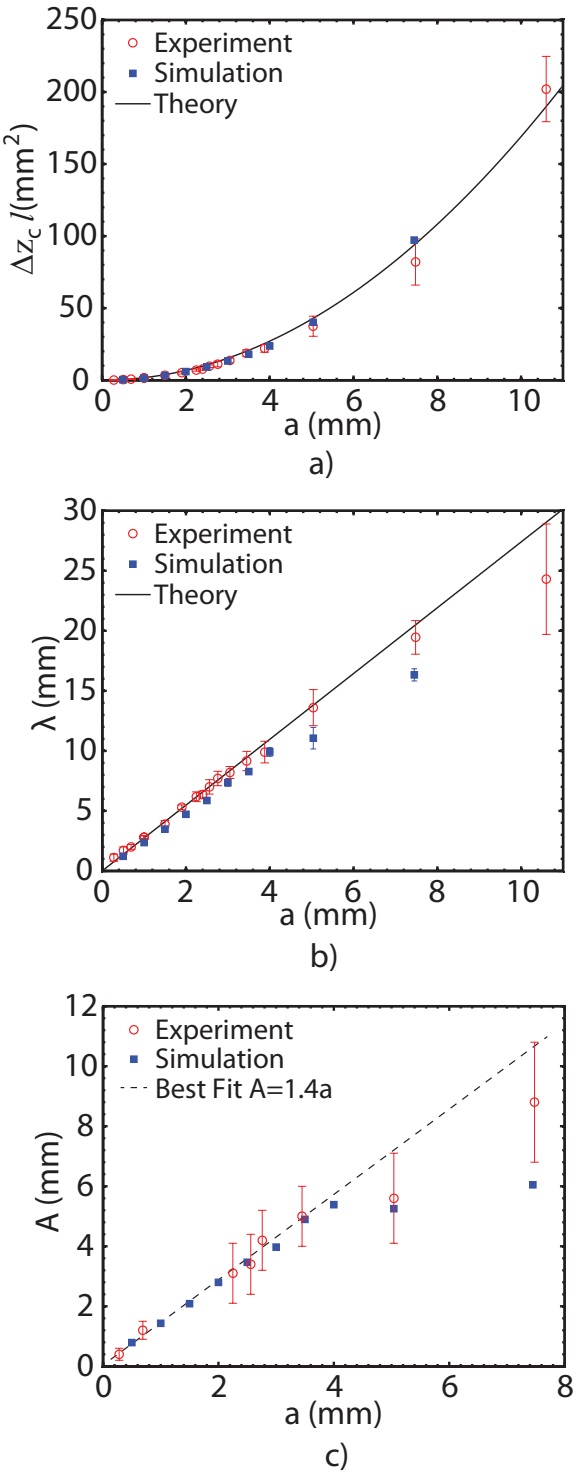

Figure 5.8: Experimental and numerical confirmation of the theoretical predictions. a) Wavelength λ at instability as a function of thickness a. b) Threshold separation Δz_c times width l as a function of thickness a. c) Finger amplitude A just after threshold as a function of thickness a.

Table 5.1: Sample Dimensions (mm)

length	10	20	30	40	50	60	70	80	100.2	149
width	40	40	40	40	60	60	80	80	58.5	55.8
gap thickness	0.5	1.0	1.5	2.0	2.5	3.0	3.5	4.0	5.04	7.45

In Fig. 5.8, we show a comparison of the wavelength and the threshold displacement from finite-element simulations with experiments carried out over a range of elastomer thicknesses as well as the theoretical predications (the wavelength $\lambda \approx 2.74a$ and the critical pulling displacement is $\Delta z \approx 1.69a^2/l$); the results compare very well. Although the linearized analysis cannot extend beyond the point of instability, the finite element simulations have no such limit. These show that the finite amplitude of the fingers just after the instability is approximately $1.4a$, which is a good agreement with the experiments, and confirm the subcritical nature of the instability with a region of bistability wherein the homogeneous and undulatory phases of the interface co-exist.

For a radial geometry, it was shown experimentally that if fluid is pumped into a cavity in the solid layer the cavity first dilates until, at some pressure, finger like protrusions of fluid invade the elastic layer[7], as seen in Fig. 5.9(c). The adhesion between the solid layer and the bounding plates is also perfectly maintained as the fingers form. The schematic picture of the experimental setup is shown in Fig. 5.9(a)(b). We have been developing a theory [86] to understand this phenomenon. This theory also makes a concrete connection between two different sorts of elastic fingering: fingering of an elastic layer in tension [6, 8] and fingering of an elastic layer being invaded by a fluid [7]. This means that there is a first order equivalency between the critical pulling displacement of the bounding plate and the critical fluid pressure acting in the cavity in terms of generating fingers. The finite element simulation to backup the analytic predictions on the onset of instability and the primary mode is an ongoing work. The full simulation is able to capture the subcritical nature of

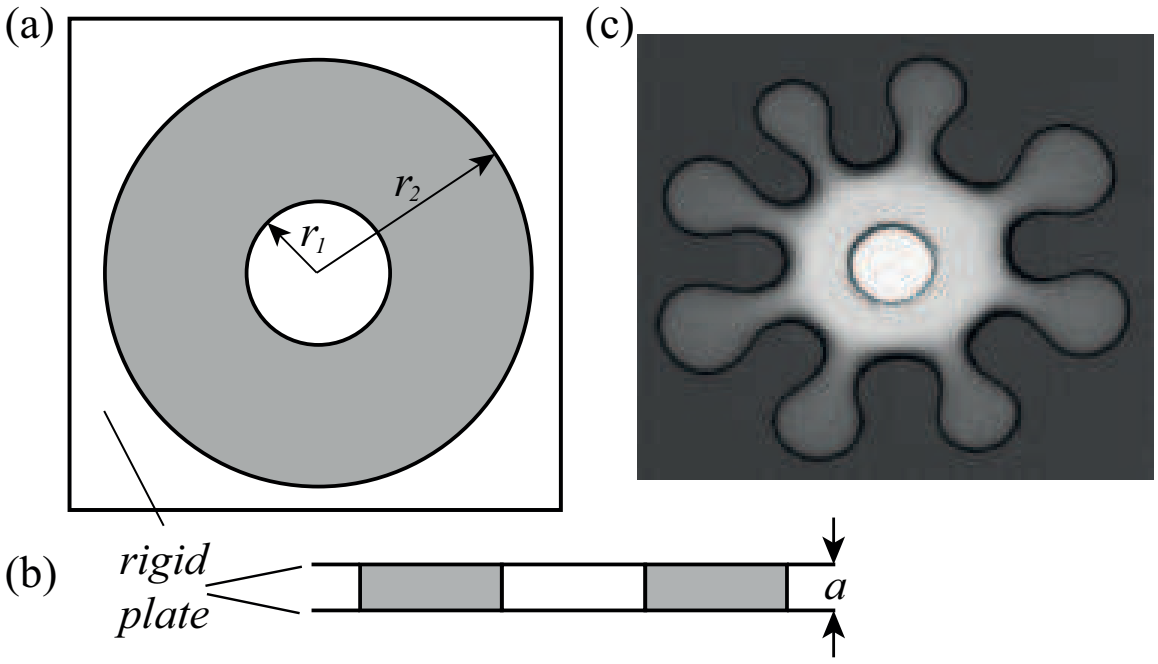

Figure 5.9: (a) Top-view of the experiment: two rigid plates confine a thin elastic layer with a central cavity containing fluid. (b) Side view showing the thickness of the elastic layer. c) Experimentally obtained fingering pattern from [7].

the finger formation and the amplitude of the fingers, where the linear theory fails to have any predicative power. Fig. 5.10 shows two examples of the deformed solid layer right after the fingering instability happens.

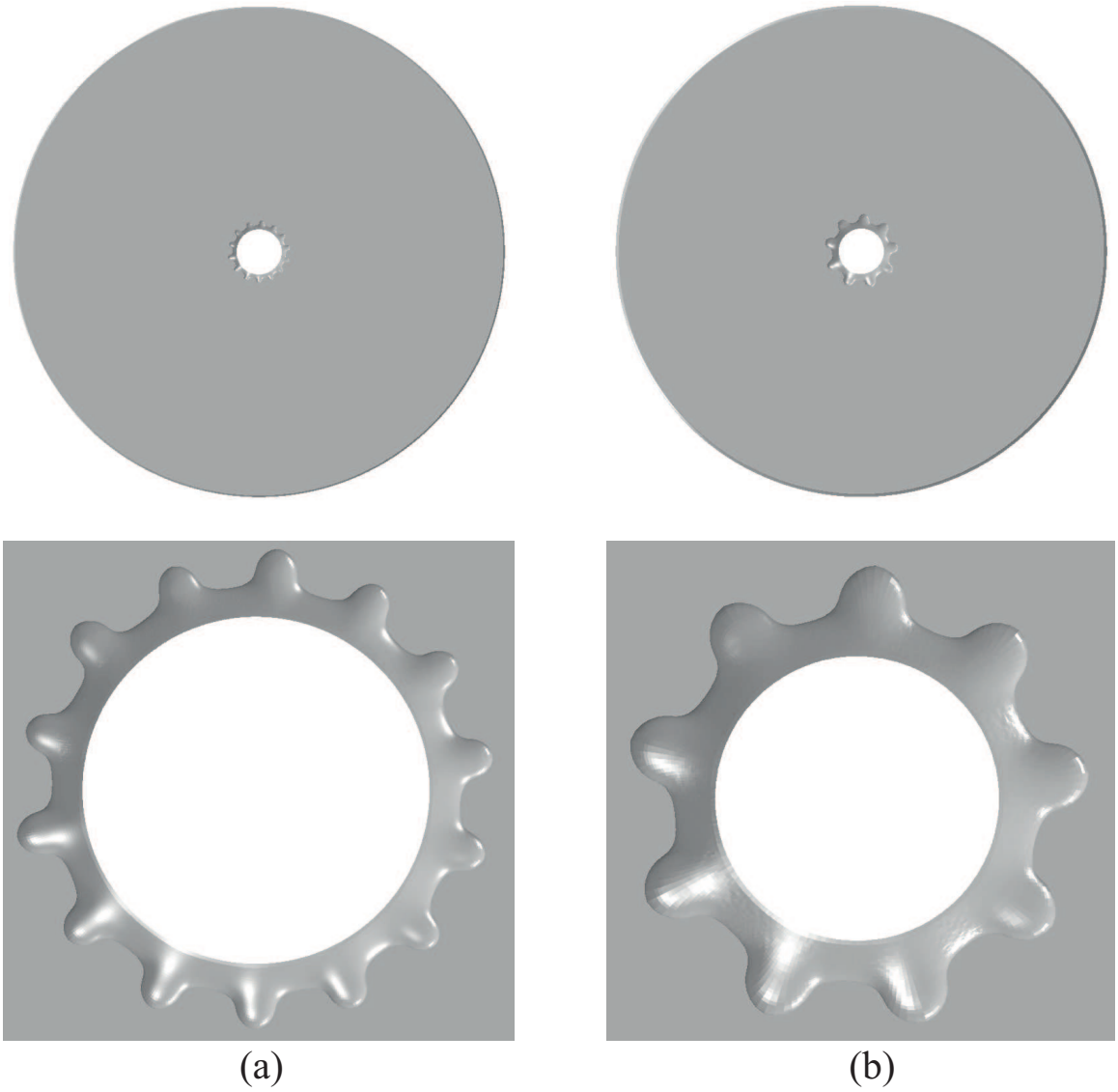

Figure 5.10: A thin circular elastic layer with thickness a and radius $r_2 = 125$mm has a central cavity of radius $r_1 = 11.5$mm (see Fig. 5.9(a) for r_1 and r_2) pressurized by a fluid. This figure shows two examples of the deformed solid layer right after the instability happens. Half of the solid layer cut through the central plan is shown. The top row is the whole domain and the bottom row is the zoomed-in picture of finger-like protrusions. (a) $a = 2.5$mm. (b) $a = 4$mm.

Chapter 6

Conclusions

We have used a combination of theories and numerical simulations to study some problems in discrete and continuum mechanics. A particular effort has been made to construct continuum theories that describe the responses of discrete mechanical systems, in the spirit of condensing information by mathematical abstraction.

In Chapter 2, We have characterized the geometry of the simplest of periodic pleated structures, Miura-ori, by a pair of design angles α and θ together with the constraint of piecewise isometric deformations. We have expressed the linearized planar stretching rigidities and non-planar bending rigidities in terms of the design angles. We have shown that the bending response of a Miura plate made of these collective unit cells can be described in terms of that of a one-dimensional beam, because the responses in the two principle directions are coupled through the design angles. We have found that the negative in-plane Poisson's ratio ν_{wl} and the positive out-of-plane bending Poisson ratio ν_b satisfies the general relation $\nu_{wl} = -\nu_b$, a consequence of geometry alone. We have also posed and solved a series of design problems to find the optimal geometric parameters of the unit cell that lead to extrema of stretching and bending rigidities as well as contraction/expansion

ratios of the system. This raises the possibility of optimal control of actuated origami-based materials in soft robotics and elsewhere using the simple geometrical mechanics approaches that we have introduced here.

In Chapter 3, we have studied the dynamics of bundle formation driven by drying liquid for two characteristic problems in two and three dimensions. For the case of two-dimensional array of lamellae, we have proposed a discrete model that explicitly considers all relevant forces and torques. Based on these results, the linear stability analysis has captured the primary 2-plate-collapse eigenmode. Full numerical simulations have shown that the final states sensitively depends on initial perturbations because of the jump in the location of the contact line when the contact angle reaches a critical value. This leads to an effective stiffness that suddenly decreases. Therefore, self-organization of clusters cannot be predicted by energy minimization arguments but depend on the dynamics of the drying process - this is especially true when the coupling of geometry to local evaporation rates is taken into account. For the three-dimensional bristle case, our numerical method has captured the primary fourfold eigenmode associated with the onset of collapse. Once again, the full dynamics has predicted the final stable state, which is determined by the competition between capillarity and elasticity. For both cases, our numerical results have agreed well with many of the salient experimental observations. In particular, we can explain the eigenmodes at the onset of instability and the time scales on which clusters form, give dynamical predictions of both regular and irregular hierarchical bundle formations, and capture the final state.

In Chapter 4, we have proposed a one-dimensional continuum theory to describe the dynamics of elastocapillary coalescence of an array of lamellae immersed in an evaporating liquid. The continuum model has been derived from the a discrete microscopic counterpart of the process presented in Chapter 3. Therefore, all the parameters in this

model can be explicitly linked to microscopic measurable material and geometric parameters. Our model predicts the onset and the arising length scale of the primary unstable mode in the linear regime, consistent with experiments. In the nonlinear regime, it further captures the coalescence of pillars, their elastic arrest and the eventual separation of bundles as the liquid dries out. The model looks similar to the classical Cahn-Hilliard form but distinguishes from it by the elastic contribution. It is this term that provides a simple refining mechanism for the phase separation. The two competing actions - coarsening driven by surface tension and refining driven by elastic resistance determine the stability of the system and arrests the coarsening at an equilibrium size. This idea can be and has been generalized to understand the aggregation dynamics with arrested phase separation that has been observed in a variety of physical and biological systems.

In Chapter 5, we have studied two forms of elastic fingering instabilities that occur in the thin confined elastic films. We have revisited the problem of adhesive instability that arises from peeling a flexible elastic plate off a soft thin confined adhesive film, where the adhesive failure occurs via the loss of adhesion at one of the surfaces attached to the adhesive, and an undulating crack front can appear and evolve into a 2D rippling pattern. We have constructed a simple model completely based on the geometry and symmetry considerations. This model is not meant as a fully realistic alternative to the actual evolution equations which will correctly reproduce all the intricacies of the long-time development of the system. However the model is minimal in mathematics, and greatly condenses information in the sense that it may be able to describe a class of moving interfaces that are not even driven by the same physics. The 3 fitting parameters in this model are chosen by an optimization setting. The model is able to capture the important length scales that arise in the crack front, including the wavelength at the onset of instability, the finger amplitude and widths of fat and thin fingers. We have shown the profiles of the crack fronts obtained from

numerical solutions of the model, and compared with the experimental results. They are in a remarkable quantitative agreement. We have also studied the cohesive instability when the thin confined elastic films is loaded under tension. The cohesive failure manifests as spatially periodic digits that invade the elastic layer along its free meniscus even though the perfect adhesion is maintained. This mode of failure has been largely overlooked experimentally and understood theoretically only until recently by our work. My numerical contributions to this work has been presented. We have shown a comparison of the wavelength and the threshold displacement from finite-element simulations with experiments carried out over a range of elastomer thicknesses as well as the theoretical predications. We have shown that the finite amplitude of the fingers just after the instability scales linearly with the film thickness, which is a good agreement with the experiments, and confirm the subcritical nature of the instability. I have also shown some preliminary results of an ongoing work that provides a theoretical understanding of the cohesive fingering instability when a fluid is injected into a cavity in the thin elastic film in an experimental setup with a radial geometry.

Bibliography

[1] K. Miura. Proceedings of 31st congress international astronautical federation. Tokyo, 1980. IAF-80-A 31:1-10.

[2] T. Tanaka, M. Morigami, and N. Atoda. Mechanism of resist pattern collapse during development process. *Jpn. J. Appl. Phys.*, **32**:6059–6059, 1993.

[3] J. Bico, B. Roman, L. Moulin, and A. Boudaoud. Elastocapillary coalescence in wet hair. *Nature*, **432**:690, 2004.

[4] B. Pokroy, S. H. Kang, L. Mahadevan, and J. Aizenberg. Self-organization of a mesoscale bristle into ordered, hierarchical helical assemblies. *Science*, **323**:237–240, 2009.

[5] Animangsu Ghatak, Manoj K. Chaudhury, Vijay Shenoy, and Ashutosh Sharma. Meniscus instability in a thin elastic film. *Phys. Rev. Lett.*, 85:4329–4332, 2000.

[6] Kenneth R. Shull, Cynthia M. Flanigan, and Alfred J. Crosby. Fingering instabilities of confined elastic layers in tension. *Phys. Rev. Lett.*, 84:3057–3060, 2000.

[7] B. Saintyves, O. Dauchot, and E. Bouchaud. Bulk elastic fingering instability in hele-shaw cells. *Phys. Rev. Lett.*, 111:047801, 2013.

[8] J.S. Biggins, B. Saintyves, Z. Wei, E. Bouchard, and L. Mahadevan. Digital instability of a confined elastic meniscus. *Proc. Natl. Acad. Sci. USA*, **110**:12545–12548, 2013.

[9] D. R. Smith, J. B. Pendry, and M. C. Wiltshire. Metamaterials and negative refractive index. *Science*, **305**:788–792, 2004.

[10] G. N. Greaves, A. L. Greer, R. S. Lakes, and T. Rouxel. Poisson's ratio and modern materials. *Nat. Mater.*, **10**:823–837, 2011.

[11] Wm. T. M. Forbes. How a beetle folds its wings. *Psyche*, **31**:254–258, 1924.

[12] H. Kobayashi, B. Kresling, and J. F.V. Vincent. The geometry of unfolding tree leaves. *Proc. R. Soc. B*, **265**:147–154, 1998.

[13] H. Kobayashi, M. Daimaruya, and H. Fujita. Unfolding of morning glory flower as a deployable structure. *Solid Mech. Its Appl.*, **106**:207–216, 2003.

[14] E. A. Elsayed and B. B. Basily. A continuous folding process for sheet materials. *Int. J. Mater. Prod. Technol.*, **21**:217–238, 2004.

[15] R. S. Lakes. Foam structures with a negative poisson's ratio. *Science*, **235**:1038–1040, 1987.

[16] B. D. Caddock and K. E. Evans. Microporous materials with negative poisson's ratios. i. microstructure and mechanical properties. *J. Phys. D*, **22**:1877, 1989.

[17] K. E. Evans and B. D. Caddock. Microporous materials with negative poisson's ratios. ii. mechanisms and interpretation. *J. Phys. D*, **22**:1883, 1989.

[18] A.Y. Haeri, D. J. Weidner, and J. B. Parise. Elasticity of -cristobalite: A silicon dioxide with a negative poisson's ratio. *Science*, **257**:650–652, 1992.

[19] A. L. Goodwin, D. A. Keen, and G. Tucker. Large negative linear compressibility of $Ag_3[Co(CN)_6]$. *Proc. Natl. Acad. Sci. U.S.A.*, **105**:18708–18713, 2008.

[20] J. Hutchinson K. E. Evans, M. A. Nkansah and S. C. Rogers. Molecular network design. *Nature*, **353**:124, 1991.

[21] R. Lang. *Origami Design Secrets: Mathematical Methods for an Ancient Art.* A K Peters/CRC Press, Boca Raton, FL, 2nd edition, 2011.

[22] E. Demaine and J. ORourke. *Geometric Folding Algorithms: Linkages, Origami, Polyhedra.* Cambridge University Press, Cambridge, England, 2007.

[23] T. Hull. *Project Origami: Activities for Exploring Mathematics.* A K Peters/CRC Press, Boca Raton, FL, 2011.

[24] Y. Klettand and K. Drechsler. *Origami5: International Meeting of Origami, Science, Mathematics, and Education.* CRC Press, Boca Raton, FL, 2011. Edited by P. Wang-Iverson, R. J. Lang and M. Yim.

[25] M. Schenk and S. Guest. *Origami5: International Meeting of Origami, Science, Mathematics, and Education.* CRC Press, Boca Raton, FL, 2011. Edited by P. Wang-Iverson, R. J. Lang and M. Yim.

[26] Alessandro Papa and Sergio Pellegrino. Systematically creased thin-film membrane structures. *J. Spacecr. Rockets*, **45**:10–18, 2008.

[27] N. Bowden, S. Brittain, A. G. Evans, J.W. Hutchinson, and G. M. Whitesides. Spontaneous formation of ordered structures in thin films of metals supported on an elastomeric polymer. *Nature*, **393**:146, 1998.

[28] L. Mahadevan and S. Rica. Self-organized origami. *Science*, **307**:1740, 2005.

[29] B. Audoly and A. Boudaoud. Buckling of a stiff film bound to a compliant substrate – part iii: Herringbone solutions at large buckling parameter. *J. Mech. Phys. Solids*, **56**:2444–2458, 2008.

[30] G. M. Whitesides and B. Grzybowski. Self-assembly at all scales. *Science*, **295**:2418–2421, 2002.

[31] G. R. Desiraju. *Crystal Engineering: The Design of Organic Solids.* Elsevier, New York, 1989.

[32] N. Bowden, A. Terfort, J. Carbeck, and G.M. Whitesides. Assembly of mesoscale bojects into ordered two-dimensional arrays. *Science*, **276**:233–235, 1997.

[33] P. W. K. Rothemund. Using lateral capillary forces to compute by selfassembly. *Proc. Natl. Acad. Sci. U.S.A*, **97**:984–989, 2000.

[34] D. Vella and L. Mahadevan. The 'cheerios effect'. *Am. J. Phys.*, **73**:817–825, 2005.

[35] A. K. Geim, S. V. Dubonos, I. V. Grigorieva, K. S. Novoselov, A. A. Zhukov, and S. Y. Shapoval. Microfabricated adhesive mimicking gecko foot-hair. *Nature Mater.*, **2**:461–463, 2003.

[36] K. K. S. Lau, J. Bico, K. B. K. Teo, M. Chhowalla, G. A. J. Amaratunga, W. I. Milne, G. H. McKinley, and K. K. Gleason. Superhydrophobic carbon nanotube forests. *Nano Lett.*, **3**:1701–1705, 2003.

[37] N. Chakrapani, B. Wei, A. Carrillo, P. M. Ajayan, and R. S. Kane. Capillaritydriven assembly of two-dimensional cellular carbon nanotube foams. *Proc. Natl. Acad. Sci. U.S.A*, **101**:4009–4012, 2004.

[38] H. Y. Kim and L. Mahadevan. Capilliary rise between elastic sheets. *J. Fluid Mech.*, **548**:141–150, 2006.

[39] C. Duprat, J. M. Aristoff, and H. A. Stone. Dynamics of elastocapillary rise. *J. Fluid Mech.*, **679**:641–654, 2011.

[40] M. Taroni and D. Vella. Multiple equlibria in a simple elastocapillary system. *J. Fluid Mech.*, **712**:273–294, 2012.

[41] D. Chandra, S. Yang, A. A. Soshinsky, and R. J. Gambogi. Biomimetic ultrathin whitening by capillary-force-induced random clustering of hydrogel micropillar arrays. *ACS Appl. Mater. Interfaces*, **1**:1698–1704, 2009.

[42] Y. P. Zhao and J. G. Fan. Clusters of bundled nanorods in nanocarpet effect. *Appl. Phys. Lett.*, **88**:103123, 2006.

[43] A. D. Gat and M. Gharib. Elasto-capilliary coalescence of multiple parallel sheets. *J. Fluid Mech.*, **723**:692–705, 2013.

[44] B. Grzybowski, H.A. Stone, and G.M. Whitesides. Dynamic self-assembly of magnetized, millimeter-sized objects rotating at the liquid-air interface. *Nature*, **405**:1033–1036, 2000.

[45] B.A. Grzybowski, X. Jiang, H.A. Stone, and G.M. Whitesides. Dynamic, self-assembled aggregates of magnetized, millimeter-sized objects rotating at the liquid-air interface: Macroscopic, two-dimensional classical artificial atoms and molecules. *Phys. Rev. E*, **64**:11603, 2001.

[46] Arezki Boudaoud, José Bico, and Benoˆ Roman. Elastocapillary coalescence: Aggregation and fragmentation with a maximal size. *Phys. Rev. E*, 76:060102, 2007.

[47] Shull KR. Contact mechanics and the adhesion of soft solids. *Mater. Sci. Eng. Rep.*, **36**:1–45, 2002.

[48] W. Monch and S. Herminghaus. Elastic instability of rubber films between solid bodies. *Europhys. Lett.*, **53**:525–531, 2001.

[49] M. Adda Bedia and L. Mahadevan. Crack-front instability in a confined elastic film. *Proc. R. Soc. Lond. A*, **462**:3233–3251, 2006.

[50] Saffman PG and Taylor GI. The penetration of a fluid into a porous medium or hele-shaw cell containing a more viscous liquid. *Proc. R. Soc. Lond. A*, **245**:312–329, 1958.

[51] GM Homsy. Viscous fingering in porous media. *Annu. Rev. Fluid Mech.*, **19**:271–311, 1987.

[52] R. J. Fields and M. F. Ashby. Finger-like crack growth in solids and liquids. *Philos. Mag.*, **33**:33–48, 1976.

[53] E. Ventsel and T. Krauthammer. *Thin Plates and Shells: Theory, Analysis, and Applications*. CRC Press, Boca, Raton, FL, 1st edition, 2001.

[54] R. Bridson, S. Marino, and R. Fedkiw. ACM SIGGRAPH/Eurograph. Symp. Comp. Animation (SCA). pages 28–36, 2003.

[55] R. Burgoon, E. Grinspun, and Z. Wood. Proceedings of the ISCA 21st international conference on computers and their applications. page 180, 2006.

[56] W. J. Arora, A. J. Nichol, H. I. Smith, and G. Barbastathis. Membrane folding to achieve three-dimensional nanostructures: Nanopatterned silicon nitride folded with stressed chromium hinges. *Appl. Phys. Lett.*, **88**:053108, 2006.

[57] E. Hawkes, B. An, N. Benbernou, H. Tanaka, S. Kim, E. D. Demaine, D. Rus, and R. J. Wood. Programmable matter by folding. *Proc. Natl. Acad. Sci. U.S.A.*, **107**:12441–12445, 2010.

[58] Mark Schenk and Simon D. Guest. Geometry of miura-folded metamaterials. *Proc. Natl. Acad. Sci. U.S.A*, **110**:3276–3281, 2013.

[59] S. Neukirch, B. Roman, B. Gaudemaris, and J. Bico. Piercing a liquid surface with an elastic rod: Buckling under capillary forces. *J. Mech. Phys. Solids*, **55**:1212–1235, 2007.

[60] S. Timoshenko and J. M. Gere. *Mechanics of Materials*. Van Nostrand Reinhold Co., 1972.

[61] S. H. Kang, B. Pokroy, L. Mahadevan, and J. Aizenberg. Control of shape and size of nanopillar assembly by adhesion-mediated elastocapillary interaction. *ACS Nano*, **4**:6323–6331, 2010.

[62] Neil W. Ashcroft and N. David Mermin. *Solid State Physics*. Thomson Press (India) Ltd, 2003.

[63] J. W. Cahn and J. E. Hilliard. Free energy of a nonuniform system. i. interfacial free energy. *J. Chem. Phys.*, **28**:258–267, 1958.

[64] K Kern, H Niehus, A Schatz, P Zeppenfeld, J Goerge, and G Comsa. Long-range spatial self-organization in the adsorbate-induced restructuring of surfaces: Cu100-(2 x 1)O. *Phys. Rev. Lett.*, **67**:855–858, 1991.

[65] K. Pohl, M. C. Bartelt, J. de la Figuera, N. C. Bartelt, J. Hrbek, and R. Q. Hwang. Identifying the forces responsible for self-organization of nanostructures at crystal surfaces. *Nature*, **397**:238–241, 1999.

[66] Holger Röder, Rolf Schuster, Harald Brune, and Klaus Kern. Monolayer-confined mixing at the Ag-Pt(111) interface. *Phys. Rev. Lett.*, **71**:2086–2089, 1993.

[67] W. Lu and Z. Suo. Dynamics of nanoscale pattern formation of an epitaxial monolayer. *J. Mech. Phys. Solids*, **49**:19370–1950, 2001.

[68] J. Erlebacher, M. Aziz, A. Karma, N. Dimitrov, and K. Sieradzki. Evolution of nanoporosity in dealloying. *Nature*, **410**:450–453, 2001.

[69] J. S. Langer. Instabilities and pattern formation in crystal growth. *Rev. Mod. Phys.*, **52**:1–28, 1980.

[70] John W Hutchinson and Zhigang Suo. Mixed mode cracking in layered materials. *Advances in applied mechanics*, **29**:191, 1992.

[71] Z Suo, C-M Kuo, DM Barnett, and JR Willis. Fracture mechanics for piezoelectric ceramics. *Journal of the Mechanics and Physics of Solids*, **40**:739–765, 1992.

[72] G.F. Oster and G.M. Odell. The mechanochemistry of cytogels. *Physica D*, **12**:333 – 350, 1984.

[73] W. J. Boettinger, J. A. Warren, C. Beckermann, and A. Karma. Phase-field simulation of solidification1. *Annual Review of Materials Research*, **32**:163–194, 2002.

[74] Alain Karma, David A. Kessler, and Herbert Levine. Phase-field model of mode iii dynamic fracture. *Phys. Rev. Lett.*, **87**:045501, 2001.

[75] Vicent Hakim and Alain Karma. Laws of crack motion and phase-field models of fracture. *J. Mech. Phys. Solids*, **57**:342–368, 2009.

[76] R. Folch, J. Casademunt, A. Hernández-Machado, and L. Ramírez-Piscina. Phase-field model for hele-shaw flows with arbitrary viscosity contrast. ii. numerical study. *Phys. Rev. E*, **60**:1734–1740, 1999.

[77] Thierry Biben, Klaus Kassner, and Chaouqi Misbah. Phase-field approach to three-dimensional vesicle dynamics. *Phys. Rev. E*, **72**:041921, 2005.

[78] Richard C. Brower, David A. Kessler, Joel Koplik, and Herbert Levine. Geometrical models of interface evolution. *Phys. Rev. E*, **29**:1335–1342, 1984.

[79] Jennifer A. Hodgdon and James P. Sethna. Derivation of a general three-dimensional crack-propagation law: A generalization of the principle of local symmetry. *Phys. Rev. B*, **47**:4831–4840, 1993.

[80] Augustus Edward Hough Love. *A Treatise on the Mathematical Theory of Elasticity.* the University Press, 1906. pp. 385.

[81] N. Hansen and A. Ostermeier. Completely derandomized self-adaptation in evolution strategies. *Evolutionary Computation*, **9**:159–195, 2001.

[82] N. Hansen, S. D. Muller, and P. Koumoutsakos. Reducing the time complexity of the derandomized evolution strategy with covariance matrix adaptation (cma-es). *Evolutionary Computation*, **11**:1–18, 2003.

[83] S. M. Allen and J. W. Cahn. Ground state structures in ordered binary alloys with second neighbor interactions. *Acta Met.*, **20**:423, 1972.

[84] S. M. Allen and J. W. Cahn. A correction to the ground state of fcc binary ordered alloys with first and second neighbor pairwise interactions. *Scripta Met.*, **7**:1261, 1973.

[85] T. J. R. Hughes H. M. Hilber and R. L. Taylor. Improved numerical dissipation for time integration algorithms in structural dynamics. *EARTHQ ENG STRUCT D*, **5**:283–292, 1977.

[86] J. S. Biggins, Z. Wei, and L. Mahadevan. Fingering when a fluid invades a highly elastic layer. *Unpublished.*

[87] Alexander E. Lobkovsky. Boundary layer analysis of the ridge singularity in a thin plate. *Phys. Rev. E*, **53**:3750–3759, 1996.

[88] S. P. Timoshenko and J. M. Gere. *Theory of Elastic Stability.* McGraw-Hill, 2nd edition, 1961.

[89] A. Mata, A. J. Fleischman, and S. Roy. Characterization of polydimethylsiloxane (pdms) properties for biomedical micro/nanosystems. *Biomedical Microdevices*, **7**:281–293, 2005.

[90] A. Grinthal, S.H. Kang, A.K Epstein, M. Aizenberg, M. Khan, and J. Aizenberg. Steering nanofibers: An integrative approach to bio-inspired fiber fabrication and assembly. *Nano Today*, **7**:35–52, 2011.

[91] H. Lamb. On the uniform motion of a sphere through a viscous fluid. *Phil. Mag.*, **21**:112, 1911.

[92] A.S. Sangani and A. Acrivos. Slow flow past periodic arrays of cylinders with application to heat transfer. *Int. J. Multiphase Flow*, **8**:193, 1982.

Appendix A

Supplementary material for Chapter 2

The unit cell of a Miura-ori patterned plate is shown in Fig.2.1 and is parameterized by two dihedral angles $\theta \in [0, \pi]$, $\beta \in [0, \pi]$, and one oblique angle α, in a unit cell of length l, width w, and height h. We treat the structure as being made of identical periodic rigid skew plaquettes joined by elastic hinges at the ridges. The structure can deploy uniformly in the plane by having each constituent skew plaquette in a unit cell rotate rigidly about the connecting elastic ridges. Then the ridge lengths l_1, l_2 and $\alpha \in [0, \pi/2]$ are constant through folding/unfolding, so that we may choose θ (or equivalently β) to be the only degree of freedom that completely characterizes a Miura-ori cell. The geometry of the unit cell implies that

$$\begin{aligned} &\beta = 2\sin^{-1}(\zeta \sin(\theta/2)), \quad l = 2l_1\zeta, \\ &w = 2l_2\xi \quad \text{and} \quad h = l_1\zeta \tan\alpha \cos(\theta/2), \end{aligned} \tag{A.1}$$

where the dimensionless width and height are

$$\xi = \sin\alpha \sin(\theta/2) \quad \text{and} \quad \zeta = \cos\alpha(1-\xi^2)^{-1/2}. \tag{A.2}$$

We see that β, l, w, and h change monotonically as $\theta \in [0, \pi]$, with $\beta \in [0, \pi]$, $l \in 2l_1[\cos\alpha, 1]$, $w \in 2l_2[0, \sin\alpha]$, and $h \in l_1[\sin\alpha, 0]$. As $\alpha \in [0, \pi/2]$, we see that $\beta \in [\theta, 0]$, $l \in [2l_1, 0]$, $w \in [0, 2l_2 \sin(\theta/2)]$ and $h \in [0, l_1]$.

Before we discuss the coupled deformations of the plate embodied functionally as $\beta(\alpha, \theta)$, we investigate the case when $\alpha = \pi/2$ corresponding to an orthogonally folded map that can only be completely unfolded first in one direction and then another, without bending or stretching the sheet except along the hinges. Indeed, when $\alpha = \pi/2$ and $\theta \neq \pi$, Eq. (A.1) reduces to $\beta = 0$, $l = 0$ and $h = l_1$, the singular limit when Miura-ori patterned sheets can not be unfolded with a single diagonal pull. Close to this limiting case, when the folds are almost orthogonal, the Miura-ori pattern can remain almost completely folded in the x direction (β changes only by a small amount) while unfolds in the y direction as θ is varied over a large range, only to expand suddenly in the x direction at the last moment. This observation can be explained by expanding Eq. (A.1) asymptotically as $\alpha \to \pi/2$ and $\theta \to \pi$, which yields $\beta \approx \pi - \epsilon/\delta$, $l \approx l_1(2 - (\epsilon/\delta)^2/4)$, $w \approx l_2(2 - \delta^2 - \epsilon^2/4)$ and $h \approx l_1\epsilon/(2\delta)$, where $\delta = \pi/2 - \alpha$ and $\epsilon = \pi - \theta$. Thus, we see that for any fixed small constant δ, only when $\epsilon < \delta$, do we find that $\beta \to \pi$, $l \to 2l_2$ and $h \to 0$, leading to a sharp transition in the narrow neighborhood ($\sim \delta$) of $\theta = \pi$ as $\alpha \to \pi/2$ (Fig.A.1a), consistent with our observations.

More generally, we start by considering the volumetric packing of Miura-ori characterized by the effective volume of a unit cell $V \equiv l \times w \times h = 2l_1^2 l_2 \zeta^2 \sin\theta \sin\alpha \tan\alpha$, which vanishes when $\theta = 0, \pi$. To determine the conditions when the volume is at an extremum for a fixed in-plane angle α, we set $\partial_\theta V|_\alpha = 0$ and find that the maximum volume

$$V_{max}|_\alpha = 2l_1^2 l_2 \sin^2\alpha \quad \text{at} \quad \theta_m = \cos^{-1}\left(\frac{\cos 2\alpha - 1}{\cos 2\alpha + 3}\right), \tag{A.3}$$

shown as a red dashed line in Fig.A.1b. Similarly, for a given dihedral angle θ, we may ask

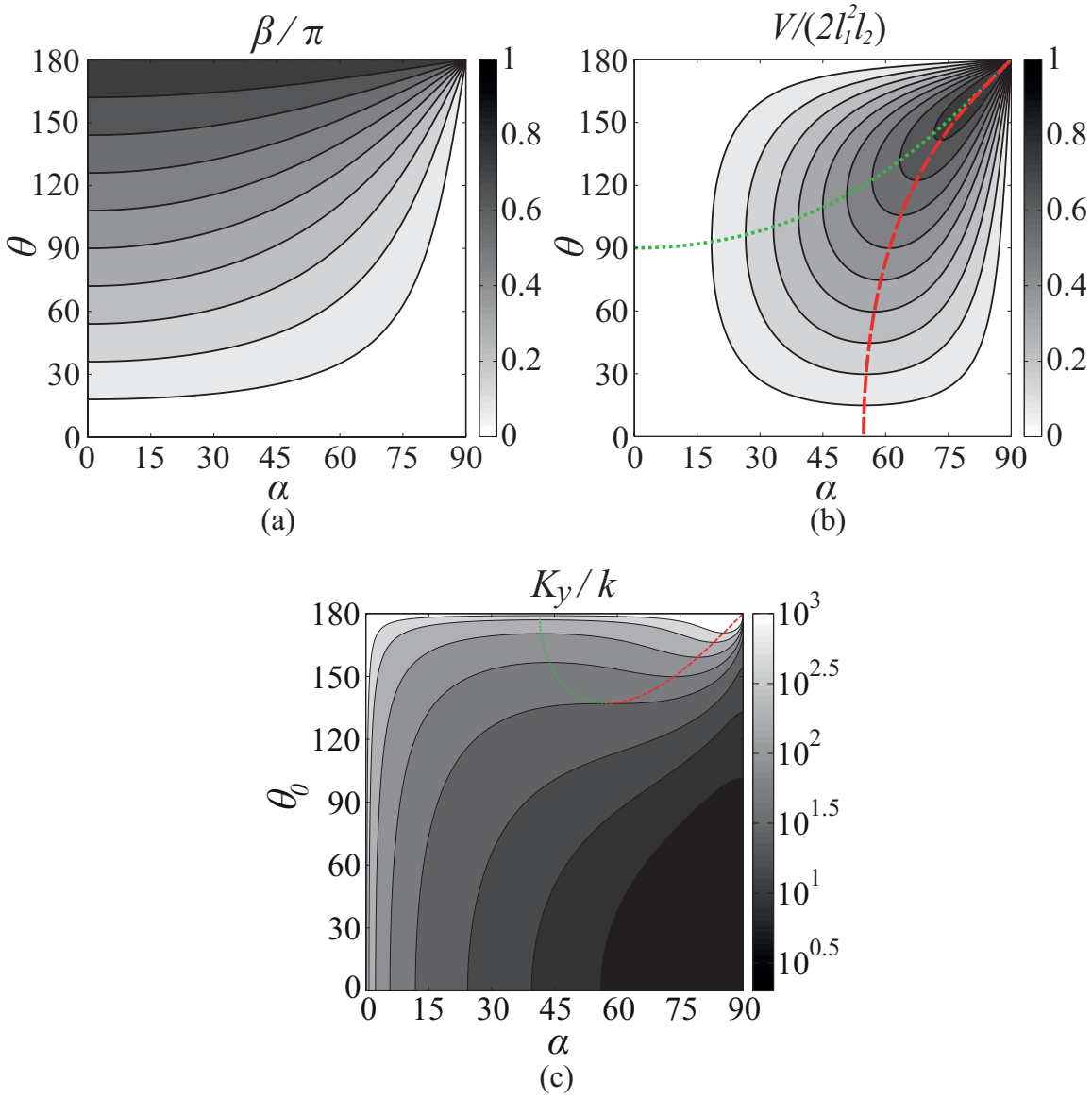

Figure A.1: Geometry of the unit cell as a function of α and θ. (a) The folding angle β increases as θ increases and decreases as α increases. The transition becomes sharper as $\alpha \approx \pi/2$, and when $\alpha = \pi/2$, $\beta = 0$ independent of θ, i.e. the unfolding (folding) of folded (unfolded) of maps with N orthogonal folds has 2^N decoupled possibilities. (b) Effective dimensionless volume $V/(2l_1^2 l_2)$. The green dotted curve $\theta_m(\alpha)$ indicates the optimal design angle pairs that correspond to the maximum $V|_\alpha$. The red dashed curve $\alpha_m(\theta)$ indicates the optimal design angle pairs that correspond to the maximum $V|_\theta$. (c) Contour plot of the dimensionless stretching rigidity K_y/k. $K_y|_\alpha$ is monotonic in θ_0. The green dotted curve indicates the design angle pairs that correspond to the minima of $K_y|_{\theta_0}$. The red dashed curve indicates the design angle pairs that correspond to the maxima of $K_x|_{\theta_0}$. See the text for details.

when the volume is extremized as a function of α? Using the condition $\partial_\alpha V|_\theta = 0$ shows that the maximum volume is given by

$$V_{max}|_\theta = \frac{4l_1^2 l_2 \cos\alpha_m \left(\sqrt{5+4\cos\theta}-3\right)\cot^2(\theta/2)\sin\theta}{\sqrt{5+4\cos\theta}-3-2\cos\theta} \tag{A.4}$$

at

$$\alpha_m = \cos^{-1}\left[\sqrt{\left(2+\cos\theta-\sqrt{5+4\cos\theta}\right)/(\cos\theta-1)}\right],$$

shown as a red dashed line in Fig.A.1b. These relations for the maximum volume as a function of the two angles that characterize the Miura-ori allow us to manipulate the configurations for the lowest density in such applications as packaging for the best protection. In the following sections, we assume each plaquette is a rhombus, i.e. $l_1 = l_2 = l_e$, to keep the size of the algebraic expressions manageable, although it is a relatively straightforward matter to account for variations from this limit.

A.1 In-plane stretching response of a Miura-ori plate

A.1.1 Poisson's ratio related to height changes

Poisson's ratios related to height changes, ν_{hl} and ν_{wl} read

$$\begin{aligned}\nu_{hl} &= \nu_{lh}^{-1} \equiv -\frac{dh/h}{dl/l} = \cot^2\alpha\sec^2\frac{\theta}{2},\\ \nu_{hw} &= \nu_{wh}^{-1} \equiv -\frac{dh/h}{dw/w} = \zeta^2\tan^2\frac{\theta}{2}.\end{aligned} \tag{A.5}$$

which are both positive, and monotonically increasing with θ and α. Expansion of ν_{hl} in Eq. (A.5) shows that $\nu_{hl}|_{\theta\to\pi} \sim (\pi-\theta)^{-2}$ and thus $\nu_{hl}|_\alpha \in [\cot^2\alpha, \infty)$, while $\nu_{hl}|_{\alpha\to 0} \sim \alpha^{-2}$ and thus $\nu_{hl}|_\theta \in (\infty, 0]$. Similarly, expansion of ν_{hw} in Eq. (A.5) shows that $\nu_{hw}|_{\theta\to\pi} \sim (\pi-\theta)^{-2}$ and thus $\nu_{hw}|_\alpha \in [0,\infty)$, while $\nu_{hw}|_\theta \in [\tan^2(\theta/2), 0]$. Finally, it is worth pointing out that ν_{hw} has a singularity at $(\alpha,\theta) = (\pi/2, \pi)$.

A.1.2 Stretching stiffness K_x and K_y

Here we derive the expressions for stretching stiffness K_x and K_y.

The expression for the potential energy of a unit cell deformed by a uniaxial force f_x in the x direction is given by

$$H = U - \int_{\theta_0}^{\theta} f_x \frac{dl}{d\theta'} d\theta', \tag{A.6}$$

where the unit cell length l is defined in Eq. (A.1). The elastic energy of a unit cell U is stored only in the elastic hinges which allow the plaquettes to rotate, and is given by

$$U = k l_e (\theta - \theta_0)^2 + k l_e (\beta - \beta_0)^2, \tag{A.7}$$

where k is the hinge spring constant, and θ_0 and β_0 $(= \beta(\alpha, \theta_0))$ are the natural dihedral angles in the undeformed state. The external force f_x at equilibrium state is obtained using the condition that the first variation $\delta H/\delta\theta = 0$, which reads

$$f_x = \frac{dU/d\theta}{dl/d\theta} = 2k \frac{(\theta - \theta_0) + (\beta - \beta_0)\varpi(\alpha, \theta)}{\eta(\alpha, \theta)}, \tag{A.8}$$

where U is defined in Eq. (A.7), l is defined in Eq. (A.1), and in addition

$$\varpi(\alpha, \theta) = \frac{\cos\alpha}{1 - \xi^2} \quad \text{and} \quad \eta(\alpha, \theta) = \frac{\cos\alpha \sin^2\alpha \sin\theta}{2(1 - \xi^2)^{3/2}}. \tag{A.9}$$

The stretching rigidity associated with the x direction is thus given by

$$K_x(\alpha, \theta_0) \equiv \left.\frac{df_x}{d\theta}\right|_{\theta_0} = 4k \frac{(1 - \xi_0^2)^2 + \cos^2\alpha}{(1 - \xi_0^2)^{\frac{1}{2}} \cos\alpha \sin^2\alpha \sin\theta_0}, \tag{A.10}$$

where $\xi_0 = \xi(\alpha, \theta_0)$.

Similarly, the uniaxial force in the y direction in a unit cell at equilibrium is

$$f_y = \frac{dU/d\theta}{dw/d\theta} = 2k \frac{(\theta - \theta_0) + (\beta - \beta_0)\varpi(\alpha, \theta)}{\sin\alpha \cos(\theta/2)}, \tag{A.11}$$

where w is defined in Eq. (A.1) and ϖ is defined in Eq. (A.9). The stretching rigidity in y direction is thus given by

$$K_y(\alpha,\theta_0) \equiv \left.\frac{df_y}{d\theta}\right|_{\theta_0} = 2k\frac{(1-\xi_0^2)^2+\cos^2\alpha}{(1-\xi_0^2)^2\sin\alpha\cos(\theta_0/2)}, \tag{A.12}$$

of which the contour plot is show in Fig. A.1c.

A.1.3 Asymptotic cases for optimal design angles

The expressions in Section A.1.2 allow us to derive in detail all the asymptotic cases associated with the optimal pairs of design angles which correspond to the extrema of stretching rigidities K_x and K_y. For simplicity, we use (α,θ) instead of (α,θ_0) to represent the design angle pairs when the unit cell is at rest.

1. Expanding $\partial_\theta K_x$ in the neighborhood of $\alpha = 0$ yields

$$\partial_\theta K_x|_{\alpha\to 0} = -\frac{8\cot\theta\csc\theta}{\alpha^2} - \frac{2}{3}\left((3+\cos\theta)\csc^2\theta\right) + O(\alpha^2). \tag{A.13}$$

   As $\alpha \to 0$, $\theta \to \pi/2$ to prevent a divergence. Continuing to expand Eq. (A.13) in the neighborhood of $\theta = \pi/2$ and keeping the first two terms yields

$$\partial_\theta K_x|_{\theta\to\pi/2} = 0 \Rightarrow 4(\theta-\pi/2) = \alpha^2. \tag{A.14}$$

   Therefore in the contour plot of K_x (Fig.3b in the main text), the greed dotted curve is approximated by $4(\theta-\pi/2)=\alpha^2$ in the neighborhood of $\alpha = 0$, and is perpendicular to $\alpha = 0$ as θ is quadratic in α.

2. Expanding $\partial_\alpha K_x$ in the neighborhood of $\theta = 0$ yields

$$\begin{aligned}\partial_\alpha K_x|_{\theta\to 0} = &-\frac{[11+20\cos(2\alpha)+\cos(4\alpha)]\csc^3\alpha\sec^2\alpha}{2\theta}\\ &-\frac{1}{192}\{[290+173\cos(2\alpha)+46\cos(4\alpha)+3\cos(6\alpha)]\\ &\csc^3\alpha\sec^2\alpha\}\,\theta + O(\theta^2).\end{aligned} \tag{A.15}$$

The numerator of the leading order in Eq. (A.15) has to vanish as $\theta \to 0$ to keep the result finite, which results in a unique solution $\alpha^* = \cos^{-1}\left(\sqrt{\sqrt{5}-2}\right)$ in the domain $\alpha \in (0, \pi/2)$. Continuing to expand Eq. (A.15) in the neighborhood of $\alpha = \alpha^*$ and only keeping the first two terms yields

$$\partial_\alpha K_x = 0|_{\alpha\to\alpha^*} \Rightarrow 4\sqrt{5(1+\sqrt{5})}(\alpha - \alpha^*) = \theta^2. \tag{A.16}$$

so the red dashed curve in the contour plot of K_x (Fig.3b in the main text) is perpendicular to $\theta = 0$.

3. Similarly, Expansion of $\partial_\alpha K_y$ near $\theta = \pi$ yields

$$\begin{aligned}\partial_\alpha K_y|_{\theta\to\pi} =& \frac{[-1+16\cos(2\alpha)+\cos(4\alpha)]\csc^2\alpha\sec^3\alpha}{2(\theta-\pi)} \\ &+ \frac{1}{192}[638 - 737\cos(2\alpha) + 162\cos(4\alpha) + \cos(6\alpha)] \\ &\csc^2\alpha\sec^5\alpha(\theta-\pi) + O[(\theta-\pi)^3].\end{aligned} \tag{A.17}$$

Allowing for a well behaved limit at leading order as $\theta \to \pi$ requires $-1+16\cos(2\alpha)+\cos(4\alpha) = 0$ and yields $\alpha^* = \cos^{-1}\left(\sqrt{(\sqrt{17}-3)/2}\right)$ as the unique solution when α is an acute. Again expanding Eq. (A.17) in the neighborhood of $\theta = \pi$, and only keeping the first two terms yields

$$\partial_\alpha K_y|_{\alpha\to\alpha^*} = 0 \Rightarrow 2\sqrt{1+\sqrt{17}}(\alpha_m - \alpha^*) = (\pi-\theta)^2. \tag{A.18}$$

So the green dotted curve in the contour plot of K_y (Fig. A.1c) is approximated by $2\sqrt{1+\sqrt{17}}(\alpha_m - \alpha^*) = (\pi-\theta)^2$ near $\alpha = \alpha^*$, and is perpendicular to $\theta = \pi$. The point where the green curve ends satisfies the condition

$$\partial_\alpha K_y = 0 \quad \text{and} \quad \partial_\alpha\left(\partial_\alpha K_y\right) = 0 \tag{A.19}$$

and numerical calculation gives us the coordinates of this critical point as

$$\theta = 2.39509, \quad \text{and} \quad \alpha = 1.00626. \tag{A.20}$$

The red dashed curve (Fig. A.1c) starting at this point shows a collection of optimal design angle pairs (α, θ) where $K_y|_\theta$ is locally maximal.

A.2 Out-of-plane bending response of a Miura-ori plate

A.2.1 Minimum model for isometric bending

Here we show that planar folding is the only geometrically possible motion under the assumption that the unit cell deforms isometrically, i.e. with only rotations of the rhombus plaquettes about the hinges. To enable the out-of-plane bending mode, the minimum model for isometric deformations requires the introduction of 1 additional diagonal fold into each plaquette, and this follows from the explanation below.

Suppose the plane $O_1O_2O_5O_4$ (Fig.A.2a) is fixed to eliminate all rigid motions, for any dihedral angle θ, the orientation of plane $O_1O_2O_8O_7$ is determined. However, the other two rhombi $O_2O_5O_6O_3$ and $O_2O_3O_9O_8$ are free to rotate about axis O_2O_5 and O_2O_8 respectively and sweep out two cones which intersect at O_2O_3 and O_2O_3'. Fig.A.2a shows the two possible configurations of a unit cell determined from the two intersections, the yellow part being the red part that has been flipped about a plane of symmetry. The unit cell in red is the only nontrivial Miura pattern, so that for any given θ, there is a unique configuration of the unit cell corresponding to it. Any continuous change in θ results in the unit cell being expanded or folded but remaining planar, in which case, O_1, O_4, O_7, O_3, O_6 and O_9 also remain coplanar. In order to enable the bending mode of the unit cell, the planarity of each plaquette must be violated. In the limit where the plaquette thickness $t \ll 1$ the stretching rigidity ($\sim t$) is much larger than the bending rigidity ($\sim t^3$), with t being the thickness of a plaquette, while the energy required to bend a strip of ridge is 5 times of that required to stretch it according to the asymptotic analysis of the *Föppl – von Kármán*

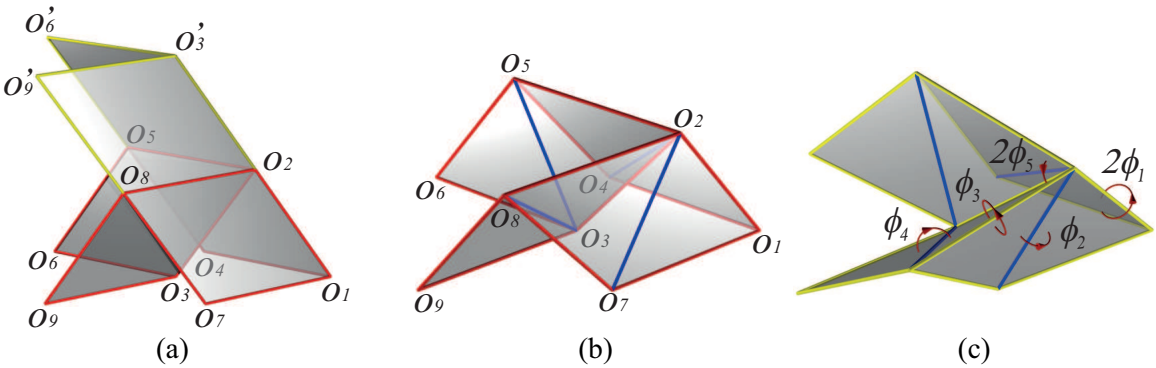

Figure A.2: Bending of a unit cell. (a) The two configurations of a unit cell for any given θ if each plaquette is a rigid rhombus. The only possible motion is in-plane stretching. The yellow plaquettes illustrate the trivial configuration of two rigid plaquettes and the red ones show the typical configuration of a Miura-ori unit cell. (b) The undeformed state. An additional fold along the short diagonal is introduced to divide each rhombus into 2 elastically hinged triangles. (c) Symmetrically bent state. The bending angles around axis $\overrightarrow{O_2O_4}$ and $\overrightarrow{O_3O_5}$ are the same as those around $\overrightarrow{O_7O_2}$ and $\overrightarrow{O_8O_3}$ respectively.

equations [87]. Therefore, the rigid ridge/fold is an excellent approximation for out-of-plane bending when $t \ll 1$. Then, to get a bent shape in a unit cell and thence in a Miura-ori plate, we must introduce an additional fold into each rhombus to divide it into two elastically hinged triangles (Fig.A.2b). As a result, 4 additional degrees of freedom are introduced in each unit cell. The deformed state can either be symmetrical about the plane $O_1O_2O_3$ (Fig.A.2c) corresponding to a bending mode, or unsymmetrical corresponding to a twisting mode. Here, we are only interested in the bent state, in which the rotation angle ϕ_2 about the axis $\overrightarrow{O_2O_4}$, and ϕ_4 about the axis $\overrightarrow{O_3O_5}$, are the same as the rotations about $\overrightarrow{O_7O_2}$ and $\overrightarrow{O_8O_3}$ respectively. The rotation angles about the axis $\overrightarrow{O_1O_2}$, $\overrightarrow{O_3O_2}$ and $\overrightarrow{O_2O_5}$ are $2\phi_1$, $2\phi_5$ and ϕ_3 respectively. ($\rightarrow$ indicates the direction.)

A.2.2 Curvatures and the bending Poisson's ratio when short folds are introduced

Here we derive expressions for the coordinates of every vertex of the unit cell after bending in the linear deformation regime, from which curvatures in the two principle directions κ_x, κ_y and the bending Poisson's ratio $\nu_b = -\kappa_y/\kappa_x$ can be calculated.

To do so, we first need to know the transformation matrix associated with rotation about an arbitrary axis. The rotation axis is defined by a point $\{a, b, c\}$ that it goes through and a direction vector $< u, v, w >$, where u, v, w are directional cosines. Suppose a point $\{x_0, y_0, z_0\}$ rotates about this axis by an infinitesimal small angle ω ($\omega \ll 1$), and reaches the new position $\{x, y, z\}$. Keeping only the leading order terms of the transformation matrix, we find that the new position $\{x, y, z\}$ is given by

$$\begin{aligned} x &= x_0 + (-cv + bw - wy_0 + vz_0)\omega, \\ y &= y_0 + (cu - aw + wx_0 - uz_0)\omega, \\ z &= z_0 + (-bu + av - vx_0 + uy_0)\omega. \end{aligned} \tag{A.21}$$

Given Eq. (A.21), we are ready to calculate the coordinates of all vertices in the bent sate. Assuming that the origin is at O_2, in the undeformed unit cell, edge O_1O_2 is fixed in xoz plane to eliminate rigid motions. Each fold deforms linearly by angle $2\phi_1$, ϕ_2, ϕ_3, ϕ_4 and $2\phi_5$ (see Fig. A.2c) around corresponding axes respectively. The coordinates of O_1 and O_2 are

$$\begin{aligned} &O_{1x} = \frac{\cos\alpha}{\sqrt{1-\xi^2}}, \quad O_{1y} = 0, \quad O_{1z} = -\frac{\sin\alpha\cos(\theta/2)}{\sqrt{1-\xi^2}}; \\ &O_{2x} = 0, \quad O_{2y} = 0, \quad O_{2z} = 0. \end{aligned} \tag{A.22}$$

The coordinates of O_3 after bending are

$$\begin{aligned}
O_{3x} =& -\frac{\cos\alpha}{\sqrt{1-\sin^2\alpha\sin^2(\theta/2)}} - \frac{\cos(\alpha/2)\sin\alpha\sin\theta}{\sqrt{3-\cos(2\alpha)(\cos\theta-1)+\cos\theta}}\phi_2 \\
&+ \frac{\sin^2\alpha\sin\theta}{2\sqrt{1-\sin^2\alpha\sin^2(\theta/2)}}\phi_3, \\
O_{3y} =& -\frac{4\cos(\theta/2)\sin(2\alpha)}{3+\cos(2\alpha)+2\cos\theta\sin^2\alpha}\phi_1 \\
&+ \frac{\csc(\theta/2)[-\sin\alpha+\sin(2\alpha)+\sin^3\alpha\sin^2(\theta/2)]\sin\theta}{[3+\cos(2\alpha)+2\cos(\theta)\sin^2\alpha]\sin(\alpha/2)}\phi_2 \\
&+ \cos(\theta/2)\sin(\alpha)\phi_3, \\
O_{3z} =& -\frac{\cos(\theta/2)\sin\alpha}{\sqrt{1-\sin^2\alpha\sin^2(\theta/2)}} + \frac{2\cos\alpha\cos(\alpha/2)\sin(\theta/2)}{\sqrt{3-\cos(2\alpha)(\cos\theta-1)+\cos\theta}}\phi_2 \\
&- \frac{\cos\alpha\sin\alpha\sin(\theta/2)}{\sqrt{1-\sin^2\alpha\sin^2(\theta/2)}}\phi_3.
\end{aligned} \tag{A.23}$$

The coordinates of O_4 after bending are

$$\begin{aligned}
O_{4x} =& \frac{\cos\alpha+\sin^2\alpha\sin^2(\theta/2)-1}{\sqrt{1-\sin^2\alpha\sin^2(\theta/2)}} - \frac{\sin^2\alpha\sin\theta}{\sqrt{3-\cos(2\alpha)(\cos\theta-1)+\cos\theta}}\phi_1, \\
O_{4y} =& \sin\alpha\sin(\theta/2) - \cos(\theta/2)\sin\alpha\phi_1, \\
O_{4z} =& -\frac{\cos(\theta/2)\sin\alpha}{\sqrt{1-\sin^2\alpha\sin^2(\theta/2)}} - \frac{2\cos\alpha\sin\alpha\sin(\theta/2)}{\sqrt{3-\cos(2\alpha)(\cos\theta-1)+\cos\theta}}\phi_1.
\end{aligned} \tag{A.24}$$

The coordinates of O_5 after bending are

$$\begin{aligned}
O_{5x} =& -\sqrt{1-\sin^2\alpha\sin^2(\theta/2)} - \frac{\sin^2\alpha\sin\theta}{\sqrt{3-\cos(2\alpha)(\cos\theta-1)+\cos\theta}}\phi_1 \\
&+ \frac{\sin^2\alpha\sin\theta}{2\sqrt{3-\cos(2\alpha)(\cos\theta-1)+\cos\theta}\sin(\alpha/2)}\phi_2, \\
O_{5y} =& \sin\alpha\sin(\theta/2) - \cos(\theta/2)\sin\alpha\phi_1 + \frac{\cos(\theta/2)\sin\alpha}{2\sin(\alpha/2)}\phi_2, \\
O_{5z} =& -\frac{2\cos\alpha\sin\alpha\sin(\theta/2)}{\sqrt{3-\cos(2\alpha)(\cos\theta-1)+\cos\theta}}\phi_1 \\
&+ \frac{\cos\alpha\sin\alpha\sin(\theta/2)}{\sqrt{3-\cos(2\alpha)(\cos\theta-1)+\cos\theta}\sin(\alpha/2)}\phi_2.
\end{aligned} \tag{A.25}$$

The coordinates of O_6 after bending are

$$\begin{aligned}
O_{6x} =& \frac{\sin^2\alpha\sin^2(\theta/2)-\cos\alpha-1}{\sqrt{1-\sin^2\alpha\sin^2(\theta/2)}} - \frac{\sin^2\alpha\sin\theta}{\sqrt{3-\cos(2\alpha)(\cos\theta-1)+\cos\theta}}\phi_1 \\
&+ \frac{\sin^2\alpha\sin\theta}{2\sqrt{1-\sin^2\alpha\sin^2(\theta/2)}}\phi_3 - \frac{\sin\alpha\sin\theta\cos(\alpha/2)}{\sqrt{3-\cos(2\alpha)(\cos\theta-1)+\cos\theta}}\phi_4, \\
O_{6y} =& \sin\alpha\sin(\theta/2) + \frac{4\cos(\theta/2)\sin\alpha[\sin^2\alpha\sin^2(\theta/2)-1-2\cos\alpha]}{3+\cos(2\alpha)+2\cos\theta\sin^2\alpha}\phi_1 \\
&+ \frac{8\cos\alpha\cos(\theta/2)\cos(\alpha/2)}{3+\cos(2\alpha)+2\cos\theta\sin^2\alpha}\phi_2 + \cos(\theta/2)\sin\alpha\phi_3 \\
&- \cos(\theta/2)\cos(\alpha/2)\phi_4, \\
O_{6z} =& -\frac{\cos(\theta/2)\sin\alpha}{\sqrt{1-\sin^2\alpha\sin^2(\theta/2)}} - \frac{2\cos\alpha\sin\alpha\sin(\theta/2)}{\sqrt{3-\cos(2\alpha)(\cos\theta-1)+\cos\theta}}\phi_1 \\
&+ \frac{\csc(\alpha/2)\sin(2\alpha)\sin(\theta/2)}{\sqrt{3-\cos(2\alpha)(\cos\theta-1)+\cos\theta}}\phi_2 - \frac{\cos\alpha\sin\alpha\sin(\theta/2)}{\sqrt{1-\sin^2\alpha\sin^2(\theta/2)}}\phi_3 \\
&+ \frac{2\cos\alpha\cos(\alpha/2)\sin(\theta/2)}{\sqrt{3-\cos(2\alpha)(\cos\theta-1)+\cos\theta}}\phi_4.
\end{aligned} \tag{A.26}$$

The coordinates of O_7, O_8 and O_9 after bending are

$$\begin{aligned}
&\{O_{7x}, O_{7y}, O_{7z}\} = \{O_{4x}, -O_{4y}, O_{4z}\}, \quad \{O_{8x}, O_{8y}, O_{8z}\} = \{O_{5x}, -O_{5y}, O_{5z}\}, \\
&\{O_{9x}, O_{9y}, O_{9z}\} = \{O_{6x}, -O_{6y}, O_{6z}\}.
\end{aligned} \tag{A.27}$$

Due to symmetry, O_3 must lie in the xoz plane after bending, so $O_{3y} = 0$, from which ϕ_3 and ϕ_5 can be expressed as a function of ϕ_1 and ϕ_2,

$$\begin{aligned}
\phi_3 =& \frac{8\cos\alpha}{3+\cos(2\alpha)+2cos\theta\sin^2\alpha}\phi_1 \\
&+ \frac{1}{2}\csc\left(\frac{\alpha}{2}\right)\left(1-\frac{8\cos\alpha}{3+\cos(2\alpha)+2\cos\theta\sin^2\alpha}\right)\phi_2. \\
\phi_5 =& \phi_1 - \frac{1}{2}\csc\left(\frac{\alpha}{2}\right)\phi_2
\end{aligned} \tag{A.28}$$

The curvature of the unit cell in the x direction is defined as the dihedral angle formed by rotating plane $O_4O_1O_7$ to plane $O_6O_3O_9$ projected onto the x direction over the unit length l. The sign of the angle follows the right-hand rule about the y axis. The

dihedral angle between plane $O_4O_1O_7$ and plane xoy is

$$\Omega_{417} = \frac{O_{4z} - O_{1z}}{\sqrt{1-\xi^2}} = -\frac{4\cos\alpha\sin\alpha\sin(\theta/2)}{3+\cos(2\alpha)+2\cos\theta\sin^2\alpha}\phi_1, \tag{A.29}$$

and the dihedral angle between plane $O_3O_6O_9$ and plane xoy is

$$\begin{aligned}\Omega_{639} &= \frac{O_{6z} - O_{3z}}{\sqrt{1-\xi^2}} \\ &= \frac{2[\cos(\alpha/2)+\cos(3\alpha/2)][\phi_2+\phi_4-2\phi_1\sin(\alpha/2)]\sin(\theta/2)}{3+\cos(2\alpha)+2\cos\theta\sin^2\alpha}.\end{aligned} \tag{A.30}$$

The curvature κ_x hence is

$$\kappa_x = \frac{\Omega_{639} - \Omega_{417}}{l} = \frac{(\phi_2+\phi_4)\cos(\alpha/2)\sin(\theta/2)}{2\sqrt{1-\xi^2}}. \tag{A.31}$$

The curvature of the unit cell in the y direction is defined as the dihedral angle between plane $O_4O_5O_6$ and $O_7O_8O_9$ projected onto the y direction over the unit cell width w, which is expressed as

$$\kappa_y = -\frac{2O_{5y} - O_{4y} - O_{3y}}{hw} = -\frac{1}{4}(\phi_2+\phi_4)\csc\left(\frac{\alpha}{2}\right)\csc\alpha\csc\left(\frac{\theta}{2}\right)\sqrt{1-\xi^2}. \tag{A.32}$$

From Eq. (A.31) and Eq. (A.32), we can calculate the bending Poisson ratio, which is simplified to

$$\nu_b = -\frac{\kappa_y}{\kappa_x} = -1 + \csc^2\alpha\csc^2\left(\frac{\theta}{2}\right). \tag{A.33}$$

A.2.3 Curvatures and the bending Poisson's ratio when long folds are introduced

In Fig.A.2, if we introduce the additional fold along the long diagonal, e.g. O_1O_5, instead of the short one, the unit cell can be bent too. In this case, ϕ_2 and ϕ_4 are bending angles around axis $\overrightarrow{O_1O_5}$ and $\overrightarrow{O_2O_6}$ respectively. O_1, O_2 do not change as they are fixed,

and coordinates of O_3 after bending are

$$\begin{aligned}
O_{3x} =& -\frac{\cos\alpha}{\sqrt{1-\sin^2\alpha\sin^2(\theta/2)}} + \frac{\sin^2\alpha\sin\theta}{2\sqrt{1-\sin^2\alpha\sin^2(\theta/2)}}\phi_3 \\
& - \frac{\sin\alpha\sin(\alpha/2)\sin\theta}{\sqrt{3-\cos(2\alpha)(\cos\theta-1)+\cos\theta}}\phi_4, \\
O_{3y} =& -\frac{4\cos(\theta/2)\sin(2\alpha)}{3+\cos(2\alpha)+2\cos\theta\sin^2\alpha}\phi_1 + \cos\left(\frac{\theta}{2}\right)\sin(\alpha)\phi_3 \\
& - \cos\left(\frac{\theta}{2}\right)\sin\left(\frac{\alpha}{2}\right)\phi_4, \\
O_{3z} =& -\frac{\cos(\theta/2)\sin(\alpha)}{\sqrt{1-\sin^2\alpha\sin^2(\theta/2)}} - \frac{\cos\alpha\sin\alpha\sin(\theta/2)}{\sqrt{1-\sin^2\alpha\sin^2(\theta/2)}}\phi_3 \\
& + \frac{2\cos\alpha\sin(\alpha/2)\sin(\theta/2)}{\sqrt{3-\cos(2\alpha)(\cos\theta-1)+\cos\theta}}\phi_4.
\end{aligned} \tag{A.34}$$

The coordinates of O_4 after bending are

$$\begin{aligned}
O_{4x} =& \frac{\cos\alpha - 1 + \sin^2\alpha\sin^2(\theta/2)}{\sqrt{1-\sin^2\alpha\sin^2(\theta/2)}} \\
& - \frac{\sin^2\alpha\sin\theta}{\sqrt{3-\cos(2\alpha)(\cos\theta-1)+\cos\theta}}\left[\phi_1 - \frac{1}{2}\sec\left(\frac{\alpha}{2}\right)\phi_2\right], \\
O_{4y} =& \sin\alpha\sin(\theta/2) - \cos(\theta/2)\sin\alpha\phi_1 + \cos(\theta/2)\sin(\alpha/2)\phi_2, \\
O_{4z} =& -\frac{\cos(\theta/2)\sin\alpha}{\sqrt{1-\sin^2\alpha\sin^2(\theta/2)}} \\
& - \frac{2\cos\alpha\sin(\theta/2)\sin(\alpha/2)}{\sqrt{3-\cos(2\alpha)(\cos\theta-1)+\cos\theta}}\left[2\cos\left(\frac{\alpha}{2}\right)\phi_1 - \phi_2\right].
\end{aligned} \tag{A.35}$$

The coordinates of O_5 after bending are

$$\begin{aligned}
O_{5x} =& -\sqrt{1-\sin^2\alpha\sin^2\left(\frac{\theta}{2}\right)} - \frac{\sin^2\alpha\sin\theta}{\sqrt{3-\cos(2\alpha)(\cos\theta-1)+\cos\theta}}\phi_1, \\
O_{5y} =& \sin\alpha\sin(\theta/2) - \cos(\theta/2)\sin\alpha\phi_1, \\
O_{5z} =& -\frac{\sin(2\alpha)\sin(\theta/2)}{\sqrt{3-\cos(2\alpha)(\cos\theta-1)+\cos\theta}}\phi_1.
\end{aligned} \tag{A.36}$$

The coordinates of O_6 after bending are

$$\begin{aligned}
O_{6x} =& \frac{\sin^2\alpha\sin^2(\theta/2)-\cos\alpha-1}{\sqrt{1-\sin^2\alpha\sin^2(\theta/2)}} - \frac{\sin^2\alpha\sin\theta}{\sqrt{3-\cos(2\alpha)(\cos\theta-1)+\cos\theta}}\phi_1 \\
&+ \frac{\sin^2\alpha\sin\theta}{2\sqrt{1-\sin^2\alpha\sin^2(\theta/2)}}\phi_3, \\
O_{6y} =& \sin\alpha\sin\left(\frac{\theta}{2}\right) + \frac{4\cos(\theta/2)\sin\alpha\left[-1-2\cos\alpha+\sin^2\alpha\sin^2(\theta/2)\right]}{3+\cos(2\alpha)+2\cos\theta\sin^2\alpha}\phi_1 \\
&+ \cos\left(\frac{\theta}{2}\right)\sin\alpha\phi_3, \\
O_{6z} =& -\frac{\cos(\theta/2)\sin\alpha}{\sqrt{1-\sin^2\alpha\sin^2(\theta/2)}} - \frac{\sin(2\alpha)\sin(\theta/2)}{\sqrt{3-\cos(2\alpha)(\cos\theta-1)+\cos\theta}}\phi_1 \\
&- \frac{\cos\alpha\sin\alpha\sin(\theta/2)}{\sqrt{1-\sin^2\alpha\sin^2(\theta/2)}}\phi_3.
\end{aligned} \tag{A.37}$$

Using the same idea for the long fold case as we did for the short fold, we can also calculate the curvatures in the two principal directions and find that

$$\begin{aligned}
\kappa_x = \frac{\Omega_{639}-\Omega_{417}}{l} &= \frac{2\left[\sin(\alpha/2)-\sin(3\alpha/2)\right]\sin(\theta/2)}{\left[3+\cos(2\alpha)+2\cos\theta\sin^2\alpha\right]l}(\phi_2+\phi_4) \\
&= \frac{\sin(\alpha/2)\sin(\theta/2)}{2l_e\sqrt{1-\xi^2}}(\phi_2+\phi_4),
\end{aligned} \tag{A.38}$$

while

$$\begin{aligned}
\kappa_y = -\frac{2O_{5y}-O_{4y}-O_{3y}}{hw} &= -\frac{\sqrt{1-\sin^2\alpha\sin^2(\theta/2)}}{2\cos(\alpha/2)w}(\phi_2+\phi_4) \\
&= -\frac{\sqrt{1-\xi^2}}{4l_e\cos(\alpha/2)\,\xi}(\phi_2+\phi_4).
\end{aligned} \tag{A.39}$$

Therefore the bending Poisson ratio is

$$\nu_b = -\frac{\kappa_y}{\kappa_x} = -1+\csc^2\alpha\csc^2\left(\frac{\theta}{2}\right), \tag{A.40}$$

which is the same as that of the case when the short folds are introduced.

A.2.4 Bending stiffness B_x and B_y

We are now in a position to derive expressions for the bending stiffness B_x and B_y. On one hand, the bending energy is physically stored in the 8 discrete folds, which can be

expressed as $1/2kl_e[4\phi_1^2 + 4\sin(\alpha/2)\phi_2^2 + 2\phi_3^2 + 4\sin(\alpha/2)\phi_4^2 + 4\phi_5^2]$. On the other hand from a continuum point of view, the energy may also be effectively considered as stored in the entire unit cell that is bent into the curvature κ_x, which can be expressed as $1/2B_x wl\kappa_x^2$. Equating the two expressions for the same energy, we can write B_x as

$$B_x = kl_e \frac{4\phi_1^2 + 4\sin(\frac{\alpha}{2})\phi_2^2 + 2\phi_3^2 + 4\sin(\frac{\alpha}{2})\phi_4^2 + 4\phi_5^2}{wl\kappa_x^2}. \tag{A.41}$$

Similarly, the bending stiffness per unit width of a single cell in the y direction is

$$B_y(\alpha, \theta) = kl_e \frac{4\phi_1^2 + 4\sin(\frac{\alpha}{2})\phi_2^2 + 2\phi_3^2 + 4\sin(\frac{\alpha}{2})\phi_4^2 + 4\phi_5^2}{wl\kappa_y^2} \tag{A.42}$$

A.2.5 Pure bending

Finally, we explain the "pure bending" situation in the main text, borrowing ideas from notions of the pure bending of a beam where curvature is constant. If we demand that a row of unit cells aligned in the x direction (e.g. the cell C_1 and C_2 in Fig.A.3) undergo exactly the same deformation, this results in $\phi_2 = \phi_4$. Furthermore, in this limit, the stretching mode is constrained, so that $\phi_1 = 0$ for all cells. For this well defined bending deformation, the bending stiffness depends only on the design angles, not on the deformation angles as shown in Eq. (A.41) and Eq. (A.42).

A.3 Numerical simulations of the bending response of a Miura-ori plate

A.3.1 Homogeneous deformation in bent plate is impossible

Here we explain why it is impossible to assemble an entire bent plate by periodically aligning unit cells with identical bending deformation in both the x and y direction.

In Fig.A.3, the 4 unit cells C_1, C_2, C_3 and C_4 have identical bending deformations: C_1 and C_2 align perfectly in the x direction, which requires that $\angle O_4O_1O_7 = \angle O_6O_3O_9 = \angle O_{11}O_{13}O_{15}$. C_1 and C_3, C_2 and C_4 align perfectly in the y direction respectively, which is automatically satisfied by the symmetry of the unit cell. Now the question becomes whether the unit cell C_3 and C_4 can align together? The answer is no. The reasoning is as follows. O_3 and $O_3^{'}$ are symmetric about plane $O_6O_{12}O_{13}$, while O_3 and $O_3^{''}$ are symmetric about plane $O_4O_5O_6$. However plane $O_6O_{12}O_{13}$ and plane $O_4O_5O_6$ are not coplanar unless all the deformation angles about the internal folds are zero, which is violated by bending. $O_3^{'}$ and $O_3^{''}$ thus do not coincide. In fact $O_3^{'} = O_3^{''}$ if and only if $O_{3y} = O_{5y} = O_{6y}$, which requires $\phi_2 = \phi_4 = 0$ from Eq. (A.24), Eq. (A.25), Eq. (A.26) and Eq. (A.28). This is the in-plane stretching mode instead of the bending mode. In conclusion, in the bent Miura-ori plate, the deformation must be inhomogeneous.

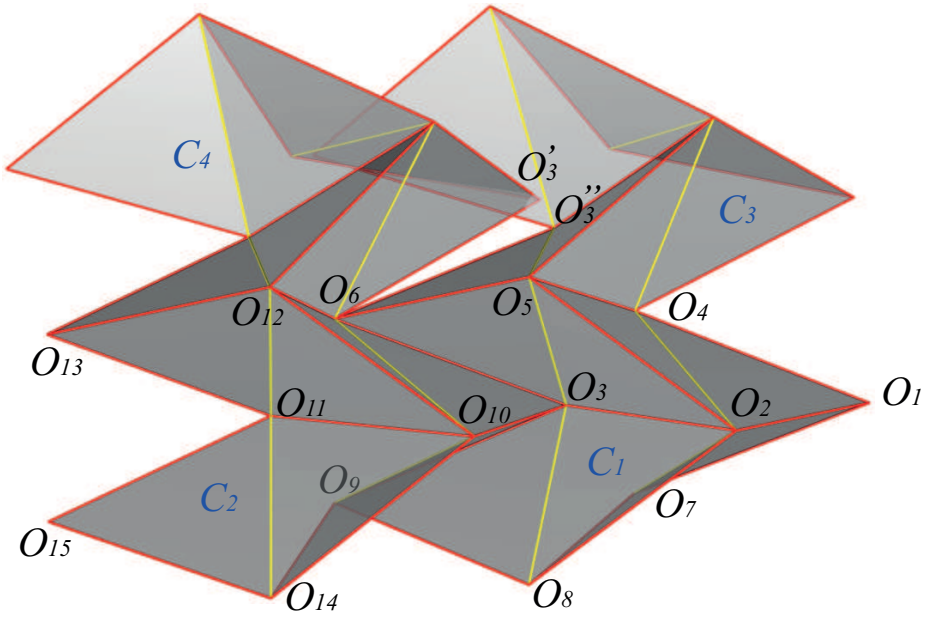

Figure A.3: 4 unit cells with identical bending deformation cannot be aligned together to form an entire plate. See the text for details.

A.3.2 Simulation model

In this subsection, we explain the bending model and the strategies used to bend the Miura-ori plate.

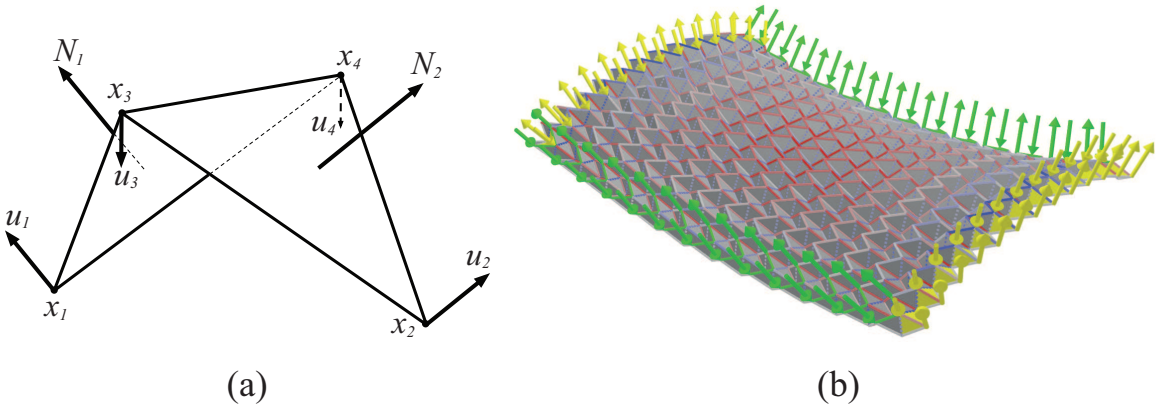

Figure A.4: Simulation model. (a) A single bending adjacency. The vectors u_i illustrate the purely geometric bending mode and N_1 and N_2 are the weighted normals of the adjacent triangles. (b) The left-right bending strategy is shown in yellow and the up-down bending strategy is shown in green. Each arrow represents a force applied to its incident vertex. Left-right force directions bisect the yellow adjacencies and are perpendicular to the shared edge and up-down force directions are normal to the plane spanned by each pair of green edges.

We endow these triangulated meshes with elastic stretching and bending modes to capture the in-plane and out-of-plane deformation of thin sheets. The stretching mode simply treats each edge in the mesh as a linear spring, all edges having the same stretching stiffness. Accordingly, the magnitude of the restorative elastic forces applied to each node in a deformed edge with rest length x_0 and stretching stiffness k is given by $\frac{k_s}{x_0}(x' - x_0)$ and the energy contained in a deformed edge is given by

$$\frac{k_s}{2x_0}(x' - x_0)^2 \tag{A.43}$$

The x_0 term in denominator of the stretching mode ensures mesh-independence. The bending mode is characterized in terms of four vectors u_1, u_2, u_3 and u_4, each of which is

applied to a node in a pair of adjacent triangles. Defining the weighted normal vectors $N_1 = (x_1 - x_3) \times (x_1 - x_4)$ and $N_2 = (x_2 - x_4) \times (x_2 - x_3)$ and the shared edge $E = x_4 - x_3$, we may write

$$u_1 = |E| \frac{N_1}{|N_1|^2} \tag{A.44}$$

$$u_2 = |E| \frac{N_2}{|N_2|^2} \tag{A.45}$$

$$u_3 = \frac{(x_1 - x_4) \cdot E}{|E|} \frac{N_1}{|N_1|^2} + \frac{(x_2 - x_4) \cdot E}{|E|} \frac{N_2}{|N_2|^2} \tag{A.46}$$

$$u_4 = -\frac{(x_1 - x_3) \cdot E}{|E|} \frac{N_1}{|N_1|^2} - \frac{(x_2 - x_2) \cdot E}{|E|} \frac{N_2}{|N_2|^2}. \tag{A.47}$$

The relative magnitudes of these vectors constitute a pure geometric bending mode for a pair of adjacent triangles. For pairs of adjacent triangles that *do not* straddle the fold line, the force on each vertex is given by

$$F_i = k_b(\frac{\theta}{2} - \frac{\theta_0}{2})u_i \tag{A.48}$$

where k_b is the bending stiffness and θ is the angle between N_1 and N_2 that makes each u_i a restorative force. For pairs of adjacent triangles that straddle folds, θ_0 is non-zero and shifts the rest angle of the adjacency to a non-planar configuration. The bending energy contained in a pair of adjacent triangles is given by

$$E_b = k_b \int_{\theta_0}^{\theta} \frac{\theta}{2} - \frac{\theta_0}{2} \mathrm{d}\theta \tag{A.49}$$

with a precise form of

$$E_b = k_b(\frac{\theta}{2} - \frac{\theta_0}{2})^2 \tag{A.50}$$

which is quadratic in θ for $\theta \sim \theta_0$.

We introduce viscous damping so that the simulation eventually comes to rest. Damping forces are computed at every vertex with different coefficients for each oscillatory mode, bending and stretching. We distinguish between these two modes by projecting the

velocities of the vertices in an adjacency onto the bending mode, and the velocities of the vertices in an edge onto the stretching mode.

We use the Velocity Verlet numerical integration method to update the positions and velocities of the vertices based on the forces from the bending and stretching model and the external forces from our bending strategies. At any time $t + \Delta t$ during the simulation we can approximate the position $x(t + \Delta t)$ and the velocity $\dot{x}(t + \Delta t)$ of a vertex as

$$x(t + \Delta t) = x(t) + \dot{x}(t)\,\Delta t + \frac{1}{2}\ddot{x}(t)\,\Delta t^2 \tag{A.51}$$

$$\dot{x}(t + \Delta t) = \dot{x}(t) + \frac{\ddot{x}(t) + \ddot{x}(t + \Delta t)}{2}\,\Delta t \tag{A.52}$$

A single position, velocity and accleration update follows a simple algorithm.

- Compute $x(t + \Delta t)$
- Compute $\ddot{x}(t + \Delta t)$ using $x(t + \Delta t)$ for stretching and bending forces and $\dot{x}(t)$ for damping forces
- Compute $\dot{x}(t + \Delta t)$

Note that this algorithm staggers the effects of damping on the simulation by Δt.

In simulation, the Miura-ori plate is made of 21 by 21 unit cells, 21 being the number of unit cells in one direction. α varies from 20^o to 70^o, and θ varies from 30^o to 150^o, both every 10^o. We design two bending strategies, each of which corresponds to a pair of opposite boundaries. The left-right bending strategy identifies the adjacencies with O_2O_3 shared edges on left boundary unit cells and O_1O_2 shared edges on right boundary unit cells (highlighted in yellow in Fig.A.4b). For each of these adjcencies we apply equal and opposite forces to the vertices on their shared edge, the directions of which are determined to lie in the bisecting plane of $O_1O_2O_4$ and $O_1O_2O_7$ (left boundary unit cells) and $O_2O_3O_5$ and $O_2O_3O_8$ (right boundary unit cells) and perpendicular to the shared edge. The up-down

Figure A.5: 3D geometry of a bent Miura plate made of 21 by 21 unit cells with $\alpha = \theta = \pi/3$. For better display purpose, we use an example with pronounced deformation. However in the simulation we have done, we make sure that the radius of curvature is at least 10 times larger than the plate size, such that the deformation is within linear regime. Readers may want to play with different toolbar options to better visualize the geometry.

bending strategy identifies the top edges of each unit cell on the up and down boundaries of the pattern (shown in green in Fig.A.4b). Each unit cell has one such pair of edges and we apply equal and opposite forces to the not-shared vertices in this pair, the directions of which are normal to the plane spanned by the pair of edges. We take out the $11th$ row and $11th$ column of vertices on the top surface as two sets of points to locally interpolate the curvature near the center of the plate in x and y direction respectively. The largest difference of ν_b for the same design angle pairs α and θ between both B.Cs applied is less than 0.5%.

By applying the bending strategies described above, we are able to generate deformed Miura-ori plates in simulation. See the simulation result in the below interactive Fig.A.5 to understand the saddle geometry that results from bending the Miura-ori. Readers may want to play with different toolbar options to better visualize the geometry.

Appendix B

Supplementary material for Chapter 3

B.1 Critical Buckling Length of Lamella

The critical buckling height of a thin plate under compression of the surface tension σ is

$$L_{crit} \sim L_{ec} = \sqrt{Eh^3/\sigma}, \tag{B.1}$$

where L_{ec} is the typical elastocapillary length scale by which the interaction between elasticity and interfacial forces is defined. For the case when the plate is clamped at one end and axially compressed at the other by the capillary force, the exact expression [88] for L_{crit} is

$$L_{crit} = \pi[48(1-\nu^2)]^{-1/2} L_{ec} \approx 1mm, \tag{B.2}$$

where we have substituted the experimental parameters. L_{crit} is much larger than the lamella height $L = 40\mu m$, so buckling of the lamellae when they pierce the gas-liquid interface does not happen in our system.

B.2 Moment Calculation for The 2D Case

The 8 possible meniscus configurations can be classified into 6 cases, where we explicitly express the moments in terms of the state variables - tilting angles θ_n and liquid volumes V_n. We have scaled all lengths by L and moment by σL, so all results below are dimensionless.

Case 1: The meniscus is pinned on both tips (Figure 3.2(b1)). The half angle β_n subtended by the meniscus arc is determined by solving

$$V_n = \frac{1}{2}d(\sin\theta_n + \sin\theta_{n+1}) + \frac{1}{2}\sin(\theta_n - \theta_{n+1}) - a_n^2(\beta_n \csc^2\beta_n - \cot\beta_n), \tag{B.3}$$

for given V_n, θ_n and θ_{n+1}, where $d = D/L$ and half of the tip distance a_n is

$$a_n = \frac{1}{2}\sqrt{2 - 2\cos(\theta_{n+1} - \theta_n) + 2d(\cos\theta_{n+1} - \cos\theta_n) + d^2}. \tag{B.4}$$

β_n must satisfy $\beta_n \leq \hat{\beta}_n$, where $\hat{\beta}_n$ is the critical angle at which the meniscus starts to slide down from at least one lamella. $\beta_n < 0$ when the meniscus concaves down, $\beta_n = 0$ when the meniscus is flat, and $\beta_n > 0$ when the meniscus concaves up. The moments on the n^{th} and $n+1^{th}$ plates are given respectively by

$$M_n = -\frac{1}{2a_n}\left[\sin(\beta_n + \theta_n - \theta_{n+1}) + d\sin(\beta_n + \theta_n)\right], \tag{B.5}$$

$$M_{n+1} = \frac{1}{2a_n}\left[\sin(\beta_n + \theta_n - \theta_{n+1}) - d\sin(\beta_n - \theta_{n+1})\right], \tag{B.6}$$

Case 2: The meniscus is down from both tips (Figure 3.2(b3)). The contact angle is fixed at α. When $\theta_n \neq \theta_{n+1}$, the radius of the meniscus r_n is determined by solving

$$\begin{aligned} V_n =& \frac{d^2}{2}\frac{\sin\theta_n\sin\theta_{n+1}}{\sin(\theta_{n+1} - \theta_n)} - r_n^2\left[\cos^2\alpha\cot\left(\frac{\theta_{n+1} - \theta_n}{2}\right)\right. \\ &\left. + \sin\alpha\cos\alpha + \frac{\pi + \theta_{n+1} - \theta_n - 2\alpha}{2}\right]. \end{aligned} \tag{B.7}$$

The wetting length on the right side of the n^{th} plate and that on the left side of the $(n+1)^{th}$ are given respectively by

$$L_{wrn} = d\frac{\sin\theta_{n+1}}{\sin(\theta_{n+1}-\theta_n)} - r_n\left[\sin\alpha + \cos\alpha\cot\left(\frac{\theta_{n+1}-\theta_n}{2}\right)\right]. \tag{B.8}$$

$$L_{wln+1} = d\frac{\sin\theta_n}{\sin(\theta_{n+1}-\theta_n)} - r_n\left[\sin\alpha + \cos\alpha\cot\left(\frac{\theta_{n+1}-\theta_n}{2}\right)\right]. \tag{B.9}$$

When $\theta_n = \theta_{n+1} = \theta$, the meniscus radius is independent of V_n, and $r_n = d\sin\theta/(2\cos\alpha)$. l_n is determined by solving

$$V_n = \frac{2l_n - d\cos\theta}{2}d\sin\theta - \left(\frac{d\sin\theta}{2}\right)^2\tan\alpha - \frac{\pi-2\alpha}{2}\left(\frac{d\sin\theta}{2\cos\alpha}\right)^2. \tag{B.10}$$

The wetting length on the right side of the n^{th} plate and that on the left side of the $(n+1)^{th}$ plate are given respectively by

$$L_{wrn} = l_n - \frac{d}{2}\sin\theta\tan\alpha, \tag{B.11}$$

$$L_{wln+1} = l_n - \frac{d}{2}\sin\theta\tan\alpha - d\cos\theta. \tag{B.12}$$

In either case, the moment on the n^{th} plate and that on the $(n+1)^{th}$ plate are given respectively by

$$M_n = -\frac{L_{wr}{}_n^2}{2r_n} - L_{wrn}\sin\alpha. \tag{B.13}$$

$$M_{n+1} = \frac{L_{wl}{}_{n+1}^2}{2r_n} + L_{wln+1}\sin\alpha. \tag{B.14}$$

Case 3: when the meniscus slides down from the n^{th} plate and is pinned on the $(n+1)^{th}$ one. In this case $L_{wrn} = l_n$ and $L_{wln+1} = 1$.

$$a_n = \frac{1}{2}\sqrt{1 + l_n^2 - 2l_n\cos(\theta_n - \theta_{n+1}) + 2d(\cos\theta_{n+1} - l_n\cos\theta_n) + d^2}, \tag{B.15}$$

$$V_n = \frac{1}{2}l_n\sin(\theta_n - \theta_{n+1}) + \frac{1}{2}d(l_n\sin\theta_n + \sin\theta_{n+1}) - a_n^2(\beta_n\csc^2\beta_n - \cot\beta_n). \tag{B.16}$$

From the condition that contact angle on the n^{th} plate is α, we can get the following relations,

$$\cos(\alpha + \theta_n - \theta_{n+1}) + d\cos(\alpha + \theta_n) - l_n \cos\alpha = 2a_n \cos\beta_n, \tag{B.17}$$

and

$$\begin{aligned} &\sin(\alpha + \beta_n + \theta_n - \theta_{n+1}) + d\sin(\alpha + \beta_n + \theta_n) = l_n \sin(\alpha + \beta_n) \\ &\text{when} \quad \theta_n \neq \theta_{n+1}, \\ &d\cos\theta + 1 - l_n = \cos(\alpha + \beta_n) \\ &\text{when} \quad \theta_n = \theta_{n+1} = \theta. \end{aligned} \tag{B.18}$$

l_n and β_n are determined by solving either (B.16) and (B.17) or (B.16) and (B.18).

Moment on the n^{th} plate and that on the $(n+1)^{th}$ plate are given respectively by

$$M_n = -\frac{\sin\beta_n}{2a_n} l_n^2 - l_n \sin\alpha. \tag{B.19}$$

$$M_{n+1} = \frac{\sin\beta_n}{2a_n} - \sin(\theta_{n+1} - \theta_n - \alpha - 2\beta_n). \tag{B.20}$$

Case 4: when the meniscus slides down from the $(n+1)^{th}$ plate and is pinned on the n^{th} one. In this case $L_{wrn} = 1$ and $L_{wln+1} = l_n$.

$$a_n = \frac{1}{2}\sqrt{1 + l_n^2 - 2l_n\cos(\theta_n - \theta_{n+1}) + 2d(l_n\cos\theta_{n+1} - \cos\theta_n) + d^2}, \tag{B.21}$$

$$V_n = \frac{1}{2} l_n \sin(\theta_n - \theta_{n+1}) + \frac{1}{2} d(\sin\theta_n + l_n \sin\theta_{n+1}) - a_n^2(\beta_n \csc^2\beta_n - \cot\beta_n). \tag{B.22}$$

From the condition that contact angle on the $(n+1)^{th}$ plate is α, we can get the following relations,

$$\cos(\alpha + \theta_n - \theta_{n+1}) - d\cos(\alpha - \theta_{n+1}) - l_n \cos\alpha = -2a_n \cos\beta_n, \tag{B.23}$$

and

$$\begin{aligned}
&\sin(\alpha+\beta_n+\theta_n-\theta_{n+1})-d\sin(\alpha+\beta_n-\theta_{n+1})=l_n\sin(\alpha+\beta_n)\\
&\text{when}\quad \theta_n\neq\theta_{n+1},\\
&d\cos\theta+l_n-1=\cos(\alpha+\beta_n)\\
&\text{when}\quad \theta_n=\theta_{n+1}=\theta.
\end{aligned}\tag{B.24}$$

Similarly, l_n and β_n are determined by solving either (B.22) and (B.23) or (B.22) and (B.24).

Moment on the n^{th} plate and that on the $(n+1)^{th}$ plate are given respectively by

$$M_n=-\frac{\sin\beta_n}{2a_n}+\sin(\theta_{n+1}-\theta_n-\alpha-2\beta_n). \tag{B.25}$$

$$M_{n+1}=\frac{\sin\beta_n}{2a_n}l_n^2+l_n\sin\alpha. \tag{B.26}$$

For certain given V_n, θ_n and θ_{n+1}, although one end of the meniscus is depinned from the tip, there is no arc satisfying the enforced contact angle condition. In the following two cases, the menisci are approximated by straight lines. They are used to prevent the numerics from blowing up when two plates almost contact, yet very unlikely to happen.

Case 5: when the meniscus slides down from the tip of the n^{th} plate and keeps flat. The moment on the n^{th} plate and that on the $(n+1)^{th}$ plate are given respectively by

$$M_n=-\frac{l_n}{b_n}[\sin(\theta_n-\theta_{n+1})+d\sin\theta_n] \tag{B.27}$$

$$M_{n+1}=\frac{1}{b_n}[l_n\sin(\theta_n-\theta_{n+1})+d\sin\theta_{n+1}], \tag{B.28}$$

where l_n is determined by solving from the given volume

$$V_n=\frac{l_n}{2}\sin(\theta_n-\theta_{n+1})+\frac{d}{2}(l_n\sin\theta_n+\sin\theta_{n+1}), \tag{B.29}$$

and b_n is

$$b_n=\sqrt{1+l_n^2-2l_n\cos(\theta_n-\theta_{n+1})+2d(\cos\theta_{n+1}-l_n\cos\theta_n)+d^2}. \tag{B.30}$$

Case 6: when the meniscus slides down from the tip of the n^{th} plate and keeps flat. The moment on the n^{th} plate and that on the $(n+1)^{th}$ plate are given respectively by

$$M_n = -\frac{1}{b_n}[l_n \sin(\theta_n - \theta_{n+1}) + d \sin\theta_n] \tag{B.31}$$

$$M_{n+1} = \frac{l_n}{b_n}[\sin(\theta_n - \theta_{n+1}) + d \sin\theta_{n+1}], \tag{B.32}$$

where l_n is determined by solving from the given volume

$$V_n = \frac{l_n}{2}\sin(\theta_n - \theta_{n+1}) + \frac{d}{2}(\sin\theta_n + l_n \sin\theta_{n+1}), \tag{B.33}$$

and b_n is

$$b_n = \sqrt{1 + l_n^2 - 2l_n \cos(\theta_n - \theta_{n+1}) + 2d(l_n \cos\theta_{n+1} - \cos\theta_n) + d^2}. \tag{B.34}$$

B.3 Damping Coefficient for The 2D Case

In order to calculate the damping coefficient, we need to account for both the viscosity of the fluid and the viscoelasticity of the solid. First we consider the contribution from the fluid. The Reynolds number $Re \sim 10^{-5}$ or less, so that inertia of the fluid is negligible. We use lubrication theory to calculate the moment acting on the plate caused by flow although the ratio of plate height L to the spacing D does not strictly satisfy that $L/D \gg 1$. Figure B.1 illustrates 3 rigid plates hinged at the base. The upper and lower one are perpendicular to the substrate, and the middle one is rotating clockwise at the angular velocity $\dot{\theta}$. The liquid is confined between two plates and the ambient pressure is set to be 0.

In the bottom chamber, the momentum conservation of the fluid in the x and y directions are

$$\frac{\partial p^+}{\partial x} = \mu \frac{\partial^2 u}{\partial y^2} \quad \text{and} \quad \frac{\partial p^+}{\partial y} = 0, \tag{B.35}$$

where p^+ is the pressure and μ is the fluid viscosity. The boundary conditions are

$$u = 0 \quad \text{at} \quad y = 0 \quad \text{and} \quad y = H(x,t). \tag{B.36}$$

From (B.35) and (B.36), we can get

$$u(x,y,t) = \frac{1}{2\mu}\frac{\partial p^+}{\partial x}(y^2 - Hy). \tag{B.37}$$

The mass conservation is

$$\frac{d}{dt}\left[\frac{1}{2}\rho x(D+H)\right] = \rho[Q(0,t) - Q(x,t)], \tag{B.38}$$

where $Q(x,t)$ is the flux. As $u = 0$ at $y = 0$, $Q(0,t) = 0$. Substitute (B.37) into (B.38),

$$\begin{aligned} Q(x,t) &= \int_0^H u(x,y,t)dy = \int_0^H \frac{1}{2\mu}\frac{\partial p^+}{\partial x}(y^2 - Hy)dy \\ &= -\frac{H^3}{12\mu}\frac{\partial p^+}{\partial x} = -\frac{1}{2}x\frac{dH}{dt}. \end{aligned} \tag{B.39}$$

From (B.39) and $H(x,t) = D - \dot{\theta}tx$ in the linear regime, we get

$$\frac{\partial p^+}{\partial x} = -\frac{6\mu}{H^3}x^2\dot{\theta}. \tag{B.40}$$

Integrate (B.40) and use the boundary condition on pressure $p^+(L,t) = 0$, and we see that

$$p^+(s,0) = \frac{2\mu L^3}{D^3}\dot{\theta}(1 - s^3), \tag{B.41}$$

where $s = x/L \in [0,1]$.

So far we have only considered the pressure acting on the lower side of the middle pillar. The pressure difference between two sides is

$$p^+(s,0) - p^-(s,0) = 2p^+(s,0) = \frac{4\mu L^3}{D^3}\dot{\theta}(1 - s^3). \tag{B.42}$$

And the moment on the middle pillar due to fluid flow is

$$M_\mu = L^2\int_0^1 (p^+(s,0) - p^-(s,0))sds = \frac{6\mu L^5\dot{\theta}}{5D^3}, \tag{B.43}$$

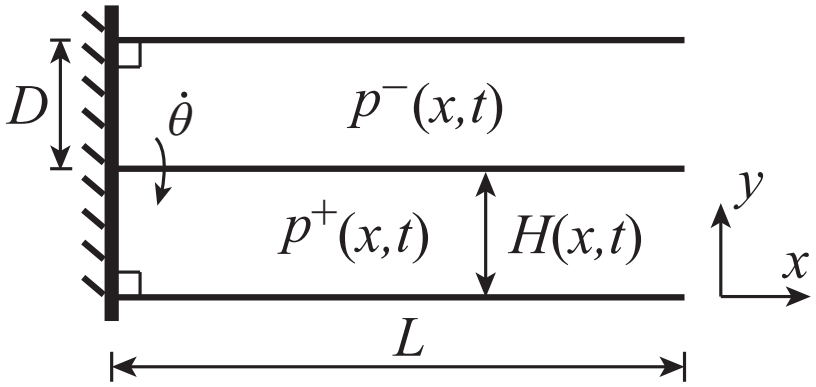

Figure B.1: Sketch of two neighboring cells. When the middle plate is rotating, the nonuniform pressure caused by flow acts on the plate from both sides and hinders the rotation.

where the last equality follows from (B.42).

Therefore the damping coefficient from the viscous fluid is approximately

$$C_1 = \frac{M_\mu}{\dot{\theta}} = \frac{6\mu L^5}{5D^3}. \tag{B.44}$$

Next we consider the damping coefficient resulted from viscoelasticity of the solid. We can estimate it from the vibration of a viscoelastic beam made of the Kelvin-Voigt material, which can be represented by a viscous damper and elastic spring connected in parallel. The constitutive law thus is

$$\Sigma = E\epsilon + \eta\dot{\epsilon}, \tag{B.45}$$

where Σ is the stress, ϵ is the strain, E is the Young's modulus and η is the viscosity. The strain-displacement relation is

$$\epsilon = \frac{y}{r} = -y\frac{\partial^2 u}{\partial x^2}, \tag{B.46}$$

where r is the radius of curvature due to bending, and u is the transverse displacement of the beam. The force balance equation is

$$\frac{\partial^2 M}{\partial x^2} + \rho_s \ddot{u} = 0, \tag{B.47}$$

where the moment $M = -\int_A \Sigma y dA$, and ρ_s is the density of the solid material.

Substitute (B.46) into (B.45), then substitute (B.45) into (B.47), and we can get the vibration equation of a viscoelastic beam, which is

$$EI\frac{\partial^4 u}{\partial x^4} + \eta I\frac{\partial^4 \dot{u}}{\partial x^4} + \rho_s \ddot{u} = 0, \quad \text{where} \quad I = \int_A y^2 dA. \tag{B.48}$$

For the thin plate, E is replaced by $E/(1-\nu^2)$, ρ is replaced by ρh and $I = h^3/12$, where h is the thickness of the plate. We can get two time scales $\tau_{m1} \sim \sqrt{12\rho(1-\nu^2)L^4/Eh^2}$ and $\tau_{m2} \sim \eta(1-\nu^2)/E$ by balancing the first and the third term, the first and the second term of the LHS of (B.48) respectively. Substitute the parameters from the experiment $L = 40\mu m$, $h = 10\mu m$, $E = 1.5Mpa$, $\nu = 0.5$ and $\rho_s = 965kg/m^3$, $\tau_{m1} \sim 10\mu s$. We roughly estimate η by using the indentation experimental result in the literature [89]. For the PDMS cured at the base to curing agent ratio of $10:1$, the loss tangent at a vibration rate of $4Hz$ is around 0.09, which is $[\eta(1-\nu^2)\omega/E]|_{\omega=4} = 0.09$, so $\tau_{m2} \approx 22.5ms$. As $\tau_{m2} \gg \tau_{m1}$, the inertia term is dominated over by the damping term in (B.48) for the micro cantilever, and thus can be neglected. Then the damping coefficient due to internal viscosity of the solid is

$$C = C_1 + C_2 = \frac{6\mu L^5}{5D^3} + \tau_m k \approx \tau_m k. \tag{B.49}$$

where we have omitted the subscript '2' in τ_{m2} and $\tau_m \approx 22.5ms$ is the time scale for the viscoelastic fiber to relax mechanically.

B.4 Damping Coefficient for The 3D Case

First, To estimate the drag coefficient c and the time scale in Eq. (3.22), we consider both the internal contribution from viscoelasticity of the solid material and the external contribution from the viscous fluid, and find that the former one dominates.

AFM characterization of the epoxy microfibers [90] shows that the force vs displacement curve has a clear hysteresis loop, which reveals that the epoxy nanofibers are

viscoelastic although primarily elastic. For a fiber of radius $R = 1.5\mu m$, length $L = 9\mu m$, and bending spring constant $k = 3\pi ER^4/4L^3 = 17.22N/m$, where $E = 1GPa$ is the Young's modulus, the hysteresis is measured 32% of the total work done at max deflection $x = 1.5\mu m$ and rate of deflection $v = 6\mu m/s$. Thus, the effective damping coefficient c_1 from the internal viscoelasticity can be calculated from $2c_1vx = 0.3 \times 0.5 \times kx^2$, based on the Kelvin-Voigt model.

To calculate the damping coefficient c_2 from the external viscous fluid, we consider a circular cylinder of radius R moving with velocity U normal to its axis at small Reynolds number $Re = 2R\rho U/\mu \sim 10^{-7}$, in which case, the drag of magnitude $4\pi\mu U/\ln(7.4/Re)$ per unit length was first derived by Lamb [91]. As the center of the pillar is moving at a velocity of almost $v/2$ when the cantilever tip is deformed at a velocity of v in the AFM test, we take $c_2 = 2\pi\mu L/\ln(7.4/Re)$ as an approximation.

It turns out that $c_1/c_2 \sim 10^7$ for the experimental parameters listed above, which indicates that the external damping from viscous fluid can be neglected and $c \approx c_1$. Therefore, the time scale for the fiber to relax mechanically is $\tau_m = c_1/k \sim 10^{-2}s$ in Eq. (3.22), and τ_m is a material property (as in the Prony series) and does not depend on the geometric dimensions of the fiber.

B.5 The Assumption of Uniform Liquid Pressure for The 3D Case

Next, we estimate the time scale for the fluid to relax given nonuniform pressure distribution. To do so, we use Darcy's law

$$q = \frac{\kappa}{\mu}\nabla P \tag{B.50}$$

where q is the flux (discharge per unit area, with units of length per time), κ is the permeability of the two-dimensional bristle array, μ is the viscosity of the fluid, and ∇P is the pressure gradient. $\nabla P \sim \frac{\sigma}{D\ell}$, where σ is the surface tension of the liquid, D is the pillar spacing, and ℓ is the system size. κ is approximated from a periodic square array of parallel cylinders, which is the initial configuration of our system. In the dilute solid volume fraction (porosity) regime, the asymptotic expression [92] for κ is

$$\kappa = R^2 \frac{-0.5 \ln \phi - 0.745 + \phi - 0.25\phi^2}{4\phi}, \tag{B.51}$$

where R is the radius of the pillar, $\phi = \pi R^2/D^2$ is the porosity. In our typical experiment, $R = 150nm$, $L = 4.5\mu m$, $D = 2\mu m$, $E = 0.2GPa$, and $\sigma = 0.022N/m$. For a domain of size $\ell \sim 100\mu m$, which contains thousands of bristles, the time scale for the fluid to relax so that the pressure inside the domain is uniform can be estimated as $\tau_f = \ell/q \sim 10^{-3} < \tau_b$.

In conclusion, for a reasonably large patch of bristles, it is plausible to assume that the pressure throughout the liquid is uniform during the evaporation because of the well-separated time scales – the time scale for the fluid to relax ($\sim 10^{-3}s$ for 50 by 50 bristles) $\ll$ that for the bristles to respond ($\sim 10^{-2}s$) $\ll$ that for the evaporation ($\sim 10^{0}s$).

Appendix C

Supplementary material for Chapter 4

For completeness, we briefly review of the discrete model that serves as the basis for our mesoscopic continuum model.

The lamellae are modeled as rigid plates of unit depth elastically hinged at the base (Fig. C.1(a)). The hinge elastic constant can be approximately derived from the bending response of a short cantilever by a transverse force F at its free end, which is given by

$$k = \frac{d(F\delta)}{d\theta} = \frac{Eh^3}{3L}, \tag{C.1}$$

where $\delta = 4FL^3(1-\nu^2)/Eh^3$ is the deflection at the free end, and θ is the deflection angle of the plate with respect to the vertical direction.

The pressure field inside the liquid is considered as uniform. This assumption is based on two facts: 1. In our system, gravity can be neglected, because the Bond number $B_o \sim 10^{-5} \ll 1$ indicates that the gravity is dominated by surface tension. 2. Comparing the viscous torque acting on the plate due to flow $M_\mu \sim \mu L^5\dot{\theta}/D^3$ with that caused by the surface tension $M_\sigma \sim \sigma L^2/D$, where μ is the viscosity of the fluid and $\dot{\theta}$ is the angular

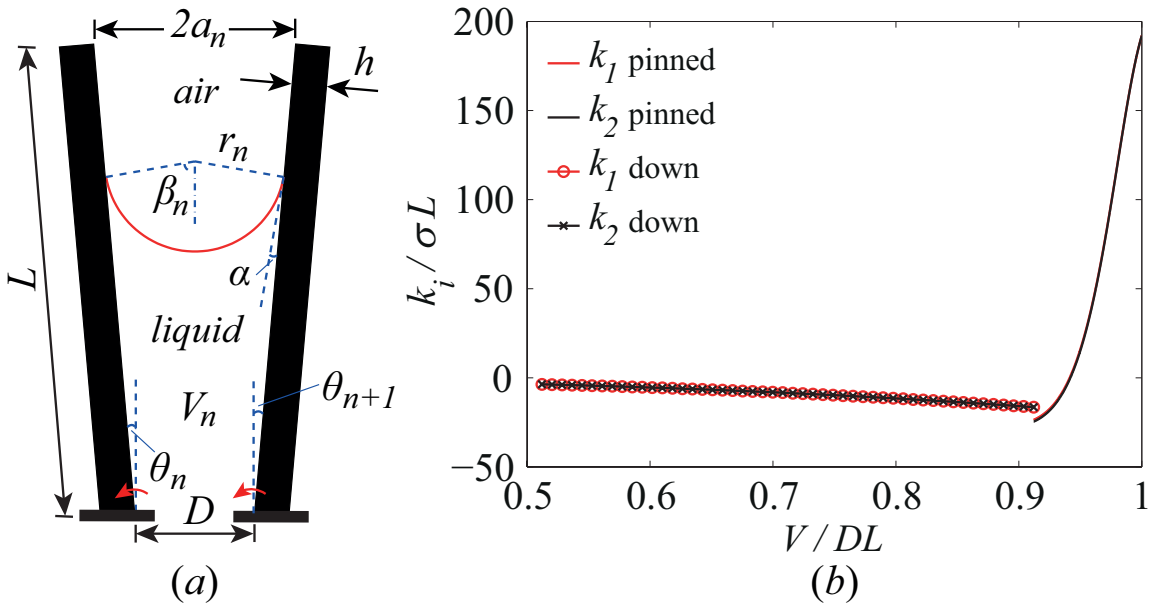

Figure C.1: (a) Sketch of the model of the n^{th} cell confined by two neighboring lamellae. The red curve represents the air-liquid interface. (b) Effective spring stiffness due to capillarity as a function of liquid volume for $L/D = 4$ at the homogeneous state where all pillars are vertical. When the meniscus is pinned at the plate tip, $k_2 = k_1 - \sigma L \sin\beta$. When the meniscus is down from the plate tip, $k_1 = k_2$. The discontinuity in k_i corresponds to the meniscus sliding down from the tip.

velocity of the rotating plate, we find that $M_\mu/M_\sigma \sim 10^{-3} \ll 1$ for $\dot{\theta} \sim O(1)$, which indicates that pressure effects due to fluid flow can be neglected. Therefore, the air-liquid interface can be well approximated by a circular arc because of the uniform pressure in each cell.

We assume the contact angle to be arbitrary when the meniscus is pinned on the tip, as long as it is larger than the critical value α. The meniscus can thus be concave-up, flat, or concave-down. Once the contact angle reaches α, it remains constant at α as the meniscus slides down from the tip.

Consequently, the meniscus profile and the resulting moment M_n can be calculated for any given deflection angles θ_n, θ_{n+1} (counter-clockwise is positive) and the liquid volume per unit depth V_n. We include the following results that are necessary for our subsequent derivation of capillary stiffnesses.

For the case when the meniscus is pinned on both tips, The moments on the n^{th} and $(n+1)^{th}$ plates are given respectively by

$$M_n = -\frac{1}{2a_n}[\sin(\beta_n + \theta_n - \theta_{n+1}) + d\cos(\beta_n + \theta_n)], \tag{C.2}$$

$$M_{n+1} = \frac{1}{2a_n}[\sin(\beta_n + \theta_n - \theta_{n+1}) + d\cos(\theta_{n+1} - \beta_n)], \tag{C.3}$$

where $2\beta_n$ is the angle subtended by the meniscus arc, $d = D/L$, and $2a_n$ is the tip separation. β_n is determined by solving

$$\frac{V_n}{L^2} = \frac{1}{2}d(\cos\theta_n + \cos\theta_{n+1}) + \frac{1}{2}\sin(\theta_n - \theta_{n+1}) - a_n^2(\beta_n \csc^2\beta_n - \cot\beta_n), \tag{C.4}$$

for given V_n, θ_n and θ_{n+1}, and

$$2a_n = [2 - 2\cos(\theta_{n+1} - \theta_n) + d^2 + 2d(\sin\theta_n - \sin\theta_{n+1})]^{\frac{1}{2}}. \tag{C.5}$$

β_n must satisfy $\beta_n \leq \beta_n^*$, where β_n^* is the critical angle at which the meniscus starts to slide

down from at least one lamella. $\beta_n < 0$ when the meniscus concaves down, $\beta_n = 0$ when the meniscus is flat, and $\beta_n > 0$ when the meniscus concaves up.

For the case when the meniscus is down from both tips, and $\theta_n = \theta_{n+1} = \theta$, the moments on the n^{th} and $(n+1)^{th}$ plate are given respectively by

$$\begin{aligned} M_n &= -\frac{L_{wr\,n}^2}{2r_n} - L_{wr\,n}\sin\alpha, \\ M_{n+1} &= \frac{L_{wl\,n+1}^2}{2r_n} + L_{wl\,n+1}\sin\alpha, \end{aligned} \tag{C.6}$$

where the meniscus radius $r_n = d\cos\theta/(2\cos\alpha)$, and the wetting length on the right side of the n^{th} plate, $L_{wr\,n}$, and that on the left side of the $(n+1)^{th}$ plate, $L_{wl\,n+1}$, are given respectively by

$$\begin{aligned} L_{wr\,n} &= l_n - \frac{d}{2}\cos\theta\tan\alpha, \\ L_{wl\,n+1} &= l_n - \frac{d}{2}\cos\theta\tan\alpha + d\sin\theta. \end{aligned} \tag{C.7}$$

l_n is determined by solving

$$\frac{V_n}{L^2} = \frac{2l_n + d\sin\theta}{2} d\cos\theta - \left(\frac{d\cos\theta}{2}\right)^2 \tan\alpha - \frac{\pi - 2\alpha}{2}\left(\frac{d\cos\theta}{2\cos\alpha}\right)^2. \tag{C.8}$$

So far, we have only calculated the moments based on a 2-plate model. To get the total moment on one plate, we must add the contributions from both adjacent cells. For example, we can obtain the full expression of M_n simply by replacing n by $n-1$ in Eq. (C.3) and add up to Eq. (C.2) for the case when the meniscus is pinned at both tips, which readily yields $M_n = M_n(\theta_{n-1}, \theta_n, \theta_{n+1}, V_n, V_{n-1})$.

For a periodic domain of $2N$ vertical lamellae and the same volume of liquid V

confined in each cell, the stiffness matrix of the system $d\overrightarrow{M}/d\overrightarrow{\theta}$ is given by

$$\begin{bmatrix} \ddots & \vdots & \vdots & \vdots & \vdots & \vdots & \\ \dots & -k_1 & 2k_2 & -k_1 & 0 & 0 & \dots \\ \dots & 0 & -k_1 & 2k_2 & -k_1 & 0 & \dots \\ \dots & 0 & 0 & -k_1 & 2k_2 & -k_1 & \dots \\ & \vdots & \vdots & \vdots & \vdots & \vdots & \ddots \end{bmatrix}, \tag{C.9}$$

where $\overrightarrow{M}$ is the vector of moments on all plates and $\overrightarrow{\theta}$ is the vector of deflection angles of all plates, and $k_1(\sigma L, V/L^2)$ and $k_2(\sigma L, V/L^2)$ are the capillary stiffnesses. The eigenvalues $s(f)$ and eigenvectors $\Psi(f)$ of $d\overrightarrow{M}/d\overrightarrow{\theta}$ thus are given by

$$\begin{aligned} s(f) &= -2k_1\cos(f) + 2k_2 + k_b, \\ \Psi(f) &= [1, e^{if}, e^{2if}, \dots, e^{i(2N-3)f}, e^{i(2N-2)f}, e^{-if}] \end{aligned} \tag{C.10}$$

respectively, where $f = n\pi/N$ with $n = 1, 2, \dots, 2N$.

For the case when the meniscus is pinned at both tips,

$$\begin{aligned} \frac{k_1}{\sigma L} &= \frac{\cos\beta - d\sin\beta}{d}\left[1 + \frac{1 - d(\beta\csc^2\beta - \cot\beta)}{d^2\csc^2\beta(1 - \beta\cot\beta)}\right] - \frac{\sin\beta + d\cos\beta}{d^2} + \sin\beta, \\ k_2 &= k_1 - \sigma L\sin\beta \end{aligned} \tag{C.11}$$

where $d = D/L$, and 2β is the angle subtending the meniscus arc and is determined by the volume

$$\frac{V}{L^2} = d - \left(\frac{d}{2}\right)^2(\beta\csc^2\beta - \cot\beta). \tag{C.12}$$

For the case when the meniscus is no longer at both tips,

$$\begin{aligned} \frac{k_1}{\sigma L} &= -\left[\frac{L_c}{r}\sin\alpha + \frac{L_c^2}{2r^2} + \sin^2\alpha\right]\frac{2L_c + d\tan\alpha}{4\cos\alpha}, \\ k_1 &= k_2 \end{aligned} \tag{C.13}$$

where $r = d/(2\cos\alpha)$ is the radius of meniscus, and the contact line position L_c is determined by the volume

$$\frac{V}{L^2} = L_c d + d^2\tan\left(\frac{\alpha}{4}\right) - d^2\frac{\pi - 2\alpha}{8\cos^2\alpha}. \tag{C.14}$$

We take $k_1 = k_2 = k_c$ for simplicity henceforth, as in Eq. (C.11) $\sigma L \sin\beta/k_1 \ll 1$ for the parameter space that we are interested in.

Only key expressions relevant to Chapter 4 are listed here, while the complete details are given in Chapter 3 and Appendix B.